Rotational Characterization of TESS Stars with Deep Learning

A DISSERTATION SUBMITTED TO THE GRADUATE DIVISION OF THE
UNIVERSITY OF HAWAI‘I AT MĀNOA IN PARTIAL FULFILLMENT OF THE
REQUIREMENTS FOR THE DEGREE OF

DOCTOR OF PHILOSOPHY

IN

ASTRONOMY

August 2022

By
Zachary R. Claytor

Dissertation Committee:

Jennifer L. van Saders, Chairperson
Daniel Huber
Peter Sadowski
Benjamin Shappee
Xudong Sun
Monique Chyba

From *Strange Planet* by Nathan W. Pyle. Used with permission by author.

For my parents Cheryl and Randy, and my sister Elyse, who were my first teachers;
and for my wife Natalie, who has shown unwavering devotion and support.

Acknowledgments

The road to a PhD cannot be taken alone. I have had friends, family, and colleagues cheering me on the entire way. Even in the midst of seemingly never-ending Unprecedented Times, their support and encouragement have never failed me.

First I want to acknowledge Jen van Saders, who agreed to advise me on a project before she even arrived to the IfA as faculty. Jen has been an invaluable source of support, wisdom, and empathy. As an advisor she gave the right combination of high expectations, precisely applied pressure, and patient understanding to help me thrive.

I'm grateful to my dissertation committee for their insights, discussions, feedback, and support.

Within the IfA, I want to thank Roy Gal, Carolyn Kaichi, and J.D. Armstrong for teaching me to love outreach, which has been one of the greatest highlights of my grad school career. I'm grateful to Dave Tholen and Josh Barnes, who were my first advisors and helped me ascend the steep learning curve of graduate education. I also want to acknowledge the people at the IfA who made it a home for me: Laura Toyama, Melissa Matsuura, Caroline Piro, Faye Uyehara, Amy Miyashiro, Evelyn Moss, Wayne Nakamoto, Bill Unruh, and Doug Simons. I must acknowledge my grad school cohort—and especially Ashley, Deep, Erica, and Ryan—for the jokes and teasing, the commiseration, the incredible adventures, and for being some of the finest people I have had the pleasure to share life and offices with.

My family—this journey started because I decided around kindergarten that I wanted to be an astronaut. From that day forward my parents encouraged me to keep going, no matter how difficult things got. I owe my positivity, my work ethic, and my stubbornness to them. My sister was the first in our family to go to college. 8-year old me didn’t understand it at the time. But once I did, it inspired me to never stop learning, never stop enriching myself, never stop striving to be better. And of course my wife Natalie has been with me through my best and my worst. She has been my biggest cheerleader. I could not have finished this race without her support, leadership, patience, and kindness.

I can’t forget my undergraduate professors at Ohio Wesleyan University, who have remained good friends and mentors. In particular I want to acknowledge Bob Haring-Kaye for his continued guidance and shepherding. As an academic and spiritual mentor, I owe so much of my confidence in faith and in science to him. I am also grateful to Bob Harmon for his endless and infectious enthusiasm about astrophysics. While we’re here, I should also acknowledge the delightful irony that I started with stellar light curves while learning from Bob Harmon at OWU, and despite hopping all over the universe from research on Pluto, to high-redshift quasars, to near-Earth asteroids, to interacting galaxies, I came back to rest on the comforting ebb and flow of the stellar light curve.

Last but not least, I want to recognize the wonderful ‘āina of Mānoa. The Institute for Astronomy rests on the mokupuni of O‘ahu, in the moku of Kona, in the ‘ahupua‘a of Waikīkī, in the ‘ili of Kolowalu, under the watchful slopes of Mānoa valley. My life, my perspective, and my work have been enriched by this place and the people who live here. Mahalo nui loa.

Abstract

Rotation is a fundamental property of stars. The *Kepler* mission revolutionized the field of stellar rotation, delivering periods of over 50,000 stars near the plane of the Milky Way. The distribution of periods revealed unexpected gaps, dips, and edges that cannot be described by current rotational evolution models, demanding new physical explanations. To sharpen the features in the distribution and to disentangle the effects of star formation history, more measurements of rotation are needed across the entire sky.

The TESS mission has the potential to probe stellar rotation in millions of stars across the entire sky, but mission systematics—instrumental noise, observing gaps, and changes in detector sensitivity—have prevented recovery of rotation periods longer than 13.7 days. We used deep learning to see through TESS systematics and recover periods from year-long light curves. Our approach uses a training set of synthesized light curves from realistic star spot evolution simulations, with real light curve systematics from quiet TESS stars. Evaluating the network on real TESS data, we estimated reliable periods for 9,837 cool dwarfs. We recovered key features of the *Kepler* and K2 distributions, including periods up to 60 days. We reproduced the intermediate rotation period gap for the first time using TESS, as well as a dip in photometric activity surrounding it.

Combining our TESS rotation periods with spectroscopic temperatures and abundances from APOGEE, we examined the detectability of rotation across fundamental stellar parameters, finding a strong dependence on temperature and age. Using gyrochronology, we inferred masses, ages, and other fundamental properties for the 6,632 TESS stars with APOGEE spectroscopy and corroborated evolution trends of Galactic chemistry and magnetic activity seen with *Kepler*. Finally with new measurements of spot filling factor from APOGEE, we investigated the spottedness of stars across the period distribution. We found that stars exhibit elevated spot fractions in the same regime where magnetic braking temporarily stalls in young open cluster stars, suggesting a common cause. Now with the ability to estimate rotation periods, including long periods, across the entire sky, we can characterize stars along many more lines of sight than before, enabling detailed study of the Galaxy's stellar populations.

Table of Contents

List of Tables

List of Figures

Chapter 1

Introduction

Heinrich Vogt and Henry Norris Russell independently posited that a star's structure and evolution is determined uniquely by its mass and distribution of chemical elements (Carroll & Ostlie 2006). While remarkably this statement, known as the Vogt–Russell theorem, has proven to be approximately true, we know today that stars are inherently more complicated and that other fundamental quantities affect their lives. Among the most important is rotation.

1.1 Why Rotation?

Rotation is deeply connected to the physics, structure, and evolution of stars. It prolongs stars' lifetimes as it mixes extra fuel into their cores, and stars rotating fast enough will depart from sphericity (Pinsonneault 1997; Maeder & Meynet 2000). In tandem with surface convection, rotation also powers magnetism, which gives rise to cool surface spots and causes flares. Magnetized winds exert torque on stars, causing them to spin down over time; this allows us to infer ages from the rotation periods of low-mass stars using gyrochronology (Skumanich 1972; Barnes 2007; Mamajek & Hillenbrand 2008; Epstein & Pinsonneault 2014; Angus et al. 2015). Magnetism is also the source of space weather,

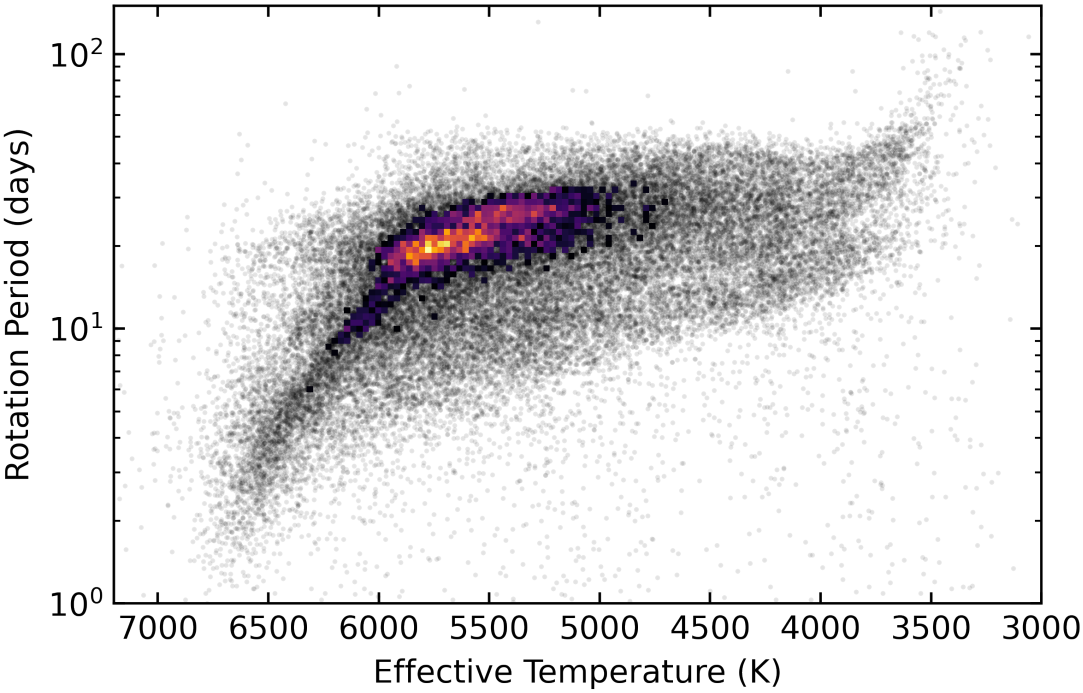

Figure 1.1: The distribution of rotation periods as a function of effective temperature in *Kepler*'s main sequence stars. The visualization changes to a 2D histogram in the region where points are too densely populated to see in the scatter plot. Periods are taken from Santos et al. (2019, 2021).

so understanding how rotation drives magnetism across all types of stars will allow us to better understand the magnetic behavior of our own star, the Sun.

Consequently, rotation period measurements are imperative if we are to answer questions about formation and evolution of stars, from the Sun to the diverse populations that make up our galaxy. Before the *Kepler* mission, rotation periods had been measured for a few thousands of stars (Irwin & Bouvier 2009; Hartman et al. 2011; Affer et al. 2012). *Kepler* revolutionized the field of stellar rotation, increasing the number of measured periods by an order of magnitude (McQuillan et al. 2014; Santos et al. 2019, 2021).

We can visualize the connections between stellar rotation, structure, magnetism, and evolution through the distribution of rotation periods observed by the *Kepler* mission (Borucki et al. 2010), shown in Figure 1.1. Here we show period versus effective temperature for 49,555 main sequence stars in the *Kepler* field (Santos et al. 2019, 2021). Single stars are born rapidly rotating and spin down as they age (e.g., Skumanich 1972), but their temperatures do not change appreciably during the main sequence ($\sim$ a few hundred K for the Sun). As a result, stars in isolation will move upwards along the diagram as they evolve and spin down. A field star population like that observed by *Kepler* comprises a mix of masses, metallicities, and ages. In Figure 1.1, temperature encapsulates most of the mass dependence, while the vertical spread in rotation period is set by the underlying ages and metallicities. The various features in the period–temperature distribution are sculpted by the evolution of rotation across time (e.g., McQuillan et al. 2014; Davenport & Covey 2018; Curtis et al. 2020; Santos et al. 2021), and the variations of that evolution across mass or temperature. Thus, understanding how these features arise will lead to a better understanding of stellar evolution across mass, metallicity, and age.

1.1.1 Features of the *Kepler* Rotation Period Distribution

Kepler gave us the best current example of a field star rotation period distribution. Its stellar populations provide a powerful test bed for rotational evolution theories (e.g., van Saders et al. 2019). Trying to reproduce the *Kepler* distribution highlighted shortcomings in our understanding of rotation that are best highlighted in the various edges, pileups, gaps, and dips that form in specific period and temperature ranges. Overall, cool stars ($T_{\rm eff} \lesssim 6,000$ K) spin more slowly and have a wider range of periods than hotter stars. This is an effect of the fundamental difference in rotational evolution above and below the temperature at which stars form surface convection zones, known as the Kraft break after Kraft (1967). Below (i.e., cooler than) the Kraft break, surface convection works with rotation to produce strong magnetic fields. These fields act on charged stellar winds, carrying angular momentum away from stars and causing them to spin down substantially over time. Above the Kraft break, outer convective envelopes vanish, and stars do not experience magnetic braking. Hot main sequence stars then largely maintain their initial, rapid rotation rates regardless of age, while cool stars evolve to slower periods and exhibit a spread in period proportional to the spread in the underlying ages.

We discuss features specific to period and temperature ranges in the following sections.

Lower Edge

The *Kepler* period distribution exhibits a sharp lower edge from about (6000 K, 4 d) to (3500 K, 20 d). A possible explanation for this edge is the convergence of field stars onto a slowly-rotating sequence (Curtis et al. 2020). While stars are born with a range of initial, usually rapid rotation periods, faster rotating stars produce stronger magnetic fields and therefore experience stronger braking torques (e.g., Kawaler 1988) as long as they are not magnetically saturated (Krishnamurthi et al. 1997). Consequently at the same age and temperature, fast-spinning stars spin down faster, and slow-spinning stars spin down more slowly. Stars with similar masses born at nearly the same time will then convergence onto a tight rotation sequence at fixed age, regardless of their initial rotation speeds. These tight sequences are seen in young open clusters (Krishnamurthi et al. 1997; Irwin & Bouvier 2009; Gallet & Bouvier 2015; Douglas et al. 2017; Rebull et al. 2017; Agüeros et al. 2018; Douglas et al. 2019; Curtis et al. 2019, 2020), which provide snapshots of rotational evolution for a range of masses at fixed age and composition. While convergence occurs at different ages for different masses (Gallet & Bouvier 2015), this convergence is complete in Solar-temperature stars in open clusters by 1 Gyr. The *Kepler* field contains a population of old stars relative to the clusters, with the vast majority older than 1 Gyr (Silva Aguirre et al. 2018; Claytor et al. 2020). By this time, nearly all the stars have reached the slowly-rotating sequence, with the most recently converged stars producing the edge. On the other hand, in an attempt to forward model the *Kepler* period distribution using population synthesis, van

Saders et al. (2019) could not explain the sharpness of the observed edge despite including spin-down laws that reproduce the convergence of spin-down at fixed age and mass. The puzzle thus remains unsolved.

Upper Edge & Hot Star Pileup

The upper edge of the period distribution is an effect of stellar magnetic braking. For temperatures below 5,100 K, the edge represents the oldest stars in the Galaxy, with ages near ~ 12 Gyr that have spun down significantly with time (van Saders et al. 2019). The cool side of the edge is mostly reproducible with "standard" Skumanich-like braking laws (which follow $P_{\rm rot} \propto t^{0.62}$, after Skumanich 1972), with the exception of the dip centered around 4,000 K. We discuss this dip in the next section.

Hotter than 5,100 K, Skumanich-like spin down fails to reproduce the upper edge of the period distribution (Angus et al. 2015). Instead, (van Saders et al. 2016) found that magnetic braking must stall or weaken, which lowers the predicted edge and produces a pileup in stars along the edge (van Saders et al. 2019). While this pileup was not initially seen in the *Kepler* distribution, using more precise temperatures from spectroscopy brought the pileup into focus (David et al. 2022). The distribution plotted in Figure 1.1 includes spectroscopic temperatures from APOGEE (Majewski et al. 2017; Jönsson et al. 2020) and LAMOST (Zhao et al. 2012; Zong et al. 2020), making the pileup visible.

M Dwarf Dip

There is a dip in the upper envelope of the period distribution centered around 4,000 K. McQuillan et al. (2014) identified this dip and noted that no contemporary gyrochronology models could reproduce the dip. van Saders et al. (2019) used population synthesis to reproduce the *Kepler* period distribution using the most advanced spin-down models at the time, but failed to reproduce the dip. The cause of the dip remains unknown.

Intermediate Period Gap

The *Kepler* period distribution exhibits a gap in rotation periods between temperatures of roughly 3,500 K and 5,000 K, first detected by McQuillan et al. (2013). The period at which the gap occurs increases with decreasing temperature. McQuillan et al. (2013) proposed that gap falls between two different stellar populations, with the lower population arising from a recent, local burst of star formation. Davenport & Covey (2018) combined *Kepler* data with new parallax measurements from *Gaia* to show that the gap seems to disappear from stellar samples further than 525 pc, supporting the claim that the gap arises from local star formation and is not universal. However, restricting magnitude-limited samples to further distances has two effects that may masquerade as a disappearance of the gap. First, the restriction to further distances removes intrinsically fainter cool stars. The sample of Davenport & Covey (2018) with $d \geq 525$ pc has bluer (hotter) stars with *Gaia* color $G_{BP} - G_{RP} \leq 1.5$, a regime where detection of the gap is already tenuous in *Kepler*. Second, stars at larger distances will naturally have less certain colors and periods because they are fainter, potentially blurring the gap even if it is present. More recent studies have all but buried the star formation hypothesis of the gap: Curtis et al. (2020) found that Ruprecht 147, a 2.7-Gyr-old open cluster, *crosses* the *Kepler* rotation period gap. That a coeval population of stars intersects the gap rules out the possibility that the gap arises different epochs of star formation.

Another hypothesis for the gap, also suggested by McQuillan et al. (2013, 2014), is that stars just below the period gap undergo a short phase of rapid spin down. This could be caused, for example, by a period of non-rigid rotation when the core and convective envelope rotationally decouple, evolve independently, and then recouple, exchanging angular momentum and temporarily slowing or even halting spin-down. After recoupling, the star would return to a “normal” rate of magnetic braking. Gordon et al. (2021) argued in favor of this hypothesis based on the rotation period distribution of K2. Furthermore, Curtis et al. (2020) showed that two-zone angular momentum models, such as those by Spada & Lanzafame (2020) can generally reproduce the stalled braking behavior.

Finally, Reinhold et al. (2019); Reinhold & Hekker (2020) suggested that the gap is created by a transition from dark spot- to bright facula-dominance in stars' photometric variability, as evidenced by stars in the gap having smaller variability amplitudes. They hypothesized that stars in the gap have mutually canceling spots and faculae, resulting in a smaller amplitude that makes the detection of rotation in the gap more difficult. This hypothesis is at least partially supported by a dip in photometric amplitudes in the gap.

Understanding how these features arise in stellar rotation distributions, and how and whether they vary throughout the Galaxy, will reveal new insights to (1) the generation of magnetic braking in rapidly rotating, young stars, (2) the stalling of magnetic braking and the weakening of activity below the detection threshold, (3) the behavior of stellar interiors as they depart from rigid-body rotation, and (4) the formation of star spots and faculae in stars other than the Sun.

1.2 Why TESS?

While *Kepler* generated a revolution and continues to produce new results, it is fundamentally limited in the insights it can deliver. *Kepler* focused on a single patch of sky, probing a single sample of the Milky Way's stars. Conclusions that are drawn from the *Kepler* period distribution must be vetted in other samples to determine whether they are common to all stars or unique to that part of the Galaxy. K2 observed multiple fields across the ecliptic plane and recovered some features like the period gap in each field (e.g., Gordon et al. 2021). However, K2 was limited by the time baseline, reaching periods just shy of 40 days due to its 80-day observing campaigns in each field. As a result, it falls short of seeing the upper edge or the K-dwarf dip seen by *Kepler*. To understand how the features in the rotation period distribution arise, we need (1) more precise period measurements to sharpen the features, (2) in new parts of the sky, (3) with a long enough time baseline to observe the slowest-rotating main sequence stars.

The Transiting Exoplanet Survey Satellite (Ricker et al. 2015) surveys the entire sky in its search for planets around other stars. During its first two years of operations, it collected full-frame images (FFIs) of all targets at 30-minute cadence. It surveyed each ecliptic hemisphere in 13 consecutive, 27-day sectors that partially overlapped at the ecliptic poles, carving out two continuous viewing zones (CVZs) observed for nearly a year each. While TESS is less photometrically precise than *Kepler* (Vanderspek et al. 2018), the FFI cadence equals *Kepler*'s long cadence mode, so they have equal time resolution for rotation period searches. Furthermore, the time baseline of the TESS CVZs is long enough to capture three or more rotations of the most slowly rotating stars, e.g., the M-dwarfs rotating at 100 days in *Kepler*. Finally, the CVZs point in different directions from the *Kepler* field, giving us access to fundamentally different populations of stars (see Figure 1.2. The stars in the CVZs are prime targets to look for signatures of rotation.

1.3 Why Deep Learning?

Conventional rotation period searches have utilized various time-frequency analysis tools including Lomb-Scargle periodograms (LSP; Lomb 1976; Scargle 1982; Feiden et al. 2011; VanderPlas 2018), autocorrelation functions (ACF; McQuillan et al. 2013, 2014), and wavelet power spectra (WPS; Mathur et al. 2010; García et al. 2014a; Santos et al. 2019). LSP generates power spectra for time series with unequal time spacing, such as ground-based light curves. Using the proper normalization, as the spacing approaches uniformity, the LSP approaches the classical Fourier transform (VanderPlas 2018). ACF

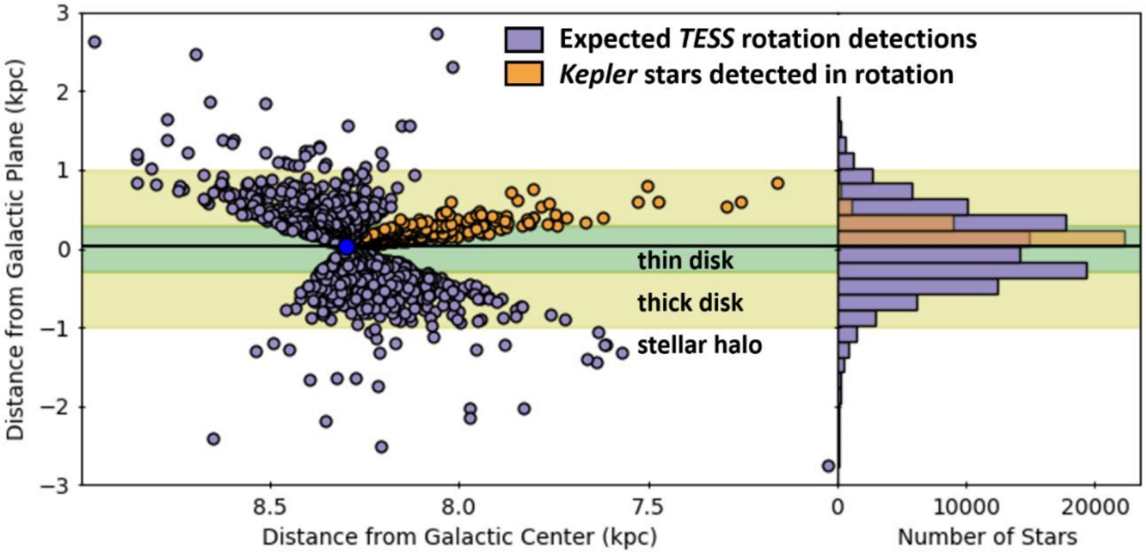

Figure 1.2: While *Kepler* pointed along the Galactic disk, the TESS continuous viewing zones point further out. If we assume the same yields of rotation period as a function of temperature and brightness as *Kepler*, TESS has the potential to deliver more periods of fundamentally different populations of stars than *Kepler*.

involves convolving a signal with itself to find time lags at which the signal is self-similar. They are ideal for equally-spaced rotational light curves with persistent star spot groups, but the ACF weakens when spots evolve on time scales of a few rotation periods or less. McQuillan et al. (2014) used ACF to produce the first *Kepler* rotation period distribution. Finally, WPS are produced by convolving wavelet kernels of varying widths with a signal to pick out signals on different time scales. They are fundamentally different from LSP and ACF in that WPS are two-dimensional representations and show periodicity over time. Santos et al. (2019, 2021) used ACF and WPS to measure periods for more than 50,000 *Kepler* stars. While all three methods do well for signals with strong periodicity, they are also sensitive to periodic and quasi-periodic noise and contamination in time series.

While TESS light curves are, in principle, ideal for rotation period searches, they come with complicated systematics that are difficult to disentangle. TESS's unique 2:1 resonance orbit of the Earth-Moon system subjects the detectors to earthshine and moonlight on the

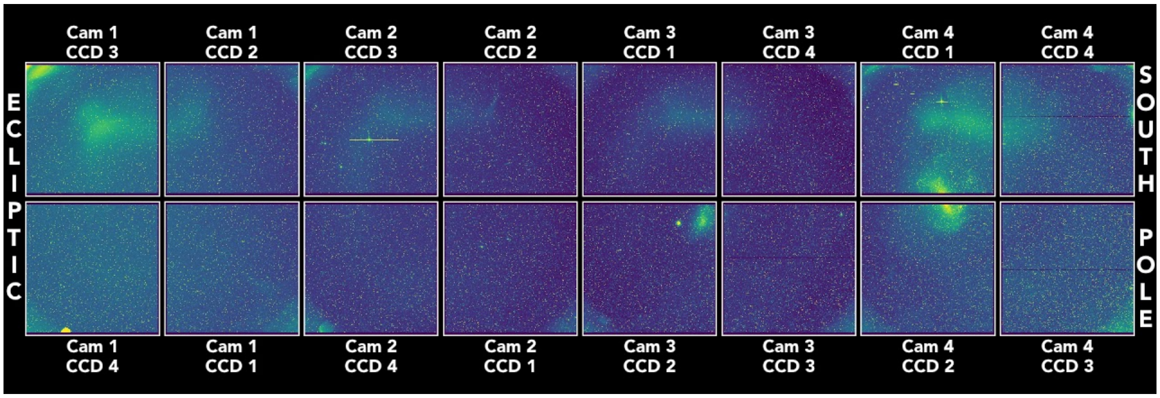

Figure 1.3: A snapshot of the full set of TESS detectors in sector 1, from "TESS: The Movie" by Ethan Kruse (`https://www.youtube.com/watch?v=76xguUB6yE4`). The video illustrates the complicated systematics in TESS throughout the sector produced by earthshine, moonlight, and more. The largest effects are seen in the snapshot as glares in the top row of CCDs.

timescale of the orbit, 13.7 days. The earthshine itself has time-varying signals within it, such as a 1-day modulation from the rotation of the Earth. Figure 1.3 shows a snapshot of the full set of TESS detectors during sector 1. Earthshine can be seen here as a glare in the top row of CCDs. Besides earthsine, TESS encounters systematics related to angular momentum dumps, detector heating, data downlinks, and more, all on timescales that interfere with astrophysical signals. Because of these effects, throughout a sector the TESS detectors encounter systematics on different pixels at different times and with varying intensity, making them incredibly difficult to correct.

The systematics attenuate coherent signals on timescales longer than 13.7 days. This affects the light curves of rapid rotators less, and conventional rotation searches have been largely successful at measuring periods shorter than 13 days in TESS (Canto Martins et al. 2020; Avallone et al. 2022; Colman 2022; Holcomb et al. 2022). However, the same searches have struggled to recover longer periods. Without assuming any prior on the period, the conventional period-finding methods pick out the signal injected by TESS systematics. Lu et al. (2020), used priors on the period in the form of temperature, photometric variability range, and other measurements, and while they recovered some periods longer than 13.7 days, they still encountered a 27-day barrier associated with TESS sector-to-sector stitching.

Many public pipelines exist that attempt to remove systematics from TESS data. We outline some later in Section 4.1. While each pipeline makes different, but well-motivated choices about how to deal with the systematics, each decision runs the risk of accidentally removing stellar signal. Several pipelines indeed have been shown to remove stellar signals along with the systematics, especially when their timescales coincide (Hattori et al. 2022). Rather than trying to remove the systematics at the risk of removing astrophysical signals, we prefer methods that see the periodicity *and* the noise and disentangle them. This allows us to understand the fundamental barrier that prevents period detections. Deep learning offers a class of such methods.

In a short time, deep learning methods have become pivotal tools in stellar astrophysics. Breton et al. (2021) used random forests to classify and detect rotation signals in *Kepler* light curves, while Lu et al. (2020) used random forests to draw connections between stellar parameters to predict TESS rotation periods. Feinstein et al. (2020) employed convolutional neural networks (CNNs) to identify stellar flares in light curves. CNNs are particularly powerful for their design to work with images or image-like data, which are ubiquitous in astronomy. CNNs can be trained to identify images of many different classes despite contaminating features, making them particularly attractive for our problem with TESS systematics.

1.4 Dissertation Outline

The goal of this dissertation is to understand how the distribution of rotation periods in cool, main-sequence stars is influenced by age, angular momentum evolution, and detection limits. We construct a simulation-driven deep learning approach, which we leverage to estimate periods of stars in the TESS continuous viewing zones, giving us access to a new sample of periods to compare and contrast with *Kepler* and K2.

We begin in Chapter 2 describing our deep learning methods. We describe the simulations underlying the training set, construct a convolutional neural network, and perform a series of training, validation, and test runs to assess the performance of the network on a simulated sample as well as a sample of real stars.

Chapter 3 describes the grid-based approach we use to model stars using rotation. We outline stellar models and the angular momentum law used to describe their rotational evolution, and we describe our modeling framework. We infer gyrochronological ages for a sample of 483 stars with *Kepler* rotation periods and ground-based infrared spectroscopic temperatures and elemental abundances. Using these ages, we validate Galactic chemical evolution trends seen in more massive or more evolved samples, and we explore the biases introduced on inferred masses and ages when metallicity, detailed abundances, or initial rotation conditions are incorrectly assumed.

In Chapter 4 we use the trained neural network to estimate reliable rotation periods for 9,837 TESS stars. We employ new training sets tailored to specific period ranges and the specific light curves we use to search for periods. After comparing and contrasting the new distribution of long TESS periods with *Kepler* and K2, we explore the detectability of periods as a function of temperature, metallicity, age, and convection zone properties to understand the effects of detection limits on the period distribution. We also combine our rotation period measurements with new spot filling fraction measurements from infrared spectroscopy to understand the effects of spottedness on the detectability of rotation.

Finally, in Chapter 5 we summarize the results of our period search and draw final conclusions on the period distribution from TESS. We conclude by discussing directions for future research.

Chapter 2

The Simulation-Driven Deep Learning Framework

Originally published as Recovery of TESS Stellar Rotation Periods Using Deep Learning, *ApJ 927, 219, by Claytor et al. (2022)*

2.1 Background

Stellar rotation is fundamentally linked to the structure and evolution of stars. In the decade since *Kepler*, much has been learned about rotation, feeding into asteroseismology, empowering gyrochronology, and changing the way we think about stellar evolution codes. Rotation period estimates are made possible through a variety of methods. Historically, spectroscopy enabled estimates of rotation velocity due to Doppler red/blue shift from the receding/approaching halves of the stellar disk. The projected rotation velocity could then be used to compute an upper limit on the period if the stellar radius was known. Missions like *CoRoT* (Baglin et al. 2006) and *Kepler* (Borucki et al. 2010) have shifted the paradigm: the majority of period estimates now employ photometry instead of spectroscopy. This works particularly for stars which, like the Sun, exhibit magnetic dark and bright spots that induce periodic variations to the light curves as the stars rotate. Several techniques have been developed in recent years to extract rotation information from spot-modulated stellar light curves. Namely, Lomb-Scargle periodograms (Marilli et al. 2007; Feiden et al. 2011), autocorrelation analysis (McQuillan et al. 2013, 2014), wavelet transforms (Mathur et al. 2010; García et al. 2014a), Gaussian processes (Angus et al. 2018), and combinations of these (Ceillier et al. 2017; Santos et al. 2019; Reinhold & Hekker 2020) have all been used to infer rotation periods from light curves.

Period-finding methods have paved the way for large studies of stellar rotation. Applied to *CoRoT* and *Kepler*, these techniques have delivered tens of thousands of rotation period estimates, which in turn have been used to advance our understanding of stellar and Galactic evolution (e.g., McQuillan et al. 2014; van Saders et al. 2016, 2019; Davenport 2017; Claytor et al. 2020; Amard et al. 2020). The Transiting Exoplanet Survey Satellite (TESS, Ricker et al. 2015) stands to increase the number of inferred periods by an order of magnitude in its ongoing all-sky survey.

Rotation studies have also brought to light the limitations of period detection methods. For example, conventional methods are subject to aliases from multiple groups of star spots (e.g., “double-dipper” stars: Basri & Nguyen 2018), and they still struggle to detect rotation in quiet, Sun-like stars (McQuillan et al. 2014; van Saders et al. 2019; Reinhold & Hekker 2020). Furthermore, the traditional methods do not necessarily reveal a star’s true period. Rather, they reveal the period(s) of latitudes at which star spots form, which may rotate faster or slower than the star’s equator due to surface differential rotation.

Finally, the systematics of TESS have made traditional period searches difficult (Oelkers & Stassun 2018; Canto Martins et al. 2020; Holcomb 2020; Avallone et al. 2022). The lunar-synchronous orbit of TESS has a 13.7-day period, and the telescope is subject to background variations from reflected sunlight causing periodic contamination that is difficult to remove. As a result, dedicated rotation studies struggle to obtain reliable periods longer than about 13 days (e.g., Canto Martins et al. 2020; Holcomb 2020; Avallone et al. 2022). New, data-driven methods are needed to overcome these systematics and recover periods.

Deep Learning is relatively new to astronomy, but in a short time Deep Learning methods have proven to be valuable at mining information from large data sets. Perhaps the most well-known use of Deep Learning is image recognition (e.g., He et al. 2015). Deep neural networks are extremely effective and efficient at processing and classifying 2D images, making them ideal tools to use on astronomical data. Neural networks, and in particular Convolutional Neural Networks (CNNs), efficiently extract information from time series, spectra, and image data. The strength of CNNs comes from their local connectivity, which incorporates the knowledge that neighboring input points are highly correlated. Examples of success using CNNs in astronomy include Hezaveh et al. (2017), who used CNNs to characterize gravitational lenses from image data. Within the realm of stellar astrophysics, Guiglion et al. (2020) used the same techniques to obtain stellar parameters from spectra. Moreover, Feinstein et al. (2020) and Blancato et al. (2020) used CNNs to infer stellar parameters and flare statistics from light curves.

Using CNNs, we predict stellar rotation periods from wavelet transforms of light curves. The use of supervised machine learning requires the existence of a training data set for which the target, in this case the rotation period, is known. This is not yet possible with TESS due to the difficulties of obtaining reliable periods using traditional techniques. Furthermore, while there is some overlap between TESS and *Kepler*, the TESS observations of the *Kepler* field are short, spanning only 27 days for most targets. This is enough to recover and validate short rotation periods (Blancato et al. 2020), and possibly some subset of longer periods (Lu et al. 2020), but not enough to be useful for the broader population of stars in our Galaxy. Moreover, even large rotation samples from *Kepler* are likely contaminated with mismeasured periods (Aigrain et al. 2015). Using a training set of periods obtained with conventional techniques risks imprinting this contamination onto the neural network. To avoid this, we followed the approach of Aigrain et al. (2015) and used a set of synthetic light curves generated from physically motivated star spot emergence models. This is an example of simulation-based inference (e.g., Cranmer et al. 2020), wherein we simulate a physical process and use machine learning to address the inverse problem of inferring the rotation.

We introduce `butterpy`[1], an open-source Python package designed to simulate realistic star spot emergence and synthesize light curves, followed by a description of the input physics of the simulations. After describing our training set, we outline our CNN and the methods we use to train, validate, and test the network. We evaluate our trained neural network on synthesized data sets spanning different period ranges to identify for what periods the network is most predictive. Next, we discuss the network's performance on a small set of real light curves for which rotation periods are known. We also compare our network predictions to periods recovered using conventional methods before finally concluding with thoughts on the feasibility of our methods to recover stellar rotation periods from real TESS light curves.

2.2 Synthetic Light Curves: `butterpy`

Synthesized light curves have several advantages over observed light curves: (1) the true, equatorial period of the simulated star is known, rather than an estimate of the period (which may be wrong), (2) data of any length and cadence can be synthesized, and (3) other physical properties like spot characteristics, differential rotation, and surface activity are known and can be independently probed.

---

[1] `https://github.com/zclaytor/butterpy` (Claytor et al. 2021).

To simulate light curves, we developed `butterpy`, a Python package designed to generate realistic, physically motivated spot emergence patterns faster than conventional surface flux transport codes. We invite the community to extend and modify the spot emergence model in the open-source GitHub repository. The name `butterpy` comes from the butterfly-shaped pattern of spot emergence with time exhibited by the Sun (e.g., Hathaway 2015). We built upon the software developed by Aigrain et al. (2015), which relied on the flux transport models of Mackay et al. (2004) and Llama et al. (2012) to generate dark spot emergence distributions which were in turn used to compute light curves. Aigrain et al. (2015) discuss in detail how well these model light curves match those seen in nature, but broadly they reproduce the solar irradiance and resemble light curve ensembles observed by *CoRoT* and *Kepler*. The original model of Mackay et al. (2004) was designed to reproduce spot emergence patterns of the Sun as well as Zeeman Doppler images of the pre-main-sequence star AB Doradus. Later, Llama et al. (2012) used this model in tandem with exoplanet transit observations to trace the migration of active latitude bands across the surfaces of stars. Aigrain et al. (2015) used the light curves generated from these spot distributions to test the recovery rates of various period detection techniques, which we seek to emulate. We discuss the method and assumptions here for clarity.

2.2.1 Spot Emergence and Light Curve Computation

Like Aigrain et al. (2015), we model star spots as uniformly dark circles on the surface of the star. For this exercise, we do not include bright plage or faculae, nor do we allow for non-uniformity of spot intensity or shape. However, we expect our model to capture most of the variance contained in real light curves. Beyond these basic assumptions, there are several variables to consider regarding the emergence of star spots and their effect on the star's light curve, including the latitudes and rates of emergence, the spot lifetimes, and the rotation speed at the latitude of emergence if the star rotates differentially. While observations of these characteristics on stars other than the Sun are limited, they are very well characterized for the Sun (Hathaway 2015, and references therein). For our model, we therefore start with the properties that are known for the Sun and allow them to vary.

Location and rate of spot emergence

The latitudes of spot emergence on the Sun vary with the Sun's 11-year activity cycle. At the beginning of a cycle, spots emerge within active regions at high latitudes ($\lambda \approx \pm 30^\circ$, Hathaway 2015), and the latitude of emergence migrates toward the equator throughout the rest of the cycle. Before the cycle ends, new spot groups begin forming again at high latitudes, indicating some amount of overlap between consecutive cycles. The repeating decay in spot latitude with time gives rise to a butterfly-like pattern known as a "butterfly diagram". Butterfly patterns have been observed in other stars as well (Bazot et al. 2018; Nielsen et al. 2019; Netto & Valio 2020), but some stars show a random distribution of spot emergence latitudes with time (e.g., Mackay et al. 2004). The width of active latitude bands has also been shown to differ even for Sun-like stars (Thomas et al. 2019). In our model, we allow for either a random or butterfly-like spot emergence between a minimum and maximum latitude that are unique for each star. For the butterfly pattern, spots begin the cycle emerging at a latitude $\lambda_{\rm max}$, decaying exponentially with time to latitude $\lambda_{\rm min}$ at the end of the cycle (Hathaway 2011).

As for longitude, spots on the Sun tend to emerge in groups, either next to existing spots, or in some cases antipolar to existing spots (Hathaway 2015). Less often, spots will emerge at random longitudes, not necessarily associated with any existing spot groups. We respectively refer to these two cases as correlated and uncorrelated active regions. In our simulations, we follow the approach of Aigrain et al. (2015), dividing the stellar surface into 16 latitude and 36 longitude bins; the probability of spot emergence is distributed across these bins. To account for the relative likelihood of correlated and uncorrelated emergence, bins already containing active regions are assigned a higher probability of emergence.

The rates of sunspot emergence change with spot area and with time throughout the activity cycle. Schrijver & Harvey (1994) expressed the number of spots emerging in area interval (a, $a + \mathrm{d}a$) and time interval (t, $t + \mathrm{d}t$) as $r(t)a^{-2}\,\mathrm{d}a\,\mathrm{d}t$, where $r(t)$ represents the time-varying emergence rate amplitude, the active region area a is in square degrees, and t is the time elapsed in the activity cycle, ranging from zero to one. For the time dependence, spots emerge very slowly at the beginning, more rapidly in the middle, and slowly again at the end (Hathaway et al. 1994). Mackay et al. (2004) modeled this using a squared sine function: $r(t) = A\sin^2(\pi t)$. The activity level A is an adjustable scale factor controlling both the average rate of spot emergence and the amplitude of light curve modulation of a single spot. It is defined such that $A = 1$ for the Sun.

Latitudinal Differential Rotation

We define asterographic longitude such that $\phi = 0$ always faces the Earth. As a consequence, spots move in longitude as the star rotates. The Sun rotates more rapidly near the equator than at the poles, a phenomenon known as "latitudinal differential rotation" (henceforth just "differential rotation"). While differential rotation is more difficult to observe on other stars, some stars may exhibit "anti-solar" differential rotation, wherein the equator rotates more slowly than the poles. This has been observed particularly in slowly-rotating stars (e.g., Rüdiger et al. 2019). In our model, we allow for solar-like, anti-solar, and solid-body rotation. Following Aigrain et al. (2015), we model the differential rotation profile as

$$\begin{aligned} \phi_k(t) &= \phi_k(t_{\mathrm{max},k}) + \Omega(\lambda_k)(t - t_{\mathrm{max},k}), \\ \Omega(\lambda_k) &= \frac{2\pi}{P_{\mathrm{eq}}}(1 + \alpha \sin^2 \lambda_k). \end{aligned} \tag{2.1}$$

Here, λ_k and ϕ_k denote the asterographic latitude and longitude of spot k. $t_{\max,k}$ is the time at which the spot achieves maximum flux, Ω is the angular velocity at latitude λ_k, and α is the differential rotation shear parameter. To include anti-solar, solid-body, and solar-like profiles, we allow α to range from -1 to 1.

Spot-Induced Flux Modulation

Once spot emergence is determined, we simulate spot evolution and flux modulation based on the simplified model of Aigrain et al. (2012, 2015). They take the photometric signature $\delta F_k(t)$ of a single spot k to be

$$\begin{aligned} \delta F_k(t) &= f_k(t)\ \max\{\cos\beta_k(t),\ 0\}, \\ \cos\beta_k(t) &= \cos\phi_k(t)\cos\lambda_k\sin i + \sin\lambda_k\cos i, \end{aligned} \tag{2.2}$$

where $\beta_k(t)$ is angle between the spot normal and the line of sight, accounting for projection on the stellar surface. The inclination i is the angle between the rotation axis and the line of sight, and λ_k and $\phi_k(t)$ are again the latitude and longitude of the spot. The factor f_k is the amount of luminous flux removed if spot k is observed at the center of the stellar disk. Aigrain et al. (2015) used an exponential rise and decay to model the rapid emergence and slow decay of single spots, but we employ a two-sided Gaussian to avoid cusps in the curve of spot area with time while preserving the same emergence and decay behavior:

$$\begin{aligned} f_k(t) &= f_k^{\max}\exp\left[-\left(t-t_{\max,k}\right)^2/\tau^2\right], \\ \tau &= \begin{cases} \tau_{\text{emerge}} = \max\left\{2\text{ d},\ \dfrac{\tau_{\text{spot}}}{5}P_{\text{eq}}\right\},\ t \leq t_{\max,k} \\ \tau_{\text{decay}} = \tau_{\text{spot}}P_{\text{eq}},\ t > t_{\max,k}, \end{cases} \end{aligned} \tag{2.3}$$

where $f_k^{\max}$ is the flux removed by spot k at the time of maximum emergence $t_{\max,k}$, τ is the relevant emergence or decay timescale, and $\tau_{\rm spot}$ is a dimensionless parameter used to relate the emergence and decay timescales to the equatorial rotation period $P_{\rm eq}$. We verified that our results were not sensitive to the choice of exponential or Gaussian emergence and decay, so the choice is purely philosophical. Like Aigrain et al. (2015), we parametrized the emergence and decay timescales as multiples of the equatorial rotation period. The form of their emergence timescale was chosen so that, in general, emergence is five times faster than decay, with a minimum possible emergence timescale of two days. We adopt the same behavior for our simulations. In the simple model of Aigrain et al. (2012), $f_k^{\max}$ takes into account the spot area and contrast, but the model of Aigrain et al. (2015) relates this factor to the strength of the magnetic field:

$$f_k^{\max} = 3 \times 10^{-4}\ A\ B_{r,k}/\langle B_{r,k}\rangle_k, \tag{2.4}$$

where A is the activity level, and the constant is chosen such that $A = 1$ reproduces approximately Sun-like behavior.

With this expression, the single-spot luminous flux modulation is proportional to the radial (or vertical) magnetic field component at that spot. The magnetic field strength or magnetic flux is proportional to the area of the active region, which van Ballegooijen et al. (1998) derive using the angular width of magnetic bipoles emerging from the active region:

$$B_r^{\pm}(\theta,\ \phi) = B_{\max}\left(\frac{\beta_{\rm init}}{\beta_0}\right)^2 \exp\left[-\frac{2(1-\cos\beta_{\pm}(\theta,\ \phi))}{\beta_0^2}\right], \tag{2.5}$$

where $B_r^{\pm}$ is the radial component of the magnetic field near either the positive or negative bipole, $B_{\max}$ is the initial peak magnetic field strength in the active region, $\beta_{\rm init}$ is the angular width of a single bipole, β_0 is the angular width (in degrees) of the bipole at the time the active region is inserted into the model, accounting for diffusion, and $\beta_{\pm}$ is the asterocentric angle between a field point and one of the bipoles.

van Ballegooijen et al. (1998) assumed that the bipole width $\beta_{\rm init}$ is proportional to the angular separation between the positive and negative poles, which they call $\Delta\beta$, with a proportionality factor of 0.4. Assuming spots form within ten degrees of the active region bipoles, the value of the exponential factor differs from unity by less than one percent. For this reason, we approximate the exponential factor as unity. Thus, at the location of a star spot, Equation (2.5) simplifies to

$$B_r \approx B_{\rm max} \left(\frac{0.4\Delta\beta}{\beta_0} \right)^2 . \tag{2.6}$$

Combining this with Equation (2.4),

$$f_k^{\rm max} = 3 \times 10^{-4} A \left(\frac{\Delta\beta_k}{\langle \Delta\beta_k \rangle_k} \right)^2 . \tag{2.7}$$

van Ballegooijen et al. (1998) and Mackay et al. (2004) consider a range of bipole widths from about 3.5° to 10°, which we adopt for our models. The distribution of $\Delta\beta$ is the same for every star, so $\langle \Delta\beta_k \rangle_k$ is effectively constant. While some low-mass stars have been suggested to have much larger spots covering substantial fractions of the surface, these stars will still be represented in our training set by models with many small spots. Putting it all together, we have a final system of equations to describe the change in luminous flux from a single spot:

$$
\begin{aligned}
\delta F_k(t) &= f_k(t)\exp\left[-\left(t - t_{\mathrm{max},k}\right)^2/\tau^2\right],\\
f_k(t) &= 3\times 10^{-4} A \left(\frac{\Delta\beta_k}{\langle\Delta\beta_k\rangle_k}\right)^2 \max\{\cos\beta_k(t),\ 0\},\\
\tau &= \begin{cases} \max\left\{2\ \mathrm{d},\ \dfrac{\tau_{\mathrm{spot}}}{5}P_{\mathrm{eq}}\right\},\ t \le t_{\mathrm{max},k}\\ \tau_{\mathrm{spot}}P_{\mathrm{eq}},\ t > t_{\mathrm{max},k}\end{cases},\\
\cos\beta_k(t) &= \cos\phi_k(t)\cos\lambda_k\sin i + \sin\lambda_k\cos i.
\end{aligned}
\tag{2.8}
$$

This depends on $\Delta\beta_k$, λ_k, $\phi_k(t)$, and $t_{\mathrm{max},k}$, which are unique to each spot; and A, τ_{spot}, P_{eq}, and i, which are unique to each star.

2.2.2 Training Set

Using the model in `butterpy`, we generated one million light curves at thirty-minute cadence and one-year duration to match the TESS Full-Frame Images (FFIs) in the continuous viewing zones (CVZs). The simulation input parameters and their chosen distributions are listed in Table 2.1. While these parameters for real stars tend to correlate with one another (e.g., faster-rotating stars tend to be more active), we intentionally left the parameters mutually uncorrelated so as not to imprint our choices on the neural network predictions. The input distribution acts as a prior on the predictions of a neural network. Uniform distributions serve as uninformative ("flat") priors. We therefore chose all our distributions to be uniform or log-uniform (i.e., uniform under a log-transformation) to avoid applying a strong prior in the neural network predictions. We sampled periods uniformly from the range [0.1, 180] days, assuming no relationship between period and activity. The period range was chosen to be as wide as possible to simulate the fastest-

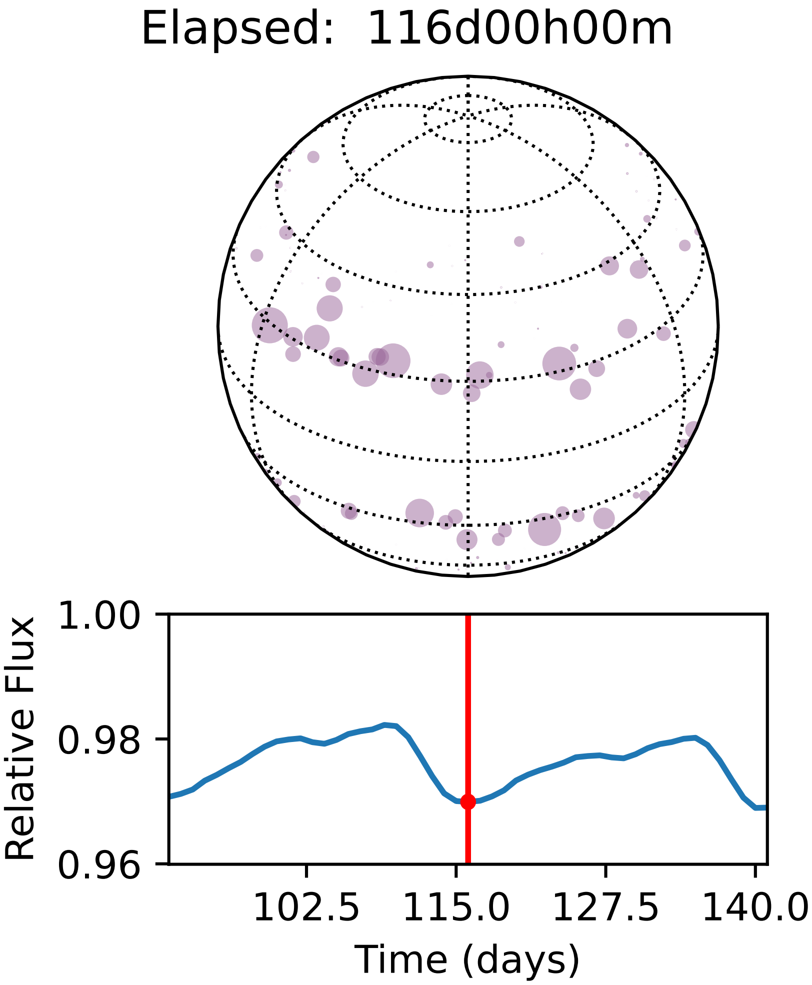

Figure 2.1: An example of a `butterpy` simulation of spot evolution and light curve generation.

rotating stars ($P_{\text{eq}} \approx 0.1$ day) while also capturing anything that would go through at least two rotations under observation in the TESS CVZs (the total baseline is 350 days, so an object with $P_{\text{eq}} = 180$ will go through almost two rotations in that time). We chose the remaining distributions and ranges to reflect those of Aigrain et al. (2015), which were chosen to resemble and slightly exceed the distributions seen in *Kepler* stars. We made minor adjustments to the ranges of activity level and differential rotation shear to search a broader parameter space. Figure 2.1 illustrates an example simulation, showing the distribution of spots on the surface as well as their impact on the observed light curve.

Table 2.1: Distribution of Simulation Input Parameters

Parameter	Range	Distribution
Equatorial rotation period P_{eq}	0.1 – 180 days	uniform
Activity level A	0.1 – 10 × solar	log-uniform
Activity cycle length T_{cycle}	1 – 40 years	log-uniform
Activity cycle overlap T_{overlap}	0.1 year – T_{cycle}	log-uniform
Minimum spot latitutde λ_{min}	0° – 40°	uniform
Maximum spot latitude λ_{max}	$\lambda_{\mathrm{min}} + 5^\circ$ – 80°	uniform
Spot lifetime τ_{spot}	1 – 10	log-uniform
Inclination i	0° – 90°	uniform in $\sin^2 i$
Latitudinal rotation shear $\Delta\Omega/\Omega_{\mathrm{eq}}$	0.1 – 1 (50%)	log-uniform
	0 (25%)	
	-1 – -0.1 (25%)	log-uniform

Note. We adopted the distributions used by Aigrain et al. (2015) with minor modifications: (1) we sampled a broader range of periods and activity levels, (2) we used a uniform distribution of periods so as not to impart unwanted prior on the neural network prediction, (3) we include anti-solar differential rotation by allowing the shear parameter to be negative.

2.2.3 TESS Noise Model

To ensure the training light curves properly emulate real TESS light curves, the training set must exhibit TESS-like noise. Aigrain et al. (2015) used light curves from quiescent *Kepler* stars to achieve this. In their study, a sample of stars from McQuillan et al. (2014) with no significant period detection served as the quiescent data set. Because there are no existing bulk period measurements for stars in the CVZs, we must find another means of simulating TESS noise.

While TESS is a planet-finding mission, the southern CVZ contains thousands of galaxies which should have roughly constant brightness with time. Any changes in the light curves of these galaxies would be due solely to TESS instrument systematics. Furthermore, while galaxies are extended on the sky and not point sources, TESS's large ($21''$) pixel size means that a typical aperture is larger than most galaxies in the TESS Input Catalog. Indeed, 85% of SCVZ galaxies fit in the width of two pixels, and 93% fit within three

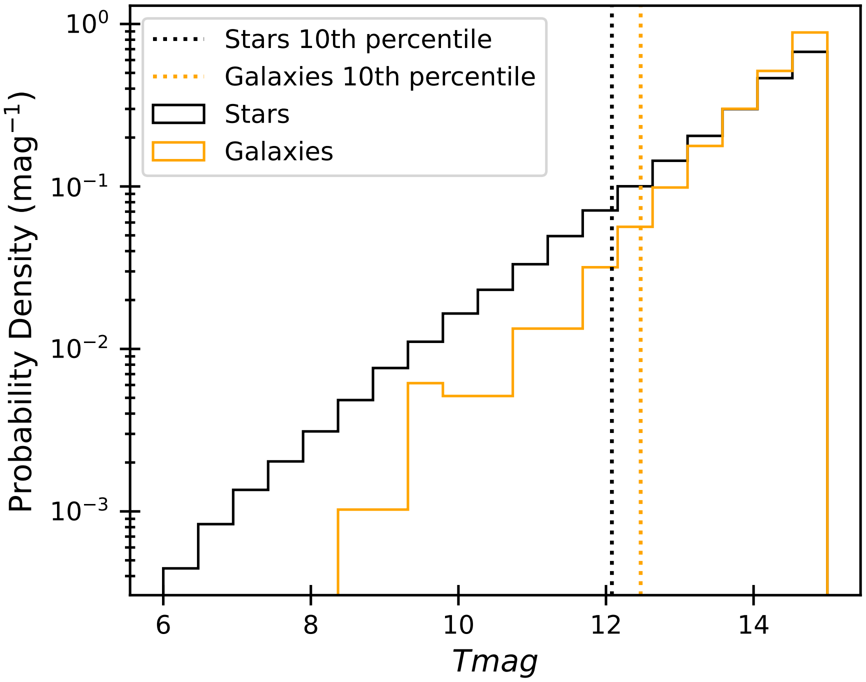

Figure 2.2: Brightness distributions of stars and galaxies in the TESS Southern Continuous Viewing Zone. The galaxies follow a similar brightness distribution to the stars in the SCVZ, especially toward the faint end where the majority of objects lie. Because the distributions are similar, the training light curves, which use the galaxy light curves to emulate noise, are representative of real distributions of stars' brightness and noise properties.

pixels. Thus, as long as we choose sufficiently large apertures, the galaxies are effectively point-like, and the galaxy light curves should reasonably resemble light curves of quiescent stars in TESS.

We selected roughly 2,000 galaxies in the southern CVZ with $Tmag \leq 15$ as our quiescent sample, removing a handful of galaxies known to be active and in the Half-Million Quasars catalog (Flesch 2015). Figure 2.2 shows the brightness distributions of galaxies and stars in the TESS SCVZ with vertical lines indicating the 10th percentiles of each distribution. The galaxies are distributed in apparent brightness similarly to the stars in the TESS SCVZ, so the training light curves will have distributions of apparent brightness and photometric precision resembling the distributions of real stars.

We queried FFI cutouts from the Mikulski Archive for Space Telescopes (MAST) using `Lightkurve` and `TESScut` (Lightkurve Collaboration et al. 2018; Brasseur et al. 2019). Then, we performed background subtraction and aperture photometry on each source using `Lightkurve` regression correctors, following Lightkurve Collaboration (2020). To summarize, aperture masks were chosen using the `create_threshold_mask` function in `Lightkurve`. This method selects pixels with fluxes brighter than a specified threshold number of standard deviations above the image's median flux value. We specified thresholds based on the target's brightness to exclude background pixels from the aperture. Once the raw light curve was computed, the regression correctors fit principle components of the time-series images and subtracted the strongest components from the raw light curve. All sector light curves for a source were then median-normalized and stitched together to form the final "pure noise" light curve.

The galaxy light curves were linearly interpolated to each TESS cadence to fill gaps, whether for missing observations or entire missing sectors. Cadences missing at the beginning or end of the light curve were filled with the light curve's mean flux value. Finally, a galaxy light curve was chosen at random to be convolved with each of the synthetic light curves, yielding our final set of simulated TESS-like light curves. We note that while the light curves were median-normalized, this should not affect the intrinsic brightness or effective signal-to-noise ratio (SNR) of the light curves. The SNR can be thought of as the spot modulation amplitude divided by the photometric precision, both of which are defined relatively and are therefore preserved under median-normalization. Thus, the ranges of brightness and photometric precision of our light curves reflect the underlying set of galaxy light curves, which are representative of stars in the TESS SCVZ. We divided the set of 2,000 galaxies into two sets of 1,000: one set to be convolved with light curves from the training partition, and one for the validation and test partitions (see Section 2.4 for more about data partitioning).

Table 2.2: Convolutional Neural Network Architecture

Layer Type	Number of Filters	Filter Size	Stride	Activation	Output Size
Input image	-	-	-		64×64
Conv2D	8	3×3	1×1	ReLU	$62 \times 62 \times 8$
MaxPool2D	1	1×3	1×3	-	$62 \times 20 \times 8$
Conv2D	16	3×3	1×1	ReLU	$60 \times 18 \times 16$
MaxPool2D	1	1×3	1×3	-	$60 \times 6 \times 16$
Conv2D	32	3×3	1×1	ReLU	$58 \times 4 \times 32$
MaxPool2D	1	1×4	1×4	-	$58 \times 1 \times 32$
Flatten	-	-	-	-	1856
Dense	-	-	-	ReLU	256
Dense	-	-	-	ReLU	64
Dense	-	-	-	Softplus	2

Note. We use three 2D convolution layers, each with ReLU activation and max-pooling. Our implementation uses 2D max-pooling with a 1-dimensional kernel to achieve pooling in the time dimension but not the frequency dimension. This choice preserves frequency resolution but achieves a small amount of translational invariance in the time dimension. The output of the convolution block is flattened to a 1-dimensional array and passed through three fully connected (dense) layers, with ReLU and finally softplus output, to yield two numbers: the rotation period and its uncertainty.

2.3 Data Processing/Wavelet Transform

There are several options for input to a neural network to predict rotation periods. One could use the light curve directly; Blancato et al. (2020) suggest this as the best way to obtain periods using neural networks without loss of information. However, using the light curve as input means that the information conveying periodicity is temporally spread out. While neural networks can certainly learn to predict periods this way, a frequency representation concentrates the period information to one location in input space. Lomb-Scargle periodograms (Lomb 1976; Scargle 1982; Feiden et al. 2011) and autocorrelation functions (McQuillan et al. 2013, 2014) are two tried-and-true methods of period estimation that have some promise as input to neural networks. While these methods are effective at concentrating periodicity information to one location, real stars' observed periodicity can

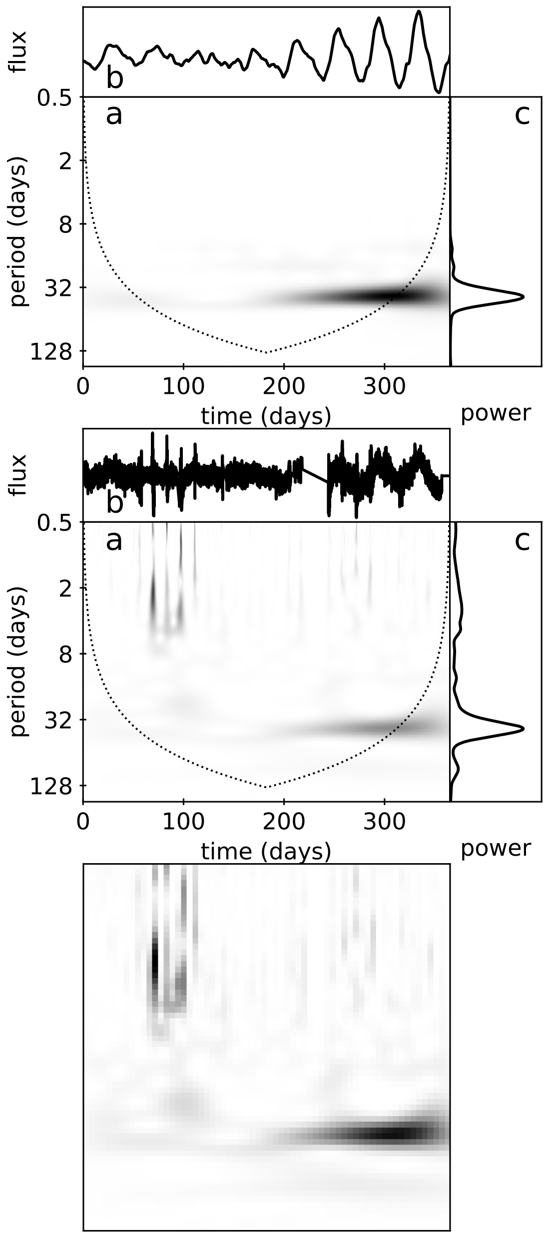

Figure 2.3: *Top:* Morlet wavelet transform (a) of a noiseless light curve, shown with the light curve (b) and global wavelet power spectrum (c). *Center:* plots for the same light curve convolved with TESS noise and re-stitched. The dotted curve marks the cone of influence, below which the power spectrum is susceptible to edge effects. *Bottom:* example of a binned wavelet power spectrum we used to train our neural network. The 64×64-pixel array, without labels, is what is fed into the network. Neural networks can learn to ignore the noise and pick out stellar signals.

change with time due to differential rotation. Lomb-Scargle and autocorrelation methods average over these changes, potentially blurring out interesting evolution.

The continuous wavelet transform (Torrence & Compo 1998) has also been used to identify rotation periods from stellar light curves (Mathur et al. 2010; García et al. 2014a; Santos et al. 2019). When applied to time series, the wavelet transform creates a 2D image of frequency versus time; thus, it has the bonus of elucidating changes in periodicity with time. Additionally, the wavelet transform's two-dimensional nature makes it an ideal partner to Deep Learning approaches. Deep Learning has been applied to wavelet transform representations in the fields of physiology (Zhao & Zhang 2005), economics (Bao et al. 2017), and more. We chose the wavelet transform as the best representation to localize periodic information while allowing the tracing of spot evolution, and as the most natural representation to leverage the decades of advances in image classification and analysis with Deep Learning.

We used the continuous wavelet transform implemented in `SciPy` (Virtanen et al. 2020) with the power spectral density correction of Liu et al. (2007). Using a Morlet wavelet, we computed wavelet power spectra for both the noiseless and noisy light curves in our training set. Examples of both noiseless and noisy power spectra are shown for the same simulated star in Figure 2.3. We then rebinned the power spectra to 64×64 pixels and saved them as arrays for fast access. Larger binned sizes were tested (e.g., 128×128) and showed no significant change in performance.

We ran several tests with the period axis of the wavelet power spectra, trying maximum periods of 128, 150, and 180 days, before settling on 180 days (i.e., half the observing window) for the final data products. In the tests with 128 and 150 days, the neural network successfully predicted periods longer than the maximum visible period in the periodogram, albeit at lower success rates. This suggests that neural networks can predict periods even when the period at maximum power is beyond the range of the plot, consistent with the results of Lu et al. (2020). This is encouraging for period predictions for stars outside the TESS continuous viewing zones, where observations are substantially less than a year in duration. In the end, we chose 180 days as the maximum value on the period axis to preserve the strongest rotation signals in as many objects as possible.

In addition to `butterpy`, the training light curves and wavelet power spectra are available on MAST as a High Level Science Product via doi:10.17909/davg-m919[2].

2.4 Convolutional Neural Network

We used a CNN to predict rotation periods from wavelet transforms. Table 2.2 outlines the CNN architecture. We used a sequence of 2D convolution layers with rectified linear activation ("rectifier" or "ReLU") followed by 1D max-pooling in the time dimension. The ReLU activation function has the form $f(x) = \max(0,\ x)$. Its nonlinearity allows the model to represent complex functions, and ReLU learns faster than other nonlinear activation functions. Max-pooling is used to down-sample input and impart a small amount of translational invariance. The shapes of the convolution and pooling kernels were chosen to impart equivariance in the frequency dimension (no pooling, since frequency is what we want to estimate) and translational invariance in the time dimension. This means that the CNN will treat periodic signals the same regardless of when they occur in the wavelet power spectrum (see Ch. 9 of Goodfellow et al. 2016).

The output of the convolution layers is then flattened to one dimension and fed into a series of three fully connected layers, also with ReLU activation. The final layer uses softplus activation, which has the form $f(x) = \ln(1 + e^x)$. A smooth approximation to the rectifier, softplus activation ensures positive output while preserving differentiability.

---

[2] `https://archive.stsci.edu/hlsp/smarts/`

The final layer outputs two numbers, which represent the rotation period and the period uncertainty.

The 2D wavelet power spectra were used as input to our neural network, while the corresponding model rotation periods served as the target output. Target periods were min-max scaled over the entire data set to the range [0, 1]. Each power spectrum array was min-max scaled to the range [0, 1] separately—using the min and max over the entire data set suppressed lower-amplitude signals and substantially impaired performance.

Our full data set of one million examples was partitioned into three sets for model training, validation, and testing. The training set consisted of 80% and was used to fit the model weights. The validation set (10%) was used for early stopping (we stop training when the validation loss does not improve over a window of 10 training epochs to avoid overfitting) and for choosing the optimal hyperparameters. The test set (10%) was used for final model evaluation.

We used the Adam optimizer (Kingma & Ba 2014), which allows for a variable learning rate, with negative log-Laplacian likelihood as the loss function. This loss function allows us to predict both the rotation period and its error (a process known as heteroskedastic regression), indicating which period predictions are more reliable than others. It has the form

$$\mathcal{L} = \ln{(2b)} + \frac{|P_{\text{true}} - P_{\text{pred}}|}{b}, \tag{2.9}$$

where b is taken to represent the predicted uncertainty.

Maximizing the log-likelihood of the Laplace distribution is equivalent to minimizing the mean absolute error instead of the mean-squared error, or predicting the median period instead of the mean. This also means that in cases where the neural network cannot predict with high confidence, predictions will be biased toward the median of the period range. Formally, the Laplace distribution has variance $2b^2$ and standard deviation $\sqrt{2}b$. Since we use the predicted uncertainty only to determine the relative credence of predictions, the number should not be considered statistically formal. With this in mind, we leave the notation in terms of b to represent the uncertainty for simplicity and to discourage a statistically formal interpretation of our uncertainty.

With 800,000 input-output pairs in the training set, our model takes roughly 3 hours until fully trained on a single NVIDIA RTX2080. Once trained, evaluation on the test input of 100,000 wavelet power spectrum plots takes less than a minute.

2.5 Results

We trained and evaluated the neural network on year-long simulations of both noiseless and noisy wavelet transform images. We additionally used Lomb-Scargle periodograms, autocorrelation functions, and wavelet transforms to obtain independent period estimates from both the noiseless and noisy data.

Aigrain et al. (2015) performed blind injection-recovery exercises on synthesized *Kepler*-like light curves to assess the reliability of conventional period-detection methods. On average, the teams recovered periods with 10% accuracy in $\sim$70% of cases in which periods were obtained. We adopt this 10% accuracy threshold as our success metric, which we designate "acc10." In addition to acc10, we also quantify results with "acc20," mean absolute percentage error (MAPE), and median absolute percentage error (mAPE), defined as follows. If we define the absolute percentage error of example i to be $\epsilon_i =$

$|P_{\mathrm{pred},i} - P_{\mathrm{true},i}|/P_{\mathrm{true},i}$, then our recovery metrics are

$$
\begin{aligned}
\mathrm{MAPE} &= \frac{1}{N}\sum_{i}^{N} \epsilon_i \\
\mathrm{mAPE} &= \mathrm{median}\{\epsilon_i\} \\
\mathrm{acc10} &= \frac{1}{N}\sum_{i}^{N} H(0.1 - \epsilon_i) \\
\mathrm{acc20} &= \frac{1}{N}\sum_{i}^{N} H(0.2 - \epsilon_i),
\end{aligned}
\tag{2.10}
$$

where $H(x - \epsilon_i)$ is the Heaviside or unit step function.

Before commenting on our period recovery, it is important to note the differences in our light curve sample from that of Aigrain et al. (2015). The most important differences are in the range of activity level and the light curve pre-processing. Our sample spans a wider range of activity levels, ranging from 0.1 to 10 times solar, as opposed to 0.3 to 3 times solar in Aigrain et al. (2015). The logarithmic scale of the distribution ensures that the increase in range evenly adds examples to the high- and low-activity ends. Thus, despite having higher-amplitude examples in our sample, there should be enough lower-amplitude examples to compensate, preserving the comparability of our summary statistics to those of Aigrain et al. (2015). Light curve pre-processing differs because of the differences in the *Kepler* pipeline and our custom TESS FFI pipeline. In principle, the *Kepler* pipeline more aggressively removes systematics, so the Aigrain et al. (2015) simulated light curves are cleaner than ours.

2.5.1 Period recovery using conventional methods

We recovered periods from our sample of noisy light curves using Lomb-Scargle periodograms (LSP, as implemented in `Lightkurve`, Lightkurve Collaboration et al.

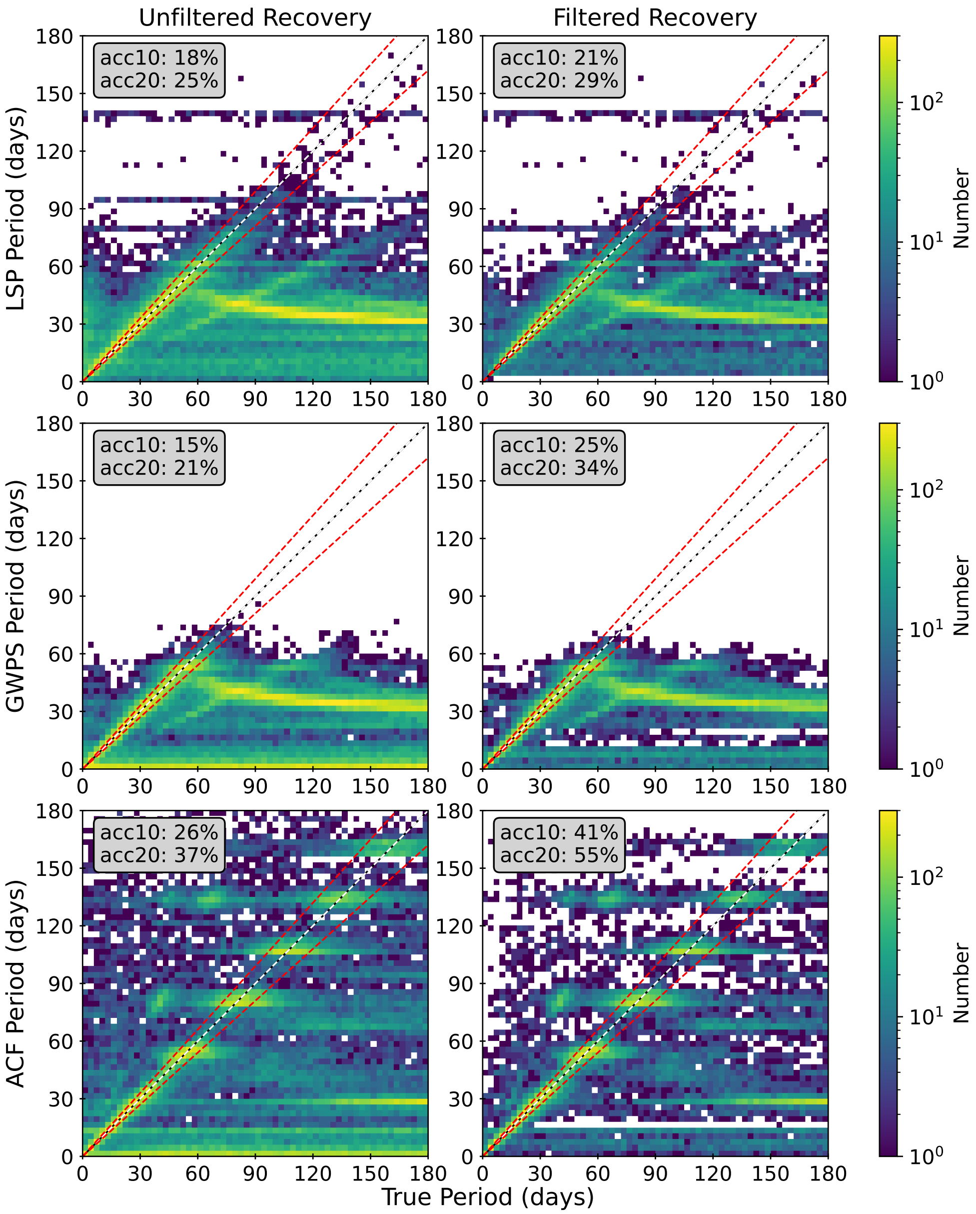

Figure 2.4: Period recovery using Lomb-Scargle periodogram (LSP, top), global wavelet power spectrum (GWPS, middle), and autocorrelation function (ACF, bottom). The left column shows the unfiltered period recovery, while the right column shows recovery filtered or "precleaned" using periodogram peak significance metrics: false alarm probability for LSP and peak prominence for GWPS and ACF. "acc10" represents fraction of periods recovered to within 10% accuracy, while "acc20" is the recovery to within 20%. ACF has the highest overall success, but the recovery worsens significantly at periods longer than about 30 days. Precleaning the sample based on peak significance improves recovery, but only marginally in most cases; aliases still dominate the predictions for true periods longer than about 50 days.

2018), autocorrelation functions (ACF, McQuillan et al. 2013, and as implemented in `starspot`, Angus et al. 2018), and global wavelet power spectrum (GWPS, as implemented in `SciPy`, Virtanen et al. 2020). The recovery results are summarized in Figure 2.4. In each panel, objects falling within 10% of the line $y = x$ are successfully recovered according to our metric. In addition to showing predictions for the entire test set (left column), we also filtered predictions based on various periodogram peak significance metrics to demonstrate how recovery rates improve with confidence in the measurement. We removed the worst half of the data based on peak false alarm probability for LSP, and peak prominence (as implemented in `SciPy`, Virtanen et al. 2020) for both GWPS and ACF. The remaining half of the test set are shown in the right column of Figure 2.4.

All three conventional methods struggle to recover periods longer than about 50 days. Longer than this, LSP and GWPS mistakenly recover signals approaching 30 days in period, which we suspect represents the TESS sector length of 27 days. LSP and GWPS are also susceptible to half-period aliases, which fall along the line $y = \frac{1}{2}x$. ACF is less susceptible to half-period aliases and appears to be the most successful method overall. However, the ACF and GWPS often misidentify signals at 5, 13, and 27 days (all well-known frequencies associated with TESS telescope systematics) as the rotation period. Interestingly, the ACF has small pockets of higher success at integer multiples of 27 days, beginning at 54 days. These occur when a star's rotation period coincides with an alias of the TESS sector length. Because the ACF is more likely to be detecting the systematic alias than the period, these coincidences should not be considered actual successes, suggesting that at long periods, the ACF's true recovery probability is lower than it appears to be.

In general, recovery was better for targets with higher light curve amplitude for all three methods, as one would expect. Filtering the sample based on periodogram peak significance marginally improved the recovery rates, but the predictions were still dominated by aliases at true periods longer than 50 days. The recovery rates also improved when limited to shorter periods (see Table 2.3). We have assumed no rotation-activity relation, so the improved recovery at shorter periods occurs when more rotations are observed in the given baseline, resulting in higher power in the periodograms. Moreover, at shorter periods rotation signals are less easily lost in the telescope systematics. In the unfiltered case, for example, if we limit to periods between 0 and 50 days, acc10 and acc20 improve to 45% and 61% for LSP, 43% and 56% for GWPS, and 42% and 54% for ACF. Filtering on periodogram peak significance and limiting to periods shorter than 50 days, acc10 and acc20 improve to roughly 60% and 80% respectively for all three techniques. We note that these short-period recovery rates are on par with those achieved by Aigrain et al. (2015) despite the differences in underlying period and amplitude distributions.

Even with filtering, conventional period-recovery techniques are subject to aliases, leaving much to be desired for long-period recovery in TESS. This is not surprising: LSP false alarm probability indicates how likely a power spectrum peak is to arise stochastically. It does not account for the systematics and aliases like those seen in TESS. Similarly, the peak prominence used for GWPS and ACF is simply a measurement of the peak height relative to neighboring troughs. It offers little insight into whether a peak arises from astrophysical periodicity, as peaks from strong aliases easily overpower those from astrophysical signals. This motivates the use of a CNN, which should be able to discern between aliases and rotation signals.

2.5.2 CNN performance on noiseless data

Our neural network's predictions on noiseless test data are shown in the left panel of Figure 2.5. The predicted periods have a mean absolute percentage error of 14% and a median absolute percentage error of 7%. 61% of periods were successfully recovered to within 10%, setting the bar for comparison to results for the noisy data.

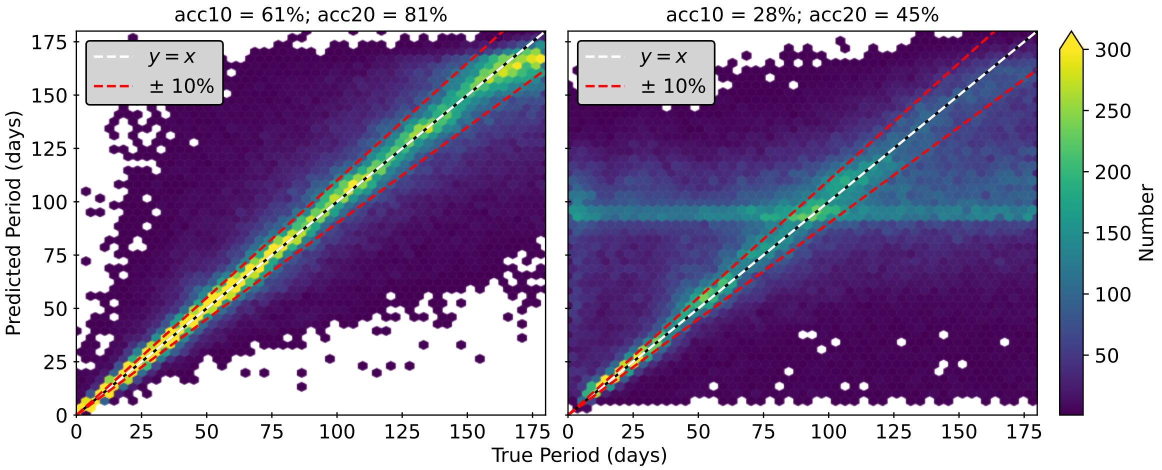

Figure 2.5: *Left:* Period predictions by our CNN trained on wavelet transforms of noiseless light curves. Predicted periods have mean absolute percentage error of 14%, median absolute percentage error of 7%, acc10 of 61%, and acc20 of 81%. *Right:* Period predictions from noisy data, where recovery is significantly worse. Predicted periods have mean absolute percentage error of 246%, median absolute percentage error of 24%, acc10 of 28%, and acc20 of 45%. The horizontal band at 90 days represents targets where the model struggled to predict the period. In these cases, the prediction was biased toward the distribution median, or 90 days.

2.5.3 CNN performance on noisy data

We present the neural network predictions on the noisy test data in the right panel of Figure 2.5. The predicted periods have a mean absolute percentage error of 246% and a median absolute percentage error of 24%. Only 28% of periods are successfully recovered to within 10%. The horizontal band at predicted period of 90 days represents simulated stars for which the network could not predict the period at all, instead assigning it the median of the period range. We discuss the filtering and removal of these spurious predictions later in this section.

The addition of TESS-like noise severely inhibits the performance of the neural network. Like the conventional methods, the neural network predictions are more accurate at shorter periods. When limiting to periods of 50 days or less, the median absolute percentage error is 12%, and 44% of targets are recovered to within 10%. The introduction of noise to the light curves also affects the amplitudes at which the network is most reliably predictive. The left panel of Figure 2.6 shows CNN recovery rate as a function of amplitude R_{per} (as defined by Basri et al. 2011) and equatorial rotation period. Here, "recovered" means the prediction is within 10% of the true period. As expected, the network performs better with higher-amplitude modulations, where the stellar signals are more easily picked out of the noise. For lower-amplitude modulations ($R_{\mathrm{per}} \lesssim 10^4$ ppm), the light curve noise dominates the stellar signal. At the lowest amplitudes, the recovery fraction approaches zero except for the range near 90 days where uncertain predictions are assigned the median of the period distribution. These low-amplitude light curves are analogous to light curves with no discernible spot modulation and provide an interesting look at how the CNN would handle light curves with no spots present. The predictions for these low-amplitude signals generally have large uncertainty as we expect.

There are a handful of bins in Figure 2.6 with seemingly high amplitudes but unsuccessful period predictions and large uncertainties. Most, if not all, of these high-amplitude failed recoveries are due to the noise template used. In these few cases ($< 1\%$ of galaxy light curves), the light curves all have one extremely noisy sector. This noisy sector dominates the wavelet transform, drowning out any rotation signal; it also dominates the amplitude measurement, masking the actual amplitude of the light curve. These noise templates will be removed from use in future work.

Also noteworthy is that the performance of the neural network worsens at both extremes of the period range. Period recovery worsens at periods longer than about 165 days, but also at periods shorter than 13 days where conventional period measuring methods succeed. As we discuss further in Section 2.6.1, this is due to the choice of loss function and its impact on predictions with uncertainty.

In addition to the rotation period, our choice of loss function allows us to predict the period uncertainty, which serves as a metric for how well the network is predicting the

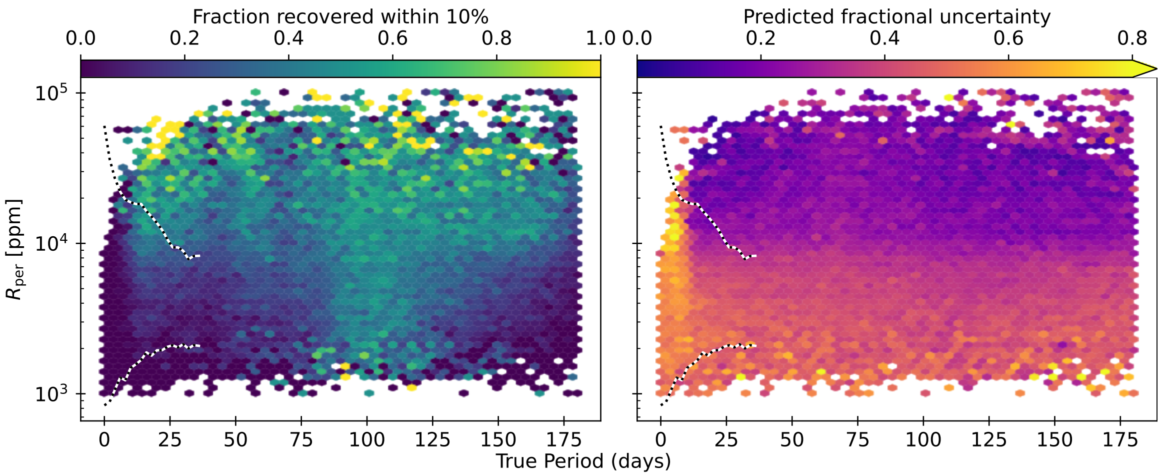

Figure 2.6: Neural network performance across the full simulation space of periods and amplitudes. In both panels, the dotted lines represent the 10th and 90th percentiles of the distributions from McQuillan et al. (2014), to gauge where stars from *Kepler* would fall. *Left:* Period recovery rate as a function of period and amplitude for the noisy data. The neural network performs better at higher amplitudes, where the rotation signal overpowers instrumental noise. The high-amplitude failed recoveries (i.e., the darkest blue bins with $R_{\rm per} > 30,000$ ppm) are from light curves whose galaxy noise templates had an extremely noisy sector. The noise dominated the light curve and wavelet transform, resulting in mismeasured amplitude and period. These noise templates will be removed in future work. *Right:* The same data, now colored by the neural-network-predicted fractional uncertainty in rotation period. The prediction is more certain for higher amplitudes. Furthermore, the prediction is most certain in the region with the highest recovery rate, indicating the predicted uncertainty is a reliable metric for period recovery without already knowing the true period.

period. The right panel of Figure 2.6 shows the predicted uncertainty versus period and amplitude. The predicted uncertainty, like the recovery rate, is better at higher amplitudes. Since the predicted uncertainty correlates with the recovery rate, the predicted uncertainty is a reliable metric for successful period recovery without already knowing the period. We can then use the predicted uncertainty to select a part of the sample recovered to a desired accuracy.

For our analysis, we selected the half of the test set with the lowest predicted fractional uncertainty. The median predicted uncertainty for the sample before the cut was $\sigma_{\rm pred}/P_{\rm pred} = 0.35$. The period recovery for the best-predicted half of the sample is

Table 2.3: Metrics of Period Recovery on Simulated Light Curves

		$P_{\mathrm{max}} = 180$ days				$P_{\mathrm{max}} = 50$ days			
Dataset	Method	MAPE (%)	mAPE (%)	acc10 (%)	acc20 (%)	MAPE (%)	mAPE (%)	acc10 (%)	acc20 (%)
A	LSP	160	11	48	66	150	7	64	83
	GWPS	52	8	56	76	52	6	67	85
	ACF	88	6	63	81	32	5	70	88
	CNN	14	7	61	81	11	5	69	86
B	LSP	93	64	18	25	146	12	45	61
	GWPS	69	73	15	21	59	14	43	56
	ACF	94	53	26	37	96	16	42	54
	CNN	246	24	28	45	149	12	44	64
C	LSP	63	54	21	29	54	8	56	73
	GWPS	50	51	25	34	27	6	63	80
	ACF	47	15	41	55	21	6	66	83
	CNN	57	11	46	69	11	7	63	86

Note. We show recovery metrics on the noiseless light curves without filtering by predicted uncertainty (set A), the noisy light curves without filtering (B), and the noisy light curves after filtering by predicted uncertainty (C). We also show metrics for both the full 0.1–180-day period set and for the subset with $P_{\mathrm{rot}} \leq 50$ days. All methods perform better on shorter-period stars, and filtering the period predictions by peak significance (or predicted uncertainty in the CNN case) improves recovery substantially for all methods. The CNN performs just as well as the conventional methods for periods less than 50 days. While for longer periods it appears the ACF outperforms the CNN, the ACF statistics are artificially inflated because nearly all the ACF's long period "successes" occur where the rotation period coincides with an alias from the TESS sector length (see Fig. 2.4). Thus, the CNN approach consistently outperforms the conventional techniques on simulated light curves with real TESS systematics.

shown in Figure 2.7. The cut removed 90% of the spurious 90-day period detections, and all summary statistics were improved. 46% of periods were correctly predicted to within 10%, and 69% were accurate to within 20%. The predicted periods had a mean absolute percentage error of 57% and a median absolute percentage error of 11%. A few targets with incorrectly predicted periods between 100 and 150 days remained after the cut. These had low predicted fractional uncertainty due to their large predicted periods, so they made

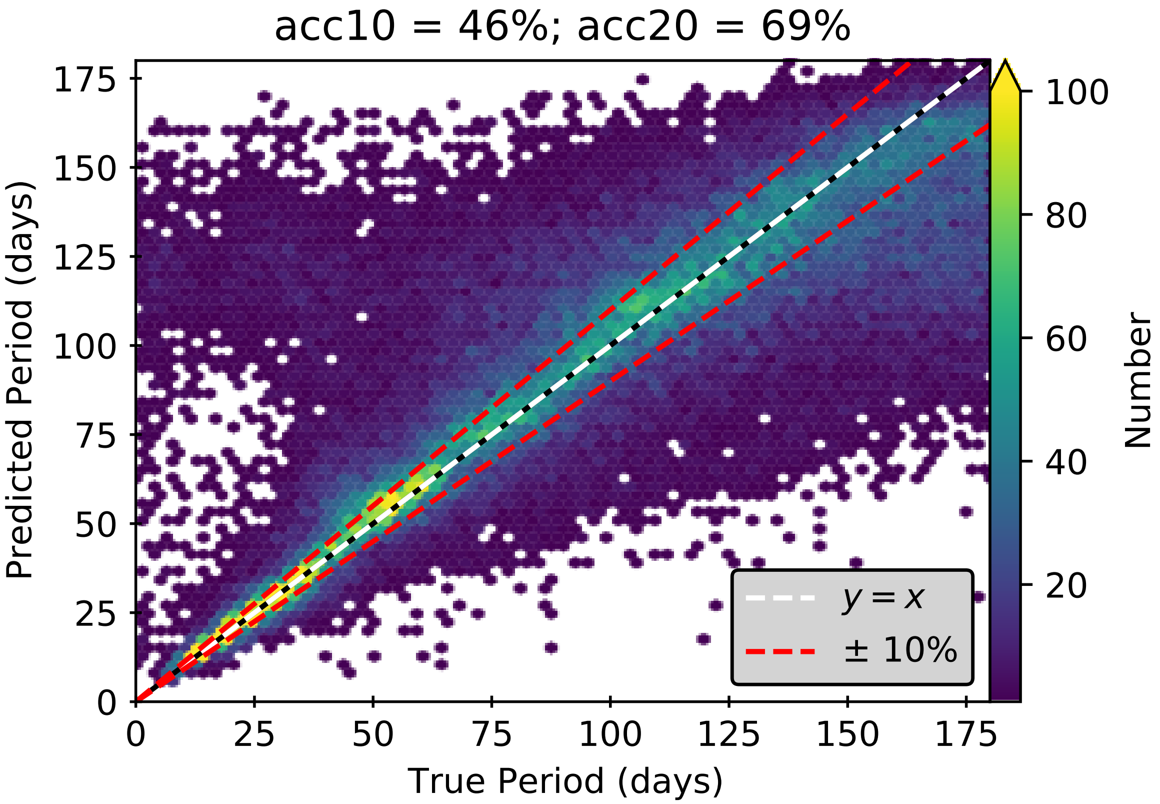

Figure 2.7: Period recovery for the half of the test set with the lowest predicted fractional uncertainty. Predicted periods have mean absolute percentage error of 57%, median absolute percentage error of 11%, acc10 of 46%, and acc20 of 69%. The predicted error cut removes the cluster of predicted periods at 90 days, giving credence to our cut to remove spurious period predictions. The cloud of objects with short true periods and predicted periods between 100 and 150 days have low fractional error because their predicted periods are large, but they account for only 4% of the objects remaining after the cut.

the cut despite being poorly predicted. They accounted for about 4% of the sample after the cut.

As with all other methods, the CNN performed better on the noisy data when limited to targets with periods less than 50 days. For this subset of the sample, the median predicted fractional uncertainty was $\sigma_{\mathrm{pred}}/P_{\mathrm{pred}} = 0.2$. Making the same cut as before (using the median fractional uncertainty of 0.2), the recovery of short-period stars improved to acc10 of 58% and median absolute percentage error of 8%. Table 2.3 shows the complete summary of our recovery results.

2.6 Discussion

We have demonstrated that CNNs are capable of extracting period information from noisy light curves or, more precisely, transformations of noisy light curves. Our model also predicts the uncertainty in the period estimate, enabling us to see where the network is most successful and determine which period predictions are most reliable. Here we discuss the strengths and weaknesses of our approach and compare them to those of conventional period detection methods. We then comment on the prospects of estimating rotation periods from real TESS light curves.

2.6.1 Strengths and weaknesses of the Deep Learning approach

We note that while `butterpy` includes the evolution of uniformly dark spots, it does not include bright plage or faculae, which are known to contribute significantly to the light curves of some active stars (Gondoin 2008). At this time `butterpy` also does not include non-uniformity of spot intensity, which is observed in sunspots (Hathaway 2015). While these are features we eventually wish to include in the `butterpy` models, the spot models in their current form should capture most of the variance seen in stellar rotational light curves. We do not believe the lack of these additional features significantly impacts our ability to recover rotation periods with Deep Learning.

Approximating non-uniform spots as uniformly dark circles may make subtle changes to the shape of the light curve, but the period information contained in the wavelet decomposition should be preserved. Similarly we expect plage and faculae to affect the light curve shape, but not the overall period information content of the wavelet transform, unless the bright spots perfectly cancel all dark spots on the stellar surface. This may actually occur in a small subset of stars (Reinhold et al. 2019), but for now we leave that investigation to future work.

Our CNN outperformed conventional techniques in the recovery of rotation periods from synthetic light curves. Whereas the conventional methods failed to recover periods longer than $\sim$2 TESS sectors, our method successfully recovered simulated star periods across the full simulation range of 0.1–180 days. Simulated stars in the range of periods yet unprobed by TESS—13.7 days up to 90 days and beyond—were recovered with the highest success rate. The recovery rate trails off at each end of the range ($P_{\rm rot} < 10$ days and $P_{\rm rot} > 170$ days) because of the choice of loss function: predicting the period with uncertainty biases predictions toward the median of the ensemble distribution and away from the ends of the range.

The challenge for classic period-recovery methods in TESS light curves is mostly due to sector-to-sector stitching and the presence of scattered Earth/Moon light (repeating every 27 and 13.7 days, respectively). Other effects such as temperature changes and momentum dumps appear at periods of 1.5, 2, 2.5, 3, 5, and 13.7 days (Vanderspek et al. 2018), all of which are clearly visible in Figure 2.4. All these effects combine to leave periodic imprints in the data that dominate stellar rotation signals and are difficult to remove. All three of our conventional method tests significantly misidentified 27-days as the rotation period. Different methods latch onto different signals as well. For example, ACF has significant misidentifications at 2.5 and 13.7 days and a weak twice-period alias, while WPS mistakes 1- and 5-day signals as the rotation period. LSP mistakes these high-frequency signals less often, but often falls prey to half-period aliases, as does WPS.

It is noteworthy that, unlike with LSP and WPS, our neural network has no significant misidentification of half-period aliases, double-dipper stars (Basri & Nguyen 2018), or high-frequency systematic aliases. This is especially encouraging since we use WPS as the basis for our training data. The fact that these aliases certainly exist in the training set but are not chosen as the period reveals the biggest strength of the CNN approach: neural networks can learn and bypass systematic and false-period signals to successfully regress rotation periods. Another strength of Deep Learning is the ability to pre-filter results using predicted uncertainties. If the rotation period is ambiguous, the network predicts a large uncertainty, allowing us to disregard the prediction. With the ability to regress long periods from TESS light curves in spite of systematics, we make a significant step towards large-scale stellar rotation studies with TESS.

2.6.2 Comparisons to other period recovery attempts

Our results are on par with or better than other recent attempts to estimate > 13-day rotation periods from TESS light curves. Canto Martins et al. (2020) used a combination of Fast Fourier Transform, Lomb-Scargle, and wavelet techniques to estimate periods for 1,000 TESS objects of interest. They obtained unambiguous rotation periods for 131 stars, but all were shorter than the 13.7-days TESS orbital period.

Lu et al. (2020) trained a random forest (RF) regressor to predict rotation periods from 27-day sections of *Kepler* light curves coupled with *Gaia* stellar parameters. They then evaluated the trained model on single sectors of TESS data for the same stars. Despite the stark differences in light curve systematics, they were able to recover rotation periods up to $\sim$50 days with 55% accuracy. Their accuracy is on par with the 57% overall mean error achieved by our Deep Learning model. However, when we limit our sample to simulated stars with periods less than 50 days, our mean error is significantly better at 11%. There are caveats to this comparison. First, the RF regressor relied primarily on the light curve variability amplitude and secondarily on effective temperature; light curve periodicity was not used for their period regression. Second, Lu et al. (2020) used two-minute cadence, Pre-search Data Conditioned Simple Aperture Photometry (PDCSAP) TESS light curves, while our light curves were thirty-minute cadence, and our processing pipeline was more similar to Simple Aperture Photometry (SAP). PDCSAP light curves are subjected to much heavier detrending than those produced by SAP methods. Finally, Lu et al. (2020) used real TESS data, while we used simulated light curves. Because the two sets comprise different underlying distributions of rotation period and amplitude, they likely have different recovery probabilities under the same method.

2.6.3 Prospects for measuring periodicity in TESS

We have so far demonstrated the ability to recover photometric rotation periods from simulated TESS-like stellar light curves using Deep Learning. But the biggest question remains: can we reliably measure long periods from real TESS data?

This is a difficult question to answer definitively for several reasons. First, validation of any method requires a set of real stars for which rotation periods are already known. The ideal data set for comparison is *Kepler*, where tens of thousands of periods have been recorded (McQuillan et al. 2014; Santos et al. 2019). Unfortunately, the overlap between TESS and *Kepler* is small: most *Kepler* stars were observed for only a single sector at a time in TESS. With only a 27-day baseline, it is impossible to validate a method of obtaining long periods. Stars in the TESS CVZs were monitored continuously for almost a year, but only a handful of these stars have previously known rotation periods.

Despite the limitations, we attempted to recover rotation periods for a handful of stars observed by *Kepler*, the Kilodegree Extremely Little Telescope survey (KELT, Pepper et al. 2007), the MEarth Project (Berta et al. 2012), and the All-Sky Automated Survey for Supernovae (ASAS-SN Shappee et al. 2014; Kochanek et al. 2017).

Kepler

We targeted about 1,000 stars in the *Kepler* field that had prior rotation period measurements from (McQuillan et al. 2014) as well as two consecutive sectors in TESS, offering a baseline of roughly 50 days. We simulated an entirely new training set with periods spanning 0.1 to 50 days, using a sample of galaxies in the *Kepler* field as the noise model. With a 50-day baseline, only periods of up to 25 days might be recoverable, as timescales longer than this may be dominated by edge effects in the wavelet transform. Our CNN was unable to recover *Kepler* periods reliably. Even when filtering based on predicted uncertainty, the recovery was no better than a random draw from the period distribution. This suggests the CNN/wavelet approach is strongest when multiple (i.e., more than 2) contiguous sectors of data are available.

KELT

We similarly targeted 106 stars in the TESS SCVZ also observed by the KELT survey. Oelkers et al. (2018) obtained rotation periods for these stars using Lomb-Scargle periodograms of their KELT light curves. We specifically selected stars with a measured period greater than 13.7 days to test recovery of long periods. To maximize the chances of recovering rotation periods, we used the TESS Science Processing Operations Center (SPOC) FFI simple aperture photometry (SAP) light curves (Caldwell et al. 2020). At the time of writing, only sectors 1-6 were available, but we trained our CNN using year-long (13-sector) light curves. However, the construction of our wavelet power spectrum used the same vertical (frequency) axis regardless of light curve length, so any length of light curve could be used without needing to retrain the neural network.

Upon visual inspection of the TESS-SPOC light curves, we noticed that many did not show obvious rotational modulation. Selecting only those light curves with unambiguous rotational modulation, we were left with 26 light curves with KELT rotation periods spanning 13.7 to 47 days. While visually inspecting the light curves, we also ensured the apparent rotational modulation was consistent with the periods obtained by Oelkers et al.

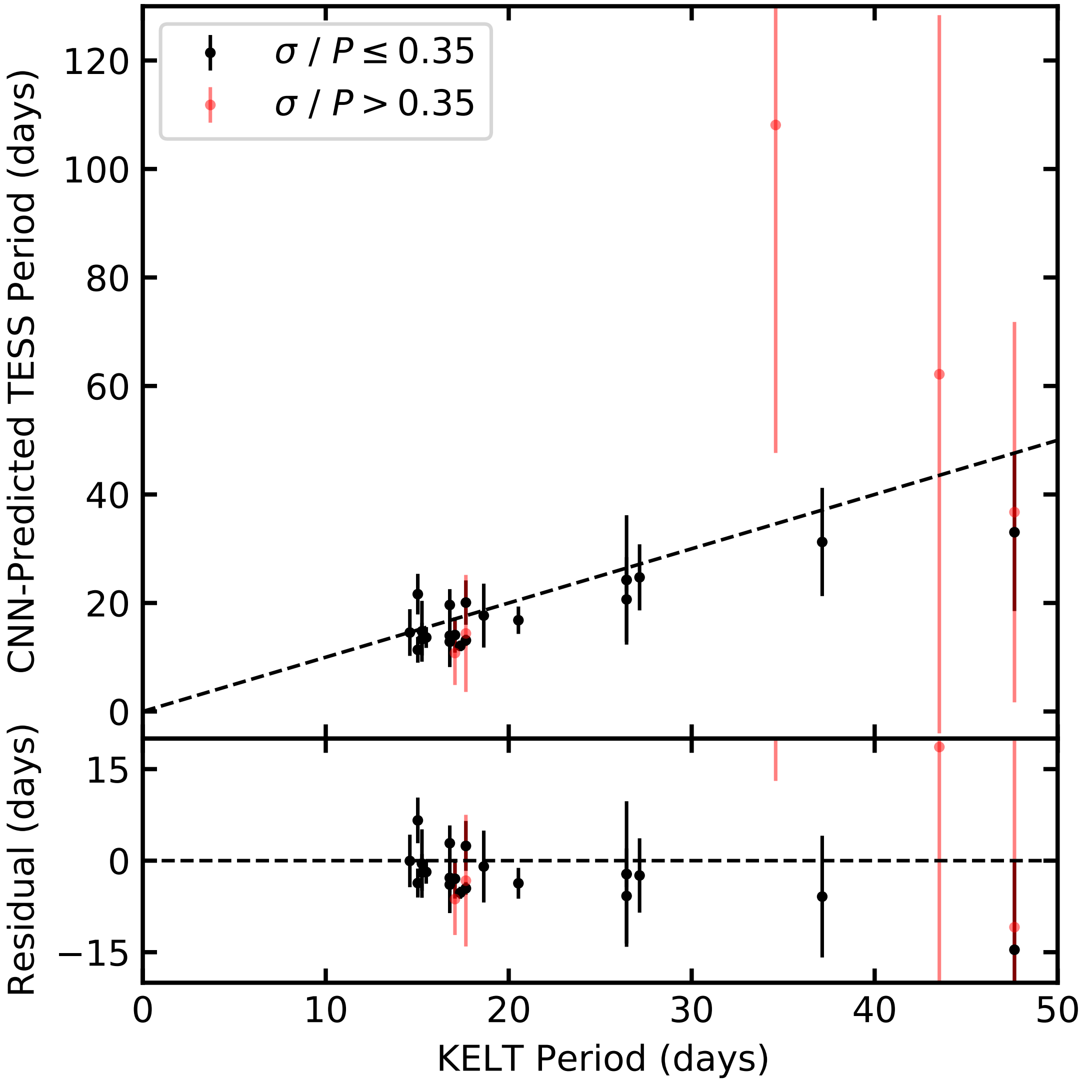

Figure 2.8: Period recovery of stars in both TESS and KELT for which rotational modulation is apparent in the light curve. We applied the same fractional uncertainty cut applied to the simulation recovery results; the 21 stars that made the cut are in black, while the 5 stars with unreliable period predictions are in red. We successfully recovered periods longer than 13.7 and even 27 days from real TESS light curves. Even when TESS aliases are the dominant sources of power in the wavelet transform, our neural network was able to recover the correct rotation period.

(2018). We generated wavelet power spectra and evaluated our neural network on the light curves. Figure 2.8 shows our predictions for these 26 KELT stars.

It is interesting that the rotation periods tend to clump around 17, 27, 37, and 47 days. These periods are not associated with any of the known KELT aliases discussed by Oelkers et al. (2018), and besides 27 days, they are not associated with any TESS aliases. Furthermore, given that 17, 37, and 47 are prime, they are unlikely to be associated with a single common alias. These are more likely associated with the spacing of periods searched by Oelkers et al. (2018). Their overall period distribution seems to have more stars at these periods than at other values, so the clumping likely arises either from sensitivity of their method to those particular periods, or from the spacing of periods used in their search for rotation.

After running these KELT stars through our CNN, we subjected the predictions to the same cut in predicted fractional uncertainty as in Figure 2.7. Stars that made the cut are displayed in black, while stars whose predicted uncertainties were too large are shown in red. The KELT stars for which we detected periods range from 0.2% to 2% in variability amplitude. We successfully recovered stars with rotation periods longer than 13.7 and 27 days, even when TESS systematics were the dominant source of power in the wavelet power spectra. Furthermore, using the predicted fractional uncertainty as a quality cut successfully removed stars whose predictions were unreliable or wrong while ensuring the most reliable predictions remained in the sample.

MEarth and TOI-700

Only one long-period target was observed by MEarth in the TESS SCVZ: TIC 149423103. Newton et al. (2018) measured a rotation period of 111 days for this target from MEarth data. Using our neural network on the FFI data from TESS, we obtained $P_{\rm rot} = 116 \pm 48$ days. While the predicted period was within 5% of the “true” period, the relatively large uncertainty (41%) means this target would fail our quality cut, and an ensemble period recovery attempt would miss it.

TOI-700 is another well-characterized star in the SCVZ. Using ASAS-SN data, Gilbert et al. (2020) estimated a precise rotation period of 54.0±0.8 days. Hedges et al. (2020) used a systematics-insensitive periodogram of its TESS light curve to obtain a period of 52.8 days. With our model we predicted a period of 59±53 days. Our period prediction was accurate to within 10%, but the large uncertainty would cause this target to be missed as well.

General period recovery and improvements

While we successfully recovered the rotation periods of these few hand-picked stars, robust recovery on larger, statistical scales will require more work and vetting. Our method allows us to see beyond the 13.7-day barrier, but mostly stars with large amplitudes were reliably recovered: the detection fraction in the synthesized test set picks up around 1% amplitude, and the successfully recovered KELT stars range from 0.2% to 2% in amplitude. We are still limited by the TESS noise floor. TESS is less precise than *Kepler* at all magnitudes (Vanderspek et al. 2018), so spot modulations require higher amplitudes to rise above the noise. Both panels of Figure 2.6 show the 10th- and 90th-percentile variability amplitudes of the rotating stars from McQuillan et al. (2014). The bulk of *Kepler*'s rotating population fall between R_{per} of 1 and 20 parts per thousand and lie in a region where our recovery was less successful. In addition, slowly rotating stars are typically old and therefore less active than their young, rapidly spinning counterparts. The difficulty of recovering periods at smaller amplitudes will adversely affect our ability to detect these slow rotators. These kinds of stars will be more difficult to recover with TESS, whatever the method. However, another view suggests recovery of real stars may not be so farfetched. Figure 2.9 shows the period recovery rate for the synthesized test set as a function of R_{per}, the light curve

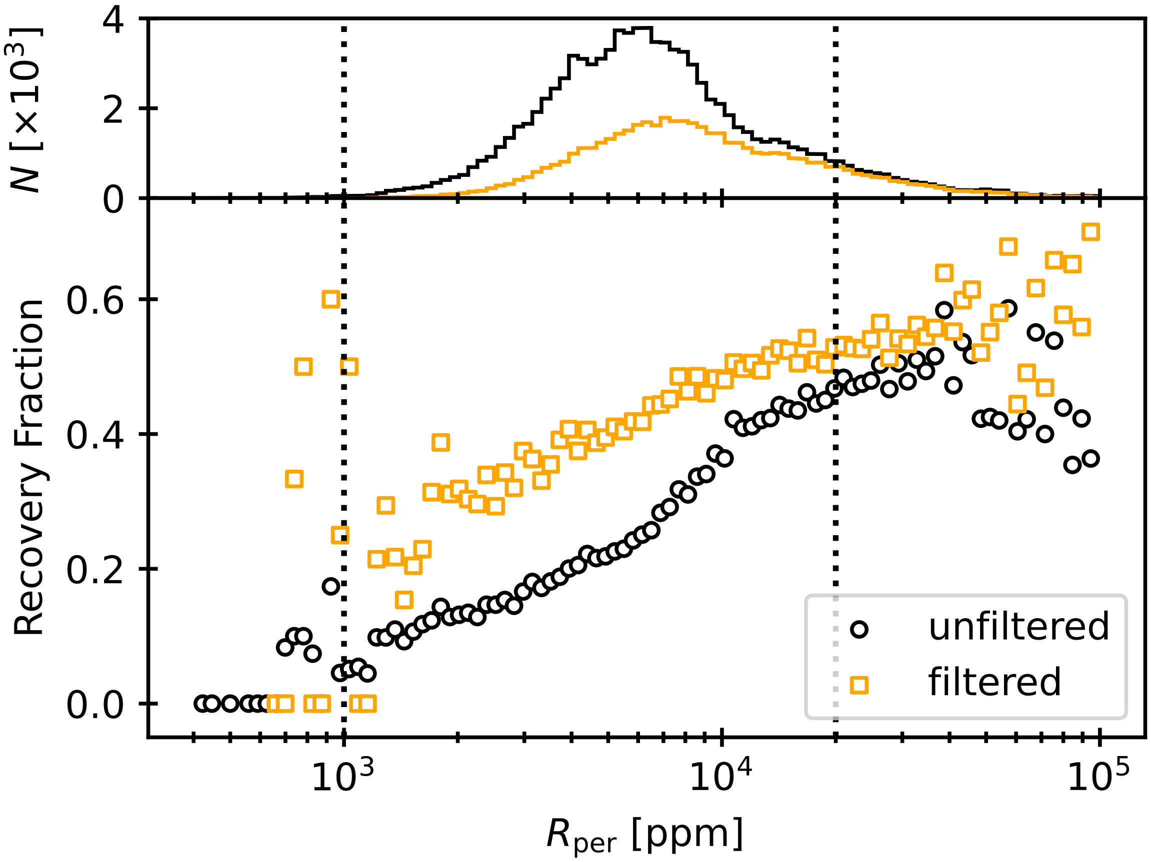

Figure 2.9: *Top*: Histogram of amplitudes of synthesized light curves in our test set, both before filtering (black) and after (orange). *Bottom*: Recovery rate as a function of amplitude for both the unfiltered (black circles) and filtered (orange squares) period predictions on the synthesized test set. The vertical dotted lines show the approximate range of amplitudes seen by McQuillan et al. (2014), where "real stars" might lie. According to the basic picture of period-amplitude relationships, slowly rotating stars will be toward the left, and fast stars will be toward the right. Applying our neural network to real stars, we expect to detect fewer low-amplitude (slowly rotating) stars than high-amplitude (fast rotating) stars, but filtering on predicted uncertainty somewhat mitigates the disparity. The large scatter in recovery fraction of the filtered data at $R_{\text{per}} \sim 10^3$ ppm is due to the very small number of objects in these bins. In this range, the unfiltered data bins have an order of magnitude more objects than the filtered data bins (hundreds in the unfiltered vs. tens in the filtered).

modulation amplitude. It is essentially the left panel of Figure 2.6 collapsed onto the vertical axis. The vertical dotted lines show the range of amplitudes for the *Kepler* stars of McQuillan et al. (2014). While the recovery is worse at lower amplitudes, filtering by predicted uncertainty improves the recovery rate at all amplitudes and somewhat lessens the disparity between high and low amplitudes. Without improvements to our method, given a log-uniform distribution of amplitudes in the range seen in *Kepler*, we expect to recover low-amplitude stars about half as frequently as high-amplitude stars.

Still, we believe improvements to our method will maximize what is recoverable from TESS. There are several ways to extend the predictability of our neural network to lower amplitudes and enhance the predictability at high amplitudes. The first and perhaps most useful improvement will come through light curve processing. Our processing pipeline followed the regression corrector documentation of Lightkurve Collaboration (2020) using a magnitude-dependent aperture threshold. In practice, a more carefully developed pipeline should be preferred. At the time of writing, the FFIs of sectors 1–6 have been reduced by both the TESS Asteroseismic Science Operations Center (TASOC) pipeline and the TESS Science Processing Operations Center (SPOC) pipeline. Once sectors 7-13 are processed, the Southern Continuous Viewing Zone (SCVZ) will be complete, providing year-long light curves for hundreds of thousands of targets. These light curves will feature more careful systematics removal and should contain cleaner examples to use as ”pure noise” light curves in our sample. We leave the use of these light curves to future work.

Another improvement may come with the inclusion of observation metadata. In TESS data, certain systematic effects are specific to particular cameras, CCDs, or even locations on a CCD. We could include camera number, CCD number, and x- and y- pixel coordinates in the training data set, perhaps as extra input nodes to be included alongside the input wavelet transforms. This will allow neural networks to learn where to expect certain features and more easily ignore them in favor of astrophysical signals.

In this work we have assumed no period-amplitude relationship in our simulated training set. This was to avoid imprinting strong priors on the predictions of the neural network. In future efforts, we may see improvements from incorporating period-activity relations in the underlying training set. These might serve to enhance the reliability of predictions, as amplitudes may help inform the network of whether a star is rotating slowly or quickly. We might also see improvements in training efficiency as the network learns more rapidly what short-period and long-period wavelet transforms look like.

Improvements can be made to the neural network as well. In its current form, our model assumes that all input signals have rotation signatures, but not all real light curves display rotational modulation. In the future we may include a classification step like Lu et al. (2020) to determine which signals contain rotational modulation. Adding this classification step will allow the regressor to focus on signals with recoverable rotation, making for more efficient training.

Based on recovery from the simulated test set, our approach is currently most effective above periods of about 13 days due to the loss function's tendency to bias uncertain predictions toward the ensemble mean. While experimenting with other loss functions may result in improved short-period recovery, preliminary tests using training sets with smaller period ranges have shown promise as well. One might consider using two neural network regressors—one for short periods, and one for long periods—and a preceding classification step to decide which regressor to use. We leave this investigation to future work.

It is important to note that our implementations of conventional period recovery techniques perform better on our simulated test set than the best efforts on real light curves (e.g., Canto Martins et al. 2020; Avallone et al. 2022, who were unsuccessful in recovering anything past 13.7 days). This indicates that, despite all our attempts to create as realistic a training set as possible, our simulations are not perfectly representative of real stars. It could be that our stitching routine fails to suppress long-period signals as the real light curves do. Another possibility is that our spot model, while tuned to the Sun, may not be representative of real spots on other stars. Whatever the reason, we have demonstrated the ability to recover periods even when the systematics that *are* present in our simulations make conventional techniques fail.

Even though our spot evolution simulations include latitudinal differential rotation, we were unable to recover differential rotation in this study. In some wavelet power spectra of our simulated light curves, the differential rotation is apparent as a slope in the frequency of maximum power versus time. When binning the power spectra to 64×64 pixels, the slope is more difficult to resolve. While increasing the resolution of the wavelet power spectrum images should enable the recovery of differential rotation, it will come at the expense of longer training time. We will investigate the recovery of differential rotation, activity levels, and spot properties in future work.

If we can see beyond the complicated systematics, TESS will deliver the largest set of rotation periods yet. McQuillan et al. (2014) obtained rotation periods for 34,000 stars in the *Kepler* field. The TESS continuous viewing zones combine to cover 900 square degrees around the ecliptic poles, representing about eight times the sky coverage of *Kepler* during its primary mission. We can therefore expect hundreds of thousands of new stars with rotation period estimates from the TESS CVZs, and perhaps more from lower ecliptic latitudes. Because of TESS's lower precision compared to *Kepler*, the true number will likely be somewhat smaller, but the prospect of hundreds of thousands of new periods is worth continued refinements of this technique. We leave the application of this tool to the full CVZ samples to future work.

2.7 Summary and Conclusion

We used a Convolutional Neural Network to recover rotation periods and uncertainties from simulated light curves with real TESS systematics. Despite the systematics, we successfully recovered periods even for targets whose periods were longer than the 13.7-

day barrier encountered by conventional period recovery methods. In the half of the simulated test data with the smallest predicted fractional uncertainty, we recovered 10%-accurate periods for 46% of the sample, and 20%-accurate periods for 69% of the sample. We also found no significant misidentification of half-period aliases, unlike the Lomb-Scargle and wavelet methods. While periods were retrieved more successfully from higher-amplitude signals, the ability to predict uncertainties allows us to probe lower-amplitude rotation signals as well.

We plan to use this method to produce a catalog of rotation periods from TESS full-frame image light curves. We will also add output options to our neural network to predict latitudinal differential rotation and understand more of the properties used to produce the training set. With Deep Learning, we hope to maximize the output of TESS in spite of the frustrations that arise from its systematics. The ability to recover rotation periods, especially long periods, from TESS data will finally enable large studies of rotation across diverse populations of stars in the Galaxy if only the systematics can be learned.

Chapter 3

The Grid-Based Stellar Modeling Framework and Gyrochronology

Originally published as Chemical Evolution in the Milky Way: Rotation-based ages for APOGEE-*Kepler* cool dwarf stars*, ApJ 888, 43, by Claytor et al. (2020)*

3.1 Background

Our understanding of Milky Way formation and evolution is informed by kinematics and chemistry of different stellar populations. Studies of galactic archaeology (e.g., Edvardsson et al. 1993; Feltzing & Gustafsson 1998; Bensby et al. 2003; Haywood et al. 2013; Bensby et al. 2014; Feltzing et al. 2017) have constructed the current schematic of our galaxy's disk: an old, "thick" disk poor in metals but enhanced in α-process elements; and a young, metal-rich, α-poor "thin" disk. Kinematically, the thick disk is characterized by high velocity dispersion perpendicular to the galactic plane, while thin-disk stars remain near the plane. Trends of composition with age suggest these populations underwent separate phases of chemical enrichment, thought to be driven by different kinds of supernovae (Maoz et al. 2011). These trends have even led some to suggest certain abundances as proxies for age (e.g., Bensby et al. 2014; Martig et al. 2016; Tucci Maia et al. 2016; Feltzing et al. 2017). Other studies have argued against the thin- and thick-disk model of the Milky Way: as our ability to estimate precise stellar ages, composition, and kinematics has improved, the historical two-population hypothesis has evolved into a continuum of galactochemical structure and evolution (e.g., Bovy et al. 2012a,b; Buder et al. 2019).

The study of chemical evolution in stellar populations is impossible without precise ages. To date, most investigations have used isochrones to estimate ages (Nordström et al. 2004; Haywood et al. 2013; Buder et al. 2019). While easy to implement, isochrone ages are most useful for cluster stars, which provide an ensemble of stars at a single age, or for field stars that have aged to about one-third of their main-sequence lifetimes (Pont & Eyer 2004; Soderblom 2010) and thus move substantially on the Hertzsprung-Russell (H-R) diagram. In this regime, isochrone ages are, at best, precise to 15% (e.g., Nordström et al. 2004). However, this excludes the majority of stars, which are not massive enough to have evolved sufficiently within the age of the galaxy. For the lowest-mass stars, which are practically stationary in temperature–luminosity space, isochrones provide no age constraints whatsoever (Pont & Eyer 2004; Epstein & Pinsonneault 2014).

Asteroseismology can also provide valuable constraints on global stellar properties. Virtually all cool stars excite solar-like oscillations, with timescales ranging from minutes to months depending on the mean density of the star. These oscillation frequencies can be measured successfully for large samples of stars using time-domain space data (e.g., Stello et al. 2013; Hon et al. 2019; Schofield et al. 2019). The frequency of maximum power is related to the surface gravity (Kjeldsen & Bedding 1995), and the frequency spacing between modes is related to the mean density via asymptotic pulsation theory. This information can be combined to infer mass and radius for large samples of stars. For red giants, knowledge of mass and composition alone gives valuable age information (e.g., Silva Aguirre et al. 2018); mass information also allows more precise ages for solar analogs than one can obtain from H-R diagram position alone. By analyzing the frequency pattern in detail, one can also obtain more direct age constraints tied to helium production in the core, giving fractional age uncertainties as low as 5% in the best cases (Creevey et al. 2017). Again, however, for the lower main sequence these asteroseismic signals become ineffective chronometers because age evolution at fixed mass produces small changes in either central helium abundance or radius. Furthermore, asteroseismic signals become difficult to detect in stars below solar mass. Studies of galactic dwarfs require a more uniformly accessible chronometer.

With the advent of large time-domain photometric surveys, increasingly large samples of stellar rotation periods have become available (e.g., McQuillan et al. 2014, who detected periods in over 80% of late-K and early M-stars in the *Kepler* field). These period estimates are natural byproducts of transit and transient surveys and enable the inference of ages using gyrochronology (Barnes 2003, 2007), based on the observation that main-sequence stars spin down as they age (e.g., Skumanich 1972). Barnes (2007) argued that with proper calibration, gyrochronology could be used to infer stellar ages to within 15%, requiring knowledge only of the color (a proxy for mass) and rotation period. This promise has driven several investigations of rotation–age relationships, typically focused on cool, main-sequence stars (e.g., Barnes 2007; Mamajek & Hillenbrand 2008; Barnes & Kim 2010; Epstein & Pinsonneault 2014; Angus et al. 2015; Gallet & Bouvier 2015; Meibom et al. 2015; van Saders et al. 2016).

Using the spin-down law of Krishnamurthi et al. (1997), Epstein & Pinsonneault (2014) explored the strengths and weaknesses of rotation-based methods, concluding that gyrochronology may be a more precise clock than both asteroseismology and isochronal techniques for cool main-sequence stars. It has potential for Sun-like stars as well: Meibom et al. (2015) obtained rotation periods for stars in NGC 6819, a 2.5 Gyr-old cluster, and demonstrated that gyrochronology could be used to obtain $\sim 10\%$ ages for solar-temperature stars.

Gyrochronology comes with challenges as well. Purely empirical methods are restricted to the domain in which they are directly calibrated, which can severely limit their utility. Rotational properties are strong functions of mass and evolutionary state, making extrapolation to regimes with poorly-characterized period-mass-age relationships risky. Theoretical models can, in principle, allow more robust predictions for stars not directly constrained by data. However, the underlying physical model can be complex. We outline the strengths and weaknesses of these different approaches below.

Empirical approaches can be powerful and flexible, using a methodology similar to that employed by color-temperature relationships: one takes calibrators of known age and correlates observables, such as color and rotation period, with age. Calibration sources tend to be open clusters (modern *Kepler*-era calibrators: Meibom et al. 2011; Barnes et al. 2016; Hartman et al. 2009; Agüeros et al. 2018; Rebull et al. 2016, 2017; Douglas et al. 2016), asteroseismic stars (García et al. 2014a; Angus et al. 2015; van Saders et al. 2016), or binaries for which individual periods are known (Mamajek & Hillenbrand 2008; Chanamé & Ramírez 2012). These come with important systematics. For example, old clusters are generally more distant than young ones. As a result, calibration samples for old, lower-main-sequence stars are sparse due to the challenges of observing those distant clusters. Amplitudes of variation are smaller for hot stars and slow rotators, so rotational detection is biased against older and more massive stars as well. There are also few calibrators of non-solar metallicity. Consequently, the composition dependence of stellar spin-down remains poorly constrained, and the behavior at older ages is subject to severe observational selection effects. More generally, structural evolution (through angular momentum conservation) can induce large departures from simple power-law behavior (see van Saders & Pinsonneault 2013, for a discussion on subgiant rotation).

Theoretical gyrochronology models require choices for the torque associated with magnetized winds, angular momentum transport, and initial rotation conditions. While braking laws (e.g., Kawaler 1988; Krishnamurthi et al. 1997; Matt & Pudritz 2008; Matt et al. 2012; van Saders & Pinsonneault 2013) are physically and empirically motivated, they require some assumptions regarding magnetic field strength, geometry, and stellar mass loss. Many spin-down relations treat stars as solid bodies. While this assumption is reasonable for old Sun-like stars, both theoretical (Gallet & Bouvier 2015; Denissenkov et al. 2010) and observational (Curtis et al. 2019; Agüeros et al. 2018) investigations suggest that the neglect of internal angular momentum transport is a poor assumption in very young objects. Furthermore, a single set of initial conditions is often chosen to represent all stars, but the period distributions of young cluster members demonstrate both striking mass-dependent trends and a wide range of initial rotation rates at fixed mass (Hartman et al. 2009; Rebull et al. 2016). While the braking laws predict that these initial conditions matter less for older stars (van Saders & Pinsonneault 2013; Epstein & Pinsonneault 2014), there are combinations of stellar masses and ages for which this initial scatter should not be ignored.

There is also evidence that the underlying model can break down for inactive stars. van Saders et al. (2016) found that stars more than halfway through their main-sequence lifetimes experience weakened braking (see also Angus et al. 2015). This poses extra constraints on the types of stars that can safely be considered in gyrochronological studies.

Stars less massive than the Sun have longer main-sequence lifetimes and thus take longer to reach the main-sequence halfway point. The coolest K- and M-dwarfs cannot have reached this point within the age of the galactic disk, so weakened braking should not pose a problem for the lowest-mass stars. In this work we focus on these low-mass stars, for which we believe gyrochronology has the greatest potential. We adopt a forward modeling approach, taking advantage of the ability of theoretical models to account for the effects of composition on angular momentum evolution predictions. We obtain rotation-based ages for a sample of cool dwarf stars observed by both *Kepler* and the Apache Point Observatory Galactic Evolution Experiment (APOGEE, Zasowski et al. 2013; Majewski et al. 2017). Using our derived ages, we explore the evolution of α-element abundances in the Milky Way and attempt to recover chemical evolution trends seen in the literature. We investigate the biases inherent to the detection of rotation periods and consequently to age inference. Finally, we examine the sensitivity of our age estimates to assumptions of metallicity, α-abundance, and initial rotation conditions, demonstrating the viability of gyrochronology as a tool for astrophysical problems.

3.2 Methods

The use of model-based gyrochronology requires several assumptions. First are choices of the actual input physics of stellar evolution, including chemical evolution and the treatment of convection. Invoking rotation forces a choice of internal angular momentum transport, braking law, and initial conditions. While our model-driven approach employs physically motivated choices for all these, each choice still requires empirical calibration based either on the Sun alone or on a small sample of well-studied stars. We explore these choices in detail below. Because of the assumptions built into our method, readers should note that 1) our results are unavoidably model-dependent, and that 2) making different model choices will affect the absolute ages, but the ranked order should be preserved. Understanding the order of galactic formation requires accurate relative ages, but accuracy in absolute age is not as necessary.

3.2.1 Stellar Spin-Down

Current theory of stellar spin-down or braking uses charged stellar winds in a magnetic field to carry angular momentum away from the star. The most basic braking laws have the form $dJ/dt \propto \omega^3$ (Kawaler 1988) for stars of a given mass, where J is the angular momentum, and ω is the angular rotation velocity. In other words, faster-rotating stars spin down more quickly, while more slowly-rotating stars spin down more slowly. This means that stars with similar masses born at nearly the same time will asymptotically approach the same spin rate, regardless of their initial angular speeds. Thus we can map the rotation period of a star at late time robustly to its age, provided the mapping is properly calibrated. This relationship is valid for stars with $M \lesssim 1.3 M_\odot$ or $T_{\rm eff} \lesssim 6200$ K. Above these regimes the surface convection zone vanishes, affecting the magnetic field generation and thereby the spin-down process (this is known as the Kraft break, after Kraft 1967).

Describing the period distributions observed in clusters requires more complicated braking prescriptions than the Kawaler law. The discovery of rapidly-rotating stars in the Pleiades cluster (Soderblom et al. 1983; Stauffer et al. 1984) suggested that angular momentum loss must be weaker in some regimes. Observations of x-ray emission, a proxy for magnetic activity, also suggested that stars' magnetic fields saturate above some critical rotation speed $\omega_{\rm crit}$ (e.g., Vilhu & Rucinski 1983; Wright et al. 2011). This saturation would allow for weaker magnetic braking for the fastest-rotating stars. Using magnetic saturation to modify the Kawaler law, Krishnamurthi et al. (1997) and Sills et al. (2000) were able to reproduce the period distributions in open clusters. This modified braking law has the form

$$\frac{dJ}{dt} = \begin{cases} -K\omega_{\rm crit}^2 \omega \left(\dfrac{R}{R_\odot}\right)^{\frac{1}{2}} \left(\dfrac{M}{M_\odot}\right)^{-\frac{1}{2}}, \ \omega > \omega_{\rm crit} \\ -K\omega^3 \left(\dfrac{R}{R_\odot}\right)^{\frac{1}{2}} \left(\dfrac{M}{M_\odot}\right)^{-\frac{1}{2}}, \ \omega \leq \omega_{\rm crit} \end{cases}$$

where

$$\omega_{\mathrm{crit}} = \omega_{\mathrm{crit},\odot} \frac{\tau_{\mathrm{cz}}}{\tau_{\mathrm{cz},\odot}},$$

τ_{cz} is the convective overturn timescale, and K is a constant calibrated so that the law reproduces the Sun's rotation at the solar age. R and M are the stellar radius and mass, respectively, and the subscript $\odot$ denotes solar values.

This form of the braking law ties the magnetic braking to the properties of the convection zone (e.g., Wright et al. 2011; Cranmer & Saar 2011), introducing an additional mass dependence. However, to second order, metallicity also affects the properties of the convection zone: metallicity increases opacity, which increases the depth of the surface convection zone and convective overturn timescale. Furthermore, metal content impacts the main-sequence lifetimes of stars at fixed mass, meaning that stars of different metallicities have different amounts of time over which to lose angular momentum on the main sequence. Two stars with the same mass and age, but different compositions, will therefore have different rotation periods.

Empirical braking laws generally neglect metallicity because there are too few calibrators to span that dimension sufficiently. Most open clusters used to calibrate spin-down relations have solar metallicity, so using these relations to predict angular momentum loss for stars with non-solar abundances requires extrapolation. However, with a full evolutionary model, one can account for the impact of metallicity on stellar structure and lifetime naturally and then apply a braking law to the model. This will result in a metallicity-dependent spin-down relation, and while there is still a lack of calibrators beyond solar metallicity, the extrapolation to other metallicities is physically motivated.

Using the braking law in Matt & Pudritz (2008) and Matt et al. (2012), van Saders & Pinsonneault (2013) produced such a model-based spin-down relation. They presented a torque of the form

$$\frac{dJ}{dt} = \begin{cases} f_K K_M \omega \left(\frac{\omega_{\rm crit}}{\omega_\odot}\right)^2, \ \omega_{\rm crit} \leq \omega \frac{\tau_{\rm cz}}{\tau_{\rm cz,\odot}} \\ f_K K_M \omega \left(\frac{\omega \tau_{\rm cz}}{\omega_\odot \tau_{\rm cz,\odot}}\right)^2, \ \omega_{\rm crit} > \omega \frac{\tau_{\rm cz}}{\tau_{\rm cz,\odot}}, \end{cases} \tag{3.1}$$

with

$$\frac{K_M}{K_{M,\odot}} = R^{3.1} M^{-0.22} L^{0.56} P_{\rm phot}^{0.44}.$$

Here f_K is the solar calibration constant, and R, M, L, and $P_{\rm phot}$ are the radius, mass, luminosity, and photospheric pressure, respectively, in solar units. To summarize, van Saders & Pinsonneault (2013) took the Matt & Pudritz (2008) formulation, which uses the magnetic field strength and mass loss rate, and parameterized them in terms of photospheric pressure, rotation velocity, and convective overturn timescale based on empirical relations (Hartman et al. 2009; Wood et al. 2005; Pizzolato et al. 2003). Notice that, for a star of known mass, composition, and age, the other parameters in K_M can be determined from a stellar model, allowing for extrapolation of the spin-down law to stars with non-solar composition. While this partially accounts for metallicity in the braking law, the exponents of the braking law parameters are anchored in empirical calibrations which are largely based on stars with Sun-like composition. We do not treat the composition dependence of these exponents, nor any metallicity dependence of the initial conditions, both of which may be important. Instead, we focus only on the underlying stellar evolution models. The remaining values of f_K and $\omega_{\rm crit}$, as well as initial conditions (i.e., initial disk period and disk-locking timescale) are typically calibrated using solar and cluster data (van Saders & Pinsonneault 2013).

The braking law in Eq. (3.1) has been tested in several regimes against other spin-down models. For example, van Saders & Pinsonneault (2013) showed that this law reproduces the rapid rotation of stars near the low-mass side of the Kraft break better than other

Table 3.1: YREC Model Grid Points

	min	max	step
mass ($M_\odot$)	0.3	2.0	0.01
[M/H] (dex)	-1.0	0.5	0.5
[α/M] (dex)	0.0	0.4	0.4

Kawaler law variants. Similarly, Tayar & Pinsonneault (2018) demonstrated the strength of Eq. (3.1) in reproducing the rotation periods of intermediate-mass core-helium-burning stars. For stars more like the Sun, most braking laws perform equally well since they are all anchored to the same set of Sun-like calibration stars. Because of its track record in reproducing observed periods of stars of various masses and evolutionary stages, we adopt the braking law in Eq. (3.1) for our study.

For our analysis we make use of the grid of stellar rotation models created using the Yale Rotating stellar Evolution Code (YREC, Demarque et al. 2008) from van Saders & Pinsonneault (2013) and van Saders et al. (2016). These models do not intrinsically include rotation. Instead, rotational evolution is determined by integrating Eq. (3.1), while the models are used to provide the time and metallicity dependence of the stellar parameters appearing in the braking law. Thus, our rotational evolution does not include the effects of rotational mixing nor evolutionary feedback from starspots, both of which may be important for the most active and rapidly rotating stars. We used the same input physics as van Saders et al. (2016), but recomputed the model grid using the Castelli & Kurucz (2004) atmosphere tables, which include non-solar abundances of α-elements (O, Ne, Mg, Si, S, Ar, Ca, and Ti).

Our model grid spans the range of mass, metallicity, and α-abundance detailed in Table 3.1, while each evolution track has been run to either the helium flash or 30 Gyr, whichever occurs first. The models utilize the nuclear reaction rates of Adelberger et al. (2011) and chemical evolution of the form $Y = Y_{\text{primordial}} + \frac{\Delta Y}{\Delta Z} Z$, with $\frac{\Delta Y}{\Delta Z} = 1.4$. To model convection, YREC employs mixing-length theory (MLT, Vitense 1953; Cox & Giuli 1968) with no convective overshoot. We use opacities from the Opacity Project (Mendoza et al. 2007), supplemented with low-temperature opacities of Ferguson et al. (2005), for a Grevesse & Sauval (1998) solar mixture of elements, and the OPAL equation of state (Rogers & Nayfonov 2002). A solar calibration sets the values of the mixing length parameter $\alpha = 1.86$, solar hydrogen mass fraction $X_\odot = 0.7089$, and solar metallicity $Z_\odot = 0.0183$. The rotational evolution uses solid-body rotation and the angular momentum loss of Eq. (3.1), with $f_K = 6.575$, $\omega_{\rm crit} = 3.394 \times 10^{-5}$ s^{-1}, disk-locking timescale $\tau_{\rm disk} = 0.281$ Myr, and initial disk period $P_{\rm disk} = 8.134$ days (the "fast-launch" conditions of van Saders & Pinsonneault 2013). We calculate the convective overturn timescale using the local MLT convective velocity at one pressure scale height above the convective boundary. We note that the effective temperatures for our sample (see Sect. 3.2.2) are generally in a regime where the weakened braking observed by van Saders et al. (2016) should not be important; most of our stars are not massive enough to have evolved to half of their main-sequence lifetimes within the age of the galaxy. Our tracks have been condensed in the time-domain to a more practical set of equivalent evolutionary phases (EEPs) according to the method of Dotter (2016).

3.2.2 Sample

We study the sample of *Kepler* Cool Dwarfs from APOGEE-1 (Majewski et al. 2017) as described in the target selection of Zasowski et al. (2013). APOGEE-1, one of the programs in phase three of the Sloan Digital Sky Survey (SDSS-III, Eisenstein et al. 2011), spectroscopically surveyed the entire Milky Way with resolution $R \sim 22,500$ in the near-infrared. While APOGEE was designed primarily to constrain dynamical and evolution models of our galaxy, in collecting data across all galactic regions, the survey also targeted the *Kepler* field. The APOGEE-1 dataset therefore contains stars for which we also have rotation periods from *Kepler*. The stars in our sample were specifically targeted as an ancillary program to the core APOGEE survey. They were selected using *Kepler* Input Catalog (KIC, Brown et al. 2011) parameters to have $T_{\rm eff} \leq 5500$ K, $\log g \geq 4.0$ dex, and 7 $<$ H-magnitude < 11. With this intentionally simple selection function, the target sample contained 1241 stars. However, three plates were not observed as planned, so only 930 were observed.

The three panels of Fig. 3.1 show where the stars in our sample are located on the H-R diagram, rotation–temperature space, and composition space. Following the method of García et al. (2014a), Ceillier et al. (2016, 2017), and Santos et al. (2019), we derived rotation periods from *Kepler* light curves obtained with KADACS (*Kepler* Asteroseismic Data Analysis and Calibration Software, García et al. 2011) using three high-pass filters at 20, 55, and 80 days and interpolating gaps in the data using the inpainting techniques of García et al. (2014b) and Pires et al. (2015). The rotational analysis employs wavelet decomposition based on Torrence & Compo (1998) and as implemented in the A2Z pipeline (Mathur et al. 2010), autocorrelation function (ACF, e.g., McQuillan et al. 2014), and the product of the two (composite spectrum, CS; e.g., Ceillier et al. 2017), obtaining three period estimates for each target, one for each KADACS filter. Aigrain et al. (2015) used injection/recovery methods to test the accuracy of this and other period-detection methods; they found that between 88% (noisy simulated stars) to 92% (noise free stars) of the periods recovered using this technique were accurate to within 10%. Targets with reliable rotation-period estimates are automatically selected if the different estimates agree and the heights of the ACF and CS peaks are larger than a given threshold (for details see Santos et al. 2019). For the remainder of the sample, we proceed with visual inspection. The rotation estimate that we provide and use for the subsequent analysis is that retrieved from the wavelet decomposition. Of the 930 stars in our sample, we recovered rotation

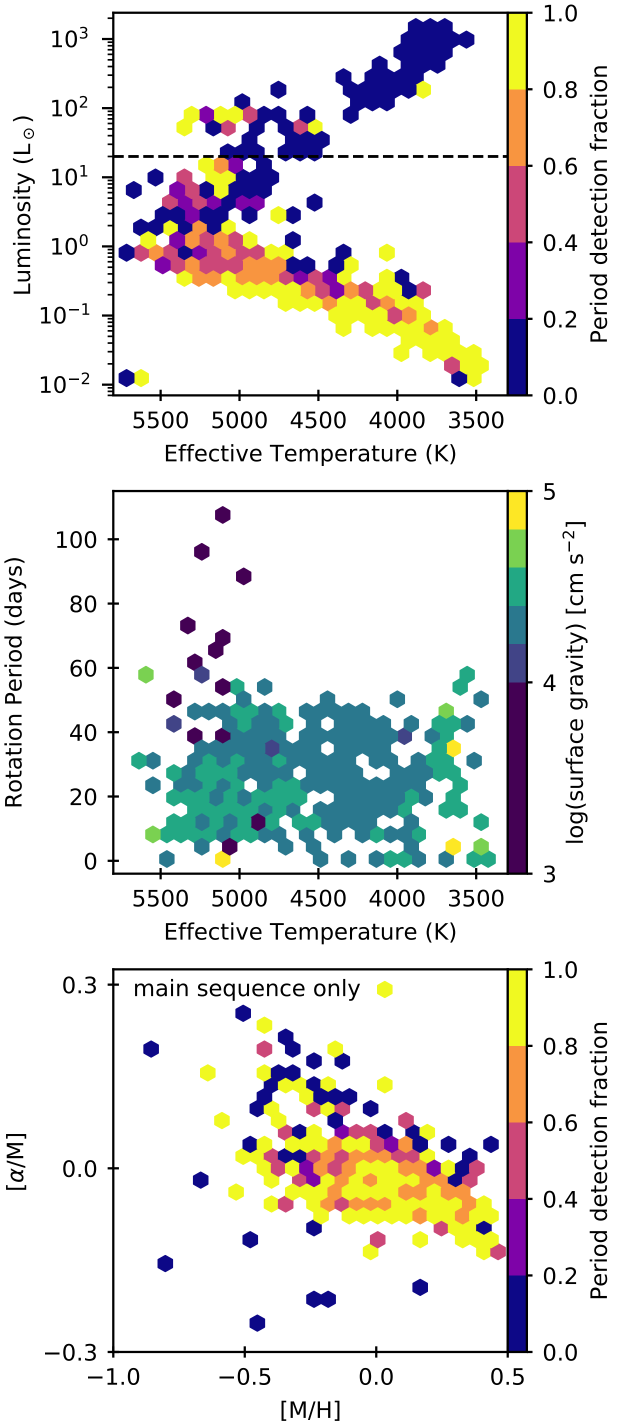

Figure 3.1: *Top:* H-R diagram for our sample of cool *Kepler* stars. We discarded giant-branch stars with $L > 20L_\odot$, shown by the black dashed line. *Middle:* Rotation period vs. temperature for stars with reliable period detections. We detected rotation in only a handful of evolved stars. *Bottom*: α-abundance vs. metallicity showing the old, "thick" disk ([α/M] $\gtrsim$ 0.1) and young, "thin" disk ([α/M] $\lesssim$ 0.1).

period estimates for 532 stars, 65% being automatically selected. The remaining stars were discarded. We detected rotation periods for more stars using this method than using autocorrelation alone: based on the detection fractions in McQuillan et al. (2014), we would expect ~ 450 detections. Our period estimates have a median uncertainty of ~ 2 days and a median relative uncertainty of $\sim 8\%$.

Periods were not reliably detected in the remaining stars for a number of reasons, likely due to noise, unfavorable orientations of the rotation axes, long rotation periods (many tens to hundreds of days), and/or small amplitudes of spot modulation. The amplitude of the spot modulation depends on the stellar inclination angle and spot latitudes, but it also depends on spot area coverage which is expected to depend on stellar age. Thus, both period and amplitude of the spot modulation are markers of age, so we suspect that we preferentially detect rotation for young stars. This is evident in the bottom panel of Fig. 3.1, where most of the metal-poor, α-rich stars (which tend to be old) are preferentially undetected in rotation.

We adopted temperatures, metallicities ([M/H]), and α-element abundances ([α/M]; α includes O, Mg, Si, S, Ca, and Ti, but is dominated by Mg, O, and Si in the dwarfs) from APOGEE Data Release 14 (Holtzman et al. 2018). These parameters were derived from spectra by the APOGEE Stellar Parameters and Chemical Abundances Pipeline (ASPCAP, García Pérez et al. 2016). ASPCAP performs a temperature-dependent calibration to the abundance measurements under the assumption that stars in a given open cluster should have homogeneous abundances. We used these calibrated values for 461 of our stars with detected rotation periods; the remaining 71 stars had no calibrated spectroscopic parameters available, usually due to the proximity of the stars' temperatures or metallicities to ASPCAP atmosphere grid edges. For these stars we used the uncalibrated values. The temperatures have a median uncertainty of 100 K, while the metallicities and α-abundances have median formal uncertainties of 0.06 and 0.02 dex, respectively. The spectroscopic temperatures are, on average, about 20 K cooler than their photometric counterparts reported by Berger et al. (2018), with a root-mean-square scatter of 147 K. These offsets are consistent with those reported by Holtzman et al. (2018) for dwarfs in APOGEE DR14. Serenelli et al. (2017) noticed a dispersion in ASPCAP metallicity when compared to values derived from optical spectroscopy; following their practice, we added a 0.1 dex uncertainty in quadrature to the ASPCAP formal uncertainties in both [M/H] and [α/M]. For the uncalibrated parameters where uncertainties were not reported, we adopted 100 K uncertainty in temperature and 0.1 dex uncertainty in both metallicity and α-abundance.

As an extra parameter to constrain the evolutionary states of stars in our sample, we adopted luminosities derived by Berger et al. (2018) from *Gaia* parallaxes. Our sample contains 31 stars which Berger et al. (2018) are missing, and for these we used ASPCAP-derived surface gravities to constrain evolutionary phase.

Single red giants are predicted to have very long rotation periods, and detected rotation signals in them are typically related to binary mass transfer (Tayar et al. 2015). We therefore focus on main-sequence period–age relations, discarding stars with luminosities above $20L_\odot$ from our analysis. We retain subgiants to gauge the usefulness of our braking law for non-main-sequence stars. Of the stars with no luminosity information, we removed those with $\log g < 3$. Using the luminosity and surface gravity cuts, 15 stars were removed from our sample. Finally, 40 of the remaining stars were common to the giant candidate catalog of García et al. (in prep). These stars' light curves and periodograms were visually inspected to ensure there was no contaminating power excess at the frequencies from which we derived rotation periods. Upon visual inspection, another 15 stars were cut, leaving 502 for further analysis.

Because our original sample was selected using KIC surface gravities, the giant contamination represents cases in which the original KIC was ineffective at separating evolved and unevolved stars. The fraction of contaminating giants and subgiants in our original sample of 930 stars is 25%. This increases to 45% when we consider stars redder than $K_p - J = 2$, in contrast to 74% found in Mann et al. (2012) for stars with KIC-determined $\log g > 4$, *Kepler* magnitude $K_p < 14$, and $K_p - J > 2$. The difference is likely due to the magnitude cut in our sample ($7 < H$-magnitude < 11): our faint-end limiting magnitude results in a smaller observed volume and less giant contamination than Mann et al. (2012) observed.

3.2.3 Markov Chain Monte Carlo (MCMC)

To obtain ages, we used Markov Chain Monte Carlo sampling to map the stellar observables of metallicity, temperature, luminosity, and period onto the fundamental parameters of mass, bulk composition, and age. We ran chains for 502 stars using the Python `emcee` package developed by Foreman-Mackey et al. (2013). `emcee` samples a posterior probability distribution using an ensemble of walkers, each running its own Markov chain.

For priors, we used uniform constraints on mass, metallicity, and α-abundance only to ensure the sampler remained within our model grid edges. For the log-likelihood, we used a χ^2 in the form of:

$$\ln P_{\rm like} = -\frac{1}{2}(\chi^2 + \chi^2_{\rm evo})$$
$$\chi^2 = \sum_i^N \left(\frac{x_{{\rm obs},i} - x_{{\rm mod},i}}{\sigma_{x_{{\rm obs},i}}} \right)^2,$$

where the $x_{{\rm obs},i}$ are the *Kepler* rotation period and ASPCAP-derived $T_{\rm eff}$, [M/H] and [α/M]; and the $x_{{\rm mod},i}$ are the sampled YREC model parameters. The second term $\chi^2_{\rm evo}$ was used as a relatively weak constraint on the evolutionary state, and only when the sampled model luminosity was different from the observed luminosity by more than a factor of two. It took the form:

$$\chi^2_{\mathrm{evo}} = \begin{cases} \left(\dfrac{\frac{1}{2}L_{\mathrm{obs}} - L_{\mathrm{mod}}}{\sigma_{L_{\mathrm{obs}}}}\right)^2, & L_{\mathrm{mod}} < \dfrac{1}{2}L_{\mathrm{obs}} \\ 0, & \dfrac{1}{2}L_{\mathrm{obs}} \leq L_{\mathrm{mod}} \leq 2L_{\mathrm{obs}} \\ \left(\dfrac{2L_{\mathrm{obs}} - L_{\mathrm{mod}}}{\sigma_{L_{\mathrm{obs}}}}\right)^2, & L_{\mathrm{mod}} > 2L_{\mathrm{obs}} \end{cases}$$

This form encouraged the walkers to remain within a factor of two of the observed luminosity without allowing luminosity the same constraining power as rotation period and temperature. Thus, if the period and luminosity provided contradictory constraints (e.g., in the case of an unresolved wide binary system, the observed luminosity would be greater than that of a single star, but the observed period may be uncontaminated), the period information would dominate the likelihood value.

An approximation was necessary to make the composition data compatible with the model grid we used. Namely, about half of our stars had α-abundances that were less than solar (with the lowest being [α/M]$= -0.44$), but the Castelli & Kurucz (2004) atmosphere tables are available only for [α/M] $= 0$ or $+0.4$. Rather than extrapolate to subsolar values, we modeled any star with an α-abundance less than solar using a solar value. Since α-enhancement has an effect on the angular momentum loss, this will have induced a slight bias in our determined ages for these stars. We discuss this bias in Sect. 3.4.1.

3.3 Results

For the MCMC sampler, we used 12 walkers, a burn-in phase of 300 iterations, and a final sampling of 5000 iterations. We allowed our chains to be run to at least 50 autocorrelation times to ensure convergence to a single region of our sampling space. We also attempted

Table 3.2: MCMC Offset Statistics

	mean	median	RMedS
$\Delta T_{\rm eff}$ (K)	23	16	16
Δ[M/H] (dex)	0.02	0.02	0.03
Δ[α/M] (dex)	0.05	0.06	0.06
$\Delta P_{\rm rot}$ (days)	0.17	0.12	0.14

Note. Offsets of Markov chain median values to corresponding input values. Statistics were computed only for stars whose chains we labeled as "good" (see Sect. 3.3). For α-abundance, the statistics were computed using only stars with positive input values, as stars with negative input values have biased chains due to the grid edge in [α/M].

runs using up to 50 walkers and 10,000 iterations for ten stars to test convergence and found our estimates with shorter chains to be robust.

We obtained chains for the 502 stars in our sample. If the input values of temperature, rotation period, metallicity, and α-abundance (for positive [α/M] only) were within the 68% credible interval of the chain, we labeled the chain as "good". With these criteria, 483 stars received the label of "good". We computed the mean, median, and root-median-square offset (RMedS) between the input parameters and the median value of their corresponding chains for "good" stars; these values are shown in Table 3.2. For all input parameters, the mean and median offsets are approximately equal to the root-median-square values, which we take to represent the median scatter about zero. In addition, the scatter in each of the four parameters is smaller than the median uncertainty in the input quantity. These demonstrate that the offsets between the input parameters and their respective model parameters are consistent with zero, indicating that our chains are well-converged to their input parameters.

Given a value for each of these input quantities, a model provides other useful predictions as well. For example, we obtained as auxiliary quantities luminosity, radius, and mass, which provided another useful check for convergence and internal consistency. Fig. 3.2 depicts the Markov chain medians of these quantities compared to values from the literature. The most obvious feature is the group of stars that fall along the line $\Delta L = -\frac{L_{\rm lit}}{2}$,

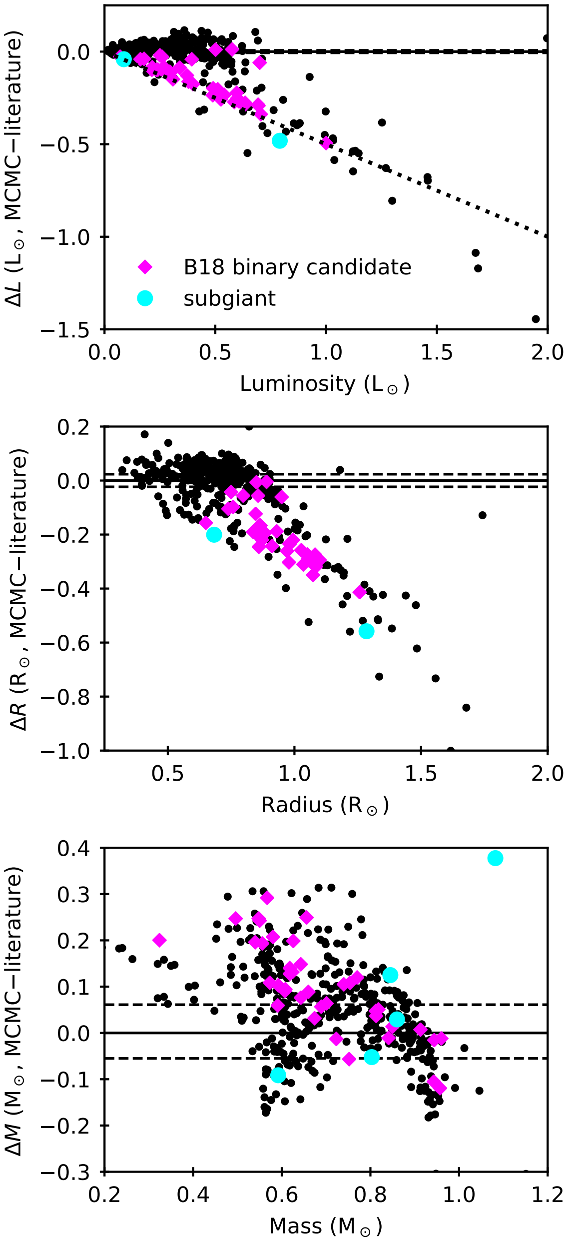

Figure 3.2: Comparison of inferred stellar parameters to literature values. Differences are given as posterior median minus the literature value; the dashed lines represent the median uncertainty in the literature values. The dotted line in the top panel represents $\Delta L/L = 50\%$, which is the maximum offset expected if the system is truly an equal-mass binary. The literature values of luminosity and mass are from Berger et al. (2018) and Mathur et al. (2017), respectively, while the comparison radii were derived from luminosity and ASPCAP temperature. The 11 subgiants were reasonably well fit, but are out of view on the luminosity and radius panels.

i.e., $L_{\mathrm{lit}} = 2L_{\mathrm{model}}$. This line is where we would expect equal mass binaries to fall, and Berger et al. (2018) photometrically classified some ($\sim 30\%$) of the stars along this line to be binary candidates, as marked by the magenta squares in the figure. The ~ 30 black points along the same line may be unconfirmed binaries or stars with flux pollution from another source. Since the radii are derived from the luminosities, the same feature is seen in the radius plot.

Masking the stars confirmed as binaries, we computed statistics for the predicted luminosities, radii, and masses in a similar manner as for the input parameters. The remaining 415 stars have a median scatter about the one-to-one line of $0.01L_\odot$, $0.01R_\odot$, and $0.05M_\odot$ in luminosity, radius, and mass, respectively. These values are comparable to the claimed uncertainties in the literature. For the stars with a Rossby number greater than that of the Sun (for which weakened braking may be important), the median scatter in L, R, and M are $0.03L_\odot$, $0.03R_\odot$, and $0.06M_\odot$. Since these parameters were not directly used in the likelihood computation, the proximity of the chain medians to the literature values further reassures that our chains are converged.

3.3.1 Gyrochronological Ages

In sampling effective temperature, rotation period, metallicity, and α-abundance, we obtained posterior distributions of ages for our sample of 483 cool *Kepler* dwarfs. We report for the first time gyrochronological ages inferred using full evolutionary models. The ages and other relevant stellar parameters for our sample are listed in Table 3.3. We consider the ages in this table to be reliable given our model assumptions. The distribution of ages in our reliable-period sample as well as the distribution of relative uncertainties are shown in Fig. 3.3.

Table 3.3: APOGEE–*Kepler* Cool Dwarf Input and Output Parameters

KIC ID	$T_{\rm eff}$ (K)	σ_T (K)	[M/H] (dex)	$\sigma_{[\rm M/H]}$ (dex)	[α/M] (dex)	$\sigma_{[\alpha/\rm M]}$ (dex)	$P_{\rm rot}$ (days)	σ_P (days)	L ($L_\odot$)	σ_L^- ($L_\odot$)	σ_L^+ ($L_\odot$)	Age (Gyr)	$\sigma_{\rm age}^-$ (Gyr)	$\sigma_{\rm age}^+$ (Gyr)
1432745	4600	98	0.171	0.118	-0.024	0.102	21.810	1.701	0.168	0.003	0.003	2.882	0.347	0.377
1724975	5259	107	-0.011	0.117	-0.042	0.101	10.607	0.748	0.854	0.018	0.019	1.030	0.105	0.114
1996721	5019	100	-0.005	0.115	0.012	0.101	31.932	3.419	0.295	0.007	0.007	6.037	0.967	1.115
2018047	4049	102	-0.375	0.116	0.103	0.103	43.017	2.450	0.075	0.001	0.001	8.786	0.888	1.020
2156061	4284	96	0.146	0.117	-0.047	0.103	29.383	3.065	0.450	0.116	0.192	4.448	0.720	0.815
							...							

Note. The input data and derived rotation-based ages for stars in the APOGEE-*Kepler* cool dwarfs sample. We list the *Kepler* IDs, APOGEE effective temperatures, bulk metallicities, and α-enhancements with formal uncertainties, rotation periods with uncertainties estimated from *Kepler* light curves, luminosities with uncertainties inferred from *Gaia* parallaxes by Berger et al. (2018), and the median of the age posteriors with 68% credibility limits. Table 3.3 is published in its entirety in the machine-readable format. A portion is shown here for guidance regarding its form and content.

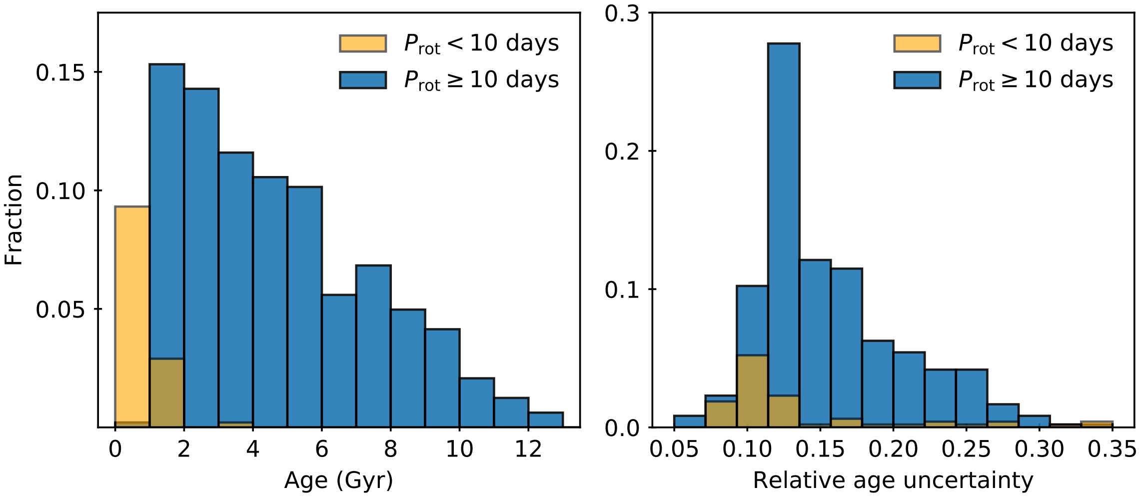

Figure 3.3: *Left*: Distribution of median ages for "good" stars. Stars with rotation periods less than ten days are likely to be synchronized binaries according to Simonian et al. (2019), so they are shown separately in orange. *Right*: The distribution of relative age uncertainty. The median age uncertainty is 14%, which is better than the median age uncertainties for other age determination methods on comparable samples.

Simonian et al. (2019) found that more than half of stars with observed periods between 1.5 and 7 days are actually synchronized binaries, noting that 10 days is the boundary longer than which no synchronization should take place (but see also Fleming et al. 2019). For this reason we plot stars with periods shorter than 10 days separately from those with longer periods.

Unlike the case of solar analogs, we clearly predict a large number of old ages for our targets, with no obvious break in the distribution. The age distribution peaks around 1 to 2 Gyr, which is younger than that found by Haywood et al. (2013) and Buder et al. (2019), but consistent with the result of Silva Aguirre et al. (2018), who also studied stars in the *Kepler* field. Even if the fast rotators are not binned separately, the peak remains unchanged. The median relative age error is 14%, which is better than the 20–30% range usually seen for isochrone ages of similar stellar populations (e.g., Buder et al. 2019, who studied over 7000 dwarf and main-sequence-turnoff stars in the Galactic Archaeology with HERMES survey, GALAH). For a discussion of systematic bias in our age estimates, see Sect. 3.4.1.

We do not expect our sample to be representative of the distribution underlying the galactic stellar population for several reasons. First, our selection criteria remove stars that have KIC surface gravity $\log g < 4$ dex. Since these stars are evolved and therefore preferentially older, this cut biases our sample toward younger stars. Moreover, requiring that our stars' rotation be detectable biases the sample toward more active stars, which also tend to be younger. Furthermore, although the original sample was selected with simple cuts in magnitude, temperature, and surface gravity in the KIC, the KIC itself is somewhat biased in its determination of stellar parameters.

3.3.2 A word on rotational detection bias

Our sample of stellar ages is uniquely biased in comparison to other such galactic samples: our ability to infer ages is tied directly to our ability to detect rotational modulation. This modulation is stronger in younger, more rapidly rotating stars. At fixed rotation period, it is stronger in stars with cooler temperatures and deeper convective envelopes (see McQuillan

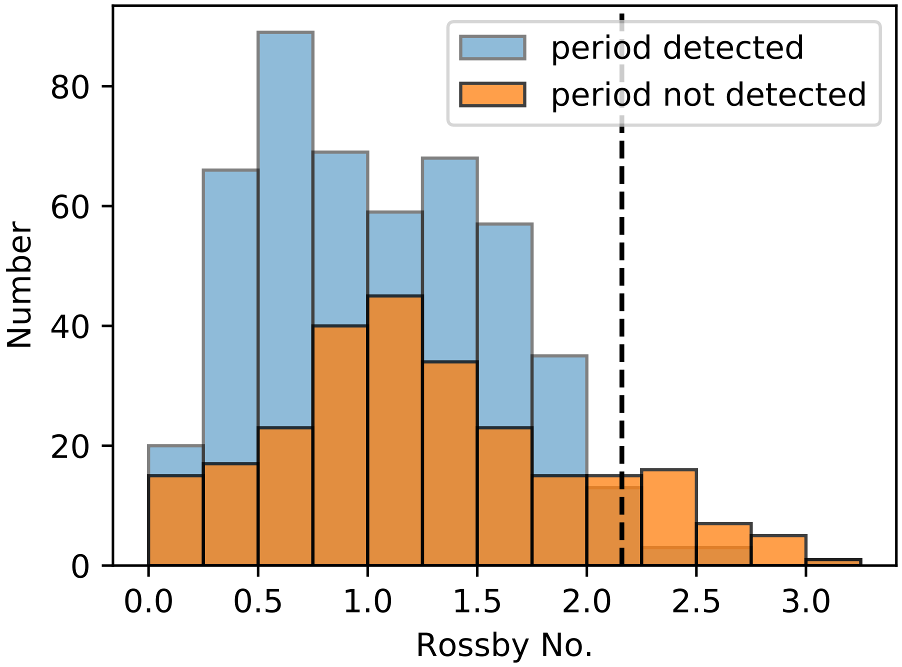

Figure 3.4: Observed Rossby numbers for the rotationally detected (blue) and estimated Rossby numbers for the undetected (orange) stars on the main sequence. The vertical dashed line is $\mathrm{Ro} = \mathrm{Ro}_\odot = 2.16$. Below this line, we expect to detect all stars in rotation with exceptions for unfavorable inclinations and spot configurations. Above it, we expect stars' variability to fall below detection thresholds.

et al. 2014; van Saders et al. 2019). α-enhancement also tends to deepen convective envelopes at fixed metallicity, although it is a second-order effect in comparison to the bulk metallicity (Karoff et al. 2018). Taken together, it means that we expect our sample to be biased against old, metal poor objects, which is clearly seen in the bottom panel of Fig. 3.1. This is in contrast to asteroseismology, which is not particularly biased against old stars, and with isochrone methods, which tend to struggle with young and intermediate age stars on the main sequence in this temperature range.

van Saders et al. (2019) suggested that stars with Rossby number $\mathrm{Ro} > 2$ might become undetectable in spot modulation based on the solar-temperature stars in the McQuillan et al. (2014) field sample, creating a sharp "detection edge" at long periods. For the metallicities and α-enhancements of stars undetected in spot modulation in our sample, we would have expected all stars cooler than 4500 K to fall at Ro < 2 for $t < 12$ Gyr, and thus to fall below this detection edge.

For those stars with measured rotation periods, we calculated the Rossby number (Ro $= P_{\rm rot}/\tau_{\rm cz}$) using the observed period and the model convective overturn timescale from our MCMC stellar parameter estimation. To estimate a distribution of Rossby numbers for the stars *not* detected in rotation we used the following recipe:

1. We split the stars into an α-rich and α-poor sequence using the same [M/H]–[α/M] selection as Silva Aguirre et al. (2018, see their Fig. 8).
2. We randomly sampled an age for each star from the appropriate α-rich or α-poor age distribution of Silva Aguirre et al. (2018, see their Fig. 9).
3. Using the star's ASPCAP abundances, sampled age, and mass from Mathur et al. (2017), we interpolated a Rossby number for each star from our stellar model grid.

Fig. 3.4 shows a histogram of Rossby numbers for the rotationally undetected stars, compared with the MCMC-estimated Rossby numbers for our "good" sample. While we can say little about the robustness of a Rossby number estimate for an individual undetected star, statistically the set of Rossby numbers should provide some insight into the sample of rotationally undetected stars. Strikingly, the undetected stars are not overwhelmingly predicted to have high Rossby numbers: the undetected stars, like the detected stars, mostly have Ro < 2, save a small but notable tail of undetected stars with predicted Rossby numbers Ro > 2. This suggests that the non-detections are only mildly biased against the oldest stars; most are likely undetected due to unfavorable spot patterns or inclinations.

Another view of detectability is encapsulated in Fig. 3.5, which shows a 2D histogram of the fraction of stars detected in rotation as a function of effective temperature and α-enhancement. We include all stars in our sample with ASPCAP $\log g > 4$ so that the

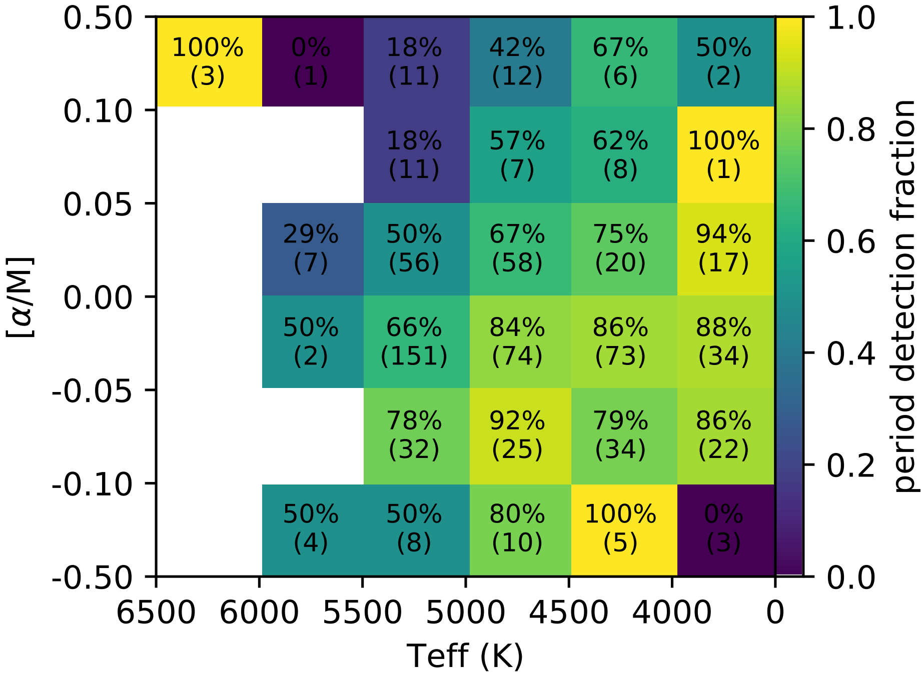

Figure 3.5: Rotation detection fraction as functions of temperature and α-enhancement for stars with $\log g > 4$. Color denotes the fraction of stars detected in rotation in each bin, while each bin is labeled with both the detection fraction and the number of stars contained in that bin. Like McQuillan et al. (2014), we find better detectability at cooler temperatures, but we also find α-enhanced stars are more difficult to detect in rotation, presumably due to the link between α-enhancement with age.

fractions are unaffected by contamination by giant stars. Like McQuillan et al. (2014), we find higher detection fractions at cooler temperatures. The decreasing detectability with increasing α-enhancement represents the difficulty of detecting rotation in progressively older and more slowly rotating stars.

3.3.3 Chemical Evolution Trends

Here we examine whether we recover the various chemical enrichment trends observed in studies that use ages determined from isochrones or asteroseismology.

Trends in α-abundance with age

Using our rotation-based ages, we investigated the abundance of α-elements as a function of age to look for trends in galactic chemical evolution. Our results are shown in Fig. 3.6 and are plotted over results of the similar studies of Haywood et al. (2013), Silva Aguirre et al. (2018), and Buder et al. (2019) to compare age trends. Each comparison study uses a different combination of α-elements; to ensure accurate comparisons, we plot our ages against the appropriate combination of elemental abundances from APOGEE. We consider trends of individual α-elements with age in Appendix A.

We recover the general trend of increasing α-abundance with age. The rate of α-enhancement is consistent with the rates observed by Haywood et al. (2013) and Silva Aguirre et al. (2018) for stars younger than ~ 8 Gyr, but the sharp upturn in slope at about 8 Gyr seen by Haywood et al. (2013) is absent from our sample. Instead, we observe a spread of α-abundances for old stars more consistent with the results of Silva Aguirre et al. (2018) and Buder et al. (2019). The difference is likely due to the sample selection used by the different studies: Haywood et al. (2013) selected stars in the solar vicinity, while Silva Aguirre et al. (2018) and Buder et al. (2019) study stars in APOGEE and GALAH, which probe beyond the solar neighborhood and detect a wider variety of stars.

Perhaps the most drastic difference between our sample and the comparison samples is that we find very few stars in the old, α-enriched sequence. Fig. 3.7 shows this same result in composition space, this time colored by age. The lower, young, α-poor sequence is well populated, but the upper α-rich sequence is nearly empty. This is likely due to the fact that old, α-enhanced stars are relatively inactive and are therefore difficult to detect in rotation (see again the bottom of Fig. 3.1). Metallicity may play a role too: old stars tend to be relatively metal poor and thus have thinner convective envelopes. Presumably, this would result in weaker magnetic fields, less starspot activity, and fewer detections at fixed age. In

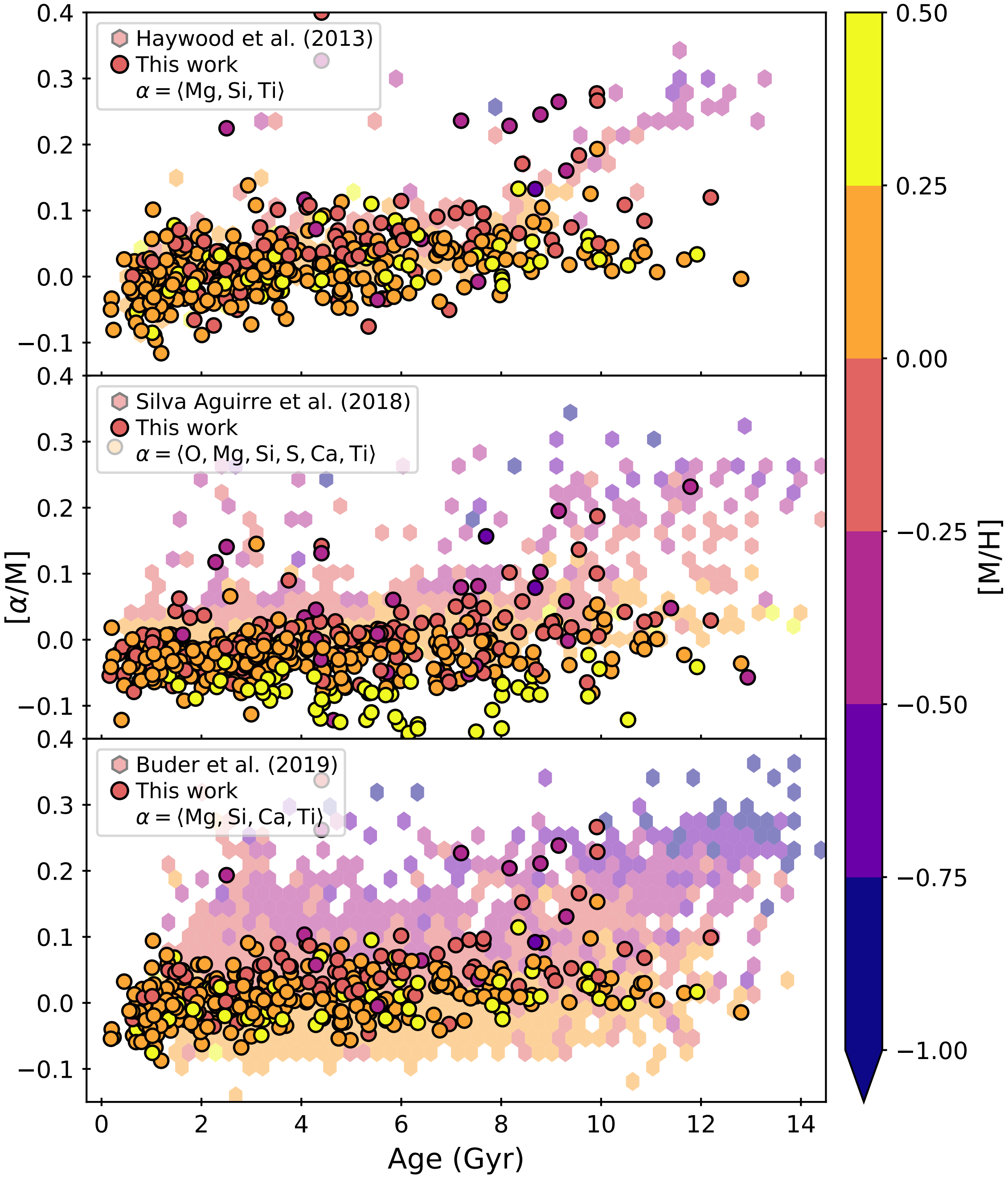

Figure 3.6: The [α/M] vs. age distribution for our "good" stars (shown in circular points), compared with results from other work (Haywood et al. 2013; Silva Aguirre et al. 2018; Buder et al. 2019, shown in hexagonal bins). We recover the α-enhancement slope for stars younger than 8 Gyr seen by Haywood et al. (2013), but we also find old, α-poor stars seen by Buder et al. (2019) and Silva Aguirre et al. (2018) that Haywood et al. (2013) did not see. Our lack of old, α-enhanced stars is likely due to observational biases (see Sect. 3.3.3).

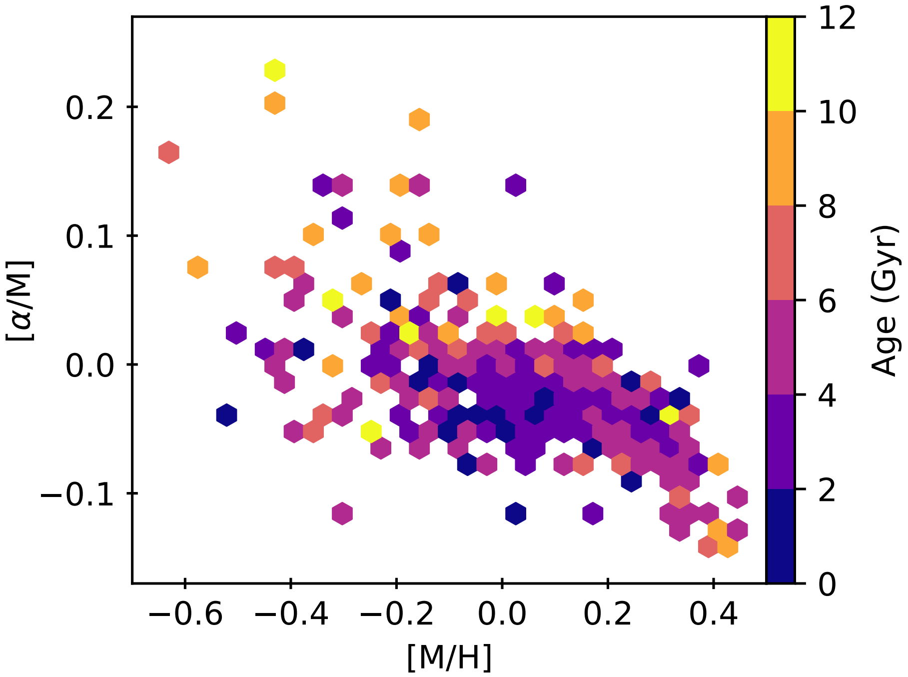

Figure 3.7: The same composition-space diagram as the bottom of Fig. 3.1, except here the bins are colored by rotation-based age. As expected, most of the α-rich ($[\alpha/M] \gtrsim 0.1$) stars are fairly old. We emphasize that the lack of stars in the α-enhanced disk is mainly due to two observational biases: (1) the stars *Kepler* observed in the α-rich, thick-disk sequence were usually evolved and showed little or no rotational modulation in their light curves, and (2) older main-sequence stars tend to be less magnetically active and are consequently more difficult to detect in rotation.

addition, almost all the stars in our sample are located within 0.5 kpc of Earth. The α-rich "thick" disk stars tend to be farther away, mostly at distances greater than 1 kpc (see Fig. 4 of Hayden et al. 2015), well outside of *Kepler*'s peak detectability.

Young, α-rich stars

Our sample includes 3 young (< 6 Gyr), α-rich ([α/M] > 0.13) stars, selected to have periods $P > 10$ days. These stars are present in numerous other surveys (Martig et al. 2015; Chiappini et al. 2015; Silva Aguirre et al. 2018; Buder et al. 2019) where ages are derived by a variety of other means including isochrone fitting, asteroseismology, and the [C/N]–mass relationship in giants. Chiappini et al. (2015) suggested that this population is formed in the region near corotation with the Galactic bar, and is then subject to strong radial migration. They may also represent a blue straggler population (Martig et al. 2015). We caution that if these stars are indeed merger products, our rotation-based ages are unreliable: if mass transfer spins up the stars, they will appear young when ages are inferred through rotation–age relations. Interestingly, these stars are also unusually kinematically hot (see Fig. 3.8).

Old, α-poor stars

Buder et al. (2019) found that 30% of the old (age $>$ 11 Gyr) stars were α-poor ([α/Fe] $<$ 0.125). Our sample is even more strikingly α-poor: 89% of stars older than 11 Gyr have low α abundances. We suspect that this is largely due to the sample bias discussed above. The old stars in this sample are predominantly α-poor, but they are also metal-rich ($-0.25 <$ [M/H] < 0.45). We suspect that the rotational detection bias preferentially removes old, metal-poor stars from the sample, resulting in an apparent enrichment of old, metal-rich, α-poor stars.

Metallicity dispersion

We find that the dispersion in metallicity increases for older stars, similar to Buder et al. (2019) and Silva Aguirre et al. (2018). We bin our "good" sample with periods greater than 10 days in 1.5 Gyr bins (each with more than 20 stars), and find that the scatter in metallicity increases from 0.14 at 2.0 Gyr to 0.22 at 5.0 Gyr, to 0.26 at 9.5 Gyr, consistent with the increased scatter found in stars with isochrone ages in Buder et al. (2019).

Metallicity distribution

The distribution of metallicities in our sample corroborates the suspicion of detection bias: while our full sample (including stars for which we did not detect rotation) has

$\langle$[Fe/H]$\rangle$ = -0.001 ± 0.008, our "good" sample is more metal-rich with $\langle$[Fe/H]$\rangle$ = 0.055 ± 0.009 (a 4.5-σ difference). The mean and difference are the same for [M/H] as for [Fe/H]. For comparison, the full solar neighborhood sample of APOGEE Data Release 12 (Hayden et al. 2015) has $\langle$[Fe/H]$\rangle$ = 0.01 ± 0.002, while the sample of Buder et al. (2019) is more metal-poor with $\langle$[Fe/H]$\rangle$ = -0.04 ± 0.003. The slight difference in mean metallicity between the APOGEE and GALAH samples is likely due to their respective target selections. APOGEE targeted the (metal-rich) galactic disk, while GALAH avoided it (Buder et al. 2019).

3.3.4 Kinematic trends

We examine the kinematics of our sample as a function of age using the combination of positions, proper motions, parallaxes, and radial velocities from the second *Gaia* data release (*Gaia* Collaboration et al. 2018). We draw associate *Kepler* targets with their *Gaia* counterparts following the method of Berger et al. (2018), which compared the magnitudes of the *Kepler* and *Gaia* source matches, removed stars with uncertain ($\sigma_\pi/\pi > 0.2$) parallaxes, and implemented the astrometric quality cuts described in detail in Berger et al. (2018), Lindegren et al. (2018), and Arenou et al. (2018). In total, 381 stars in our sample survive the Berger et al. (2018) cuts, have reported *Gaia* RV values (*Gaia* Collaboration et al. 2018), and have a "good" label. We convert the *Gaia* five-parameter astrometic solution and line of sight velocities into U (radial), V (azimuthal), and W (vertical) velocities following Johnson & Soderblom (1987). We adopt a peculiar velocity for the Sun of $(U_\odot, V_\odot, W_\odot) = (11.0, 12.24, 7.25)$ km/s from Schönrich et al. (2010). We estimate velocity errors by propagating the full *Gaia* 5D $(\alpha, \delta, \varpi, \mu_{\rm ra}, \mu_{\rm dec})$ covariance matrix through the coordinate transformations, assuming an independent Gaussian error distribution for the line of sight velocities.

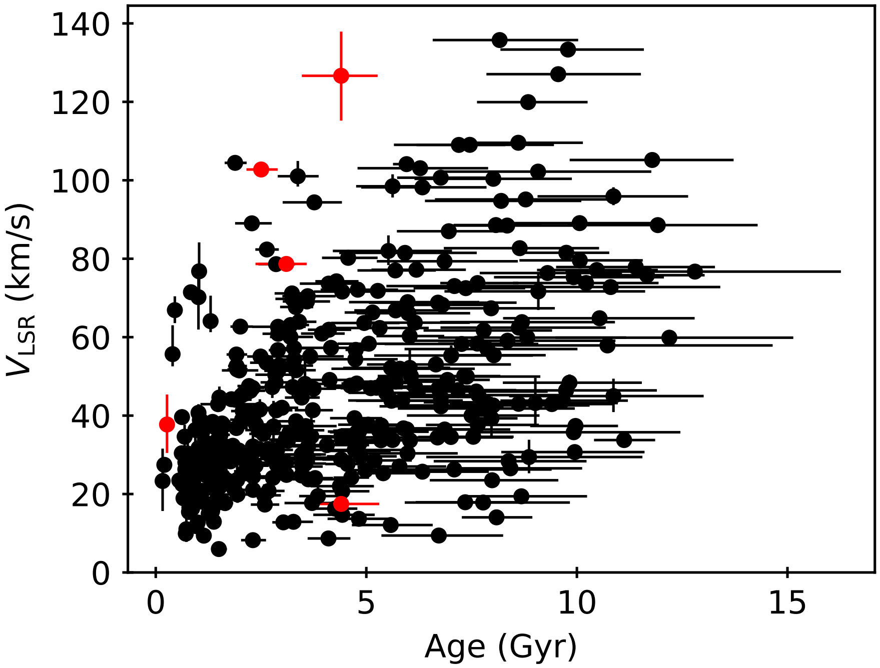

Figure 3.8: Velocities with respect to the Local Standard of Rest ($V_{\rm LSR} = \sqrt{U_{\rm LSR}^2 + V_{\rm LSR}^2 + W_{\rm LSR}^2}$) for sample stars with "good" designation, displaying increased velocity dispersion with age. Young α-enhanced stars ($t < 6$ Gyr, $[\alpha/\mathrm{M}] > 0.13$) are shown in red. All stars are shown, regardless of rotation period.

We show the velocities with respect to the local standard of rest in Fig. 3.8 as a function of rotation-based age. The velocity dispersion in the sample is higher in the older stars, consistent with a picture in which stars are dynamically heated over time. Our sample shows much the same behavior as the M-dwarf sample of Newton et al. (2016, their Fig. 13), who also observed an increase velocity dispersion in slow rotators, corresponding to old stars.

3.4 Discussion

We have inferred rotation-based ages for this cool-star sample in part because all other standard age determination methods fail in dwarf stars much cooler than the Sun. Even in our models, magnetic braking is calibrated using only a handful of stars with $T_{\rm eff} < 5500$K at ages greater than a few Gyr. Our inferred ages are therefore still an extrapolation of relations calibrated on largely solar-like objects. The recovery of broad kinematic and galactochemical trends seen in samples with ages determined via other means is an encouraging sign that rotation does indeed carry age information in cool stars.

While the ages we present have a median relative uncertainty of 14%, we note that this relates to precision, not accuracy. This precision comes under the assumption that our choice of braking law is correct, and under a particular set of input physics for the stellar models. With these assumptions, the *relative* ages of our stars are likely to be accurate, but we can make no such claim for the absolute ages. Fortunately, investigations of evolution generally rely on relative ages, so accurate absolute ages are not always necessary.

A systematic look at the effects of different stellar model grids, magnetic braking models, and angular momentum transport prescriptions is beyond the scope of this work. However, here we do examine the impacts of a range of different initial rotation periods and the manner in which composition is incorporated into the modeling.

3.4.1 Systematic uncertainties in gyrochronological ages

The uncertainties associated with model-based gyrochronological ages include effects of composition and initial conditions. For composition, changing the bulk metallicity or detailed abundances changes the depth of the stellar convection zone, which in turn affects the rate of spin-down. Meanwhile, it has been demonstrated that a star "forgets" its initial conditions after some sufficient amount of time has passed, usually less than a Gyr for G- and K-dwarfs, but up to several Gyrs for the coolest M-dwarfs (e.g., Epstein & Pinsonneault 2014; Gallet & Bouvier 2015). Any lingering dependence on initial conditions remains to be quantified. Using our model grid, we performed three tests to quantify independently the effects of metallicity, α-abundance, and initial conditions on our derived ages.

First we investigated the effects on age if metallicity is ignored, i.e., if one assumes a star has solar composition. We attempted to mimic the scenario one might encounter when attempting to use gyrochronology relations on a poorly studied field star whose temperature and period are known, but whose metallicity, detailed abundances, or initial rotation period are not. We employed the following procedure:

1. Interpolate ages for two stars from the model grid using the same randomly sampled mass, α-abundance, and rotation period, but with different metallicities: one with [M/H] = 0.5, and one with a solar value (i.e., [M/H] = 0)

2. Compare the ages for the two stars, treating the metal-rich star as the "real" star, and the star with solar abundance as an "incorrect" model.

3. Repeat until all regions of the model grid have been sufficiently sampled

We repeated this test for a metal-poor case as well, using a "real" star with [M/H] = -0.5.

The second test was like the first except that the α-enhancement was used as the manipulated variable. In other words, we sampled two stars of the same mass, metallicity, and rotation period, but differing α-abundances of [α/M] = 0 (the solar case) and 0.4 (the enhanced case).

Finally, in our third test we sampled stars of the same mass, metallicity, and α-abundance, but with different initial conditions. The control sample employed the standard "fast-launch" conditions of disk-locking timescale $\tau_{\text{disk}} = 0.281$ Myr and disk period $P_{\text{disk}} = 8.134$ days. The test sample, on the other hand, used "slow-launch" conditions of $\tau_{\text{disk}} = 5.425$ Myr and $P_{\text{disk}} = 13.809$ days (van Saders & Pinsonneault 2013). These values were calibrated using stars in the Pleiades cluster (125 Myr old) and M37 (550 Myr).

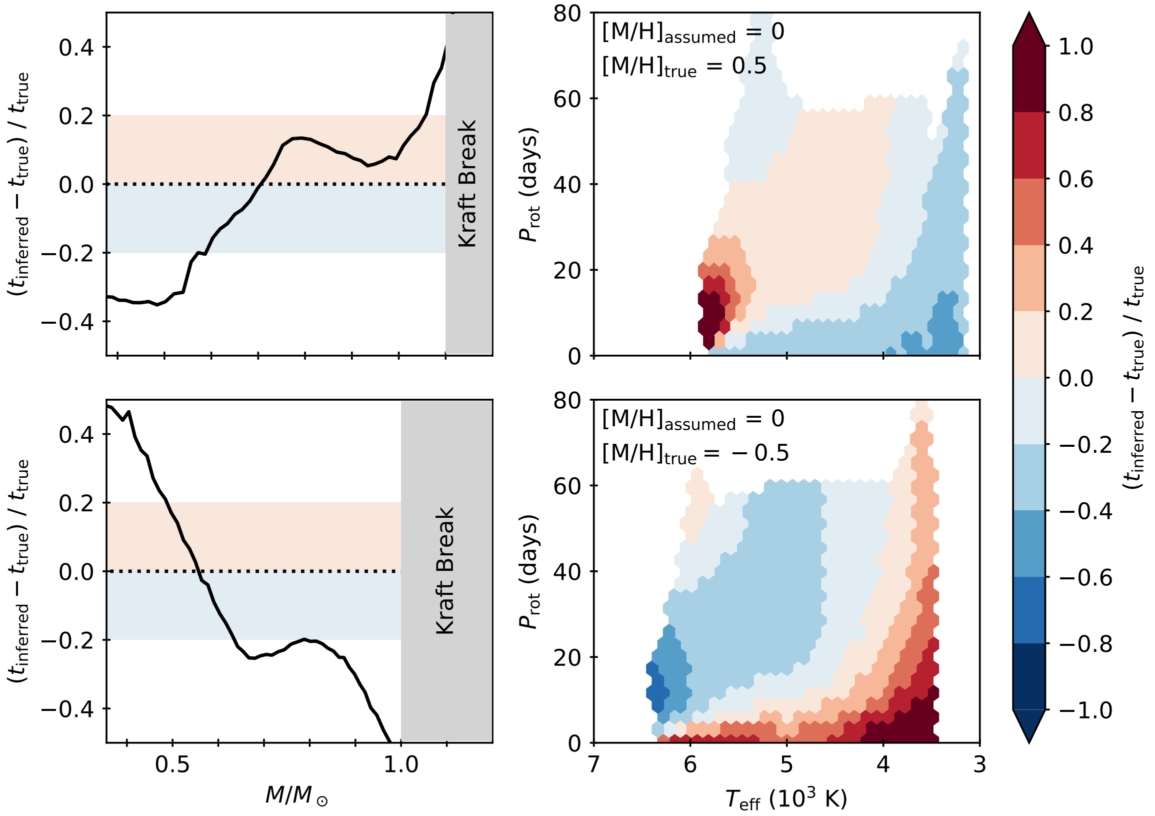

Figure 3.9: Fractional bias in inferred age when solar metallicity is incorrectly assumed and the actual metallicity is 0.5 dex (top) and -0.5 dex (bottom). *Left:* Age bias changes as a function of mass. Below a solar mass, the effect can range from -40%–10% in metal-rich stars, but the effect is slightly worse for metal-poor stars and at the Kraft break. *Right:* The same age bias now shown on the $P_{\rm rot}$–$T_{\rm eff}$ diagram. The bias is worst in M-dwarfs (where calibration is poor) and stars near the Kraft break (where the use of gyrochronology is ill-posed).

Each test consisted of 50,000 random samples, and the results are shown in Figs. 3.9 and 3.10. In all plots, the value $(t_{\rm inferred} - t_{\rm true})/t_{\rm true}$ indicates by what fraction the age is overestimated (or underestimated) under the given false assumption. The panels in a given row show the results for the same sample in two different ways. The left panels of Fig. 3.9 show the age bias as a function of mass, while the right panels show a $T_{\rm eff}$–period diagram with bins colored by the age bias. For the α-abundance and launch condition tests, the bias

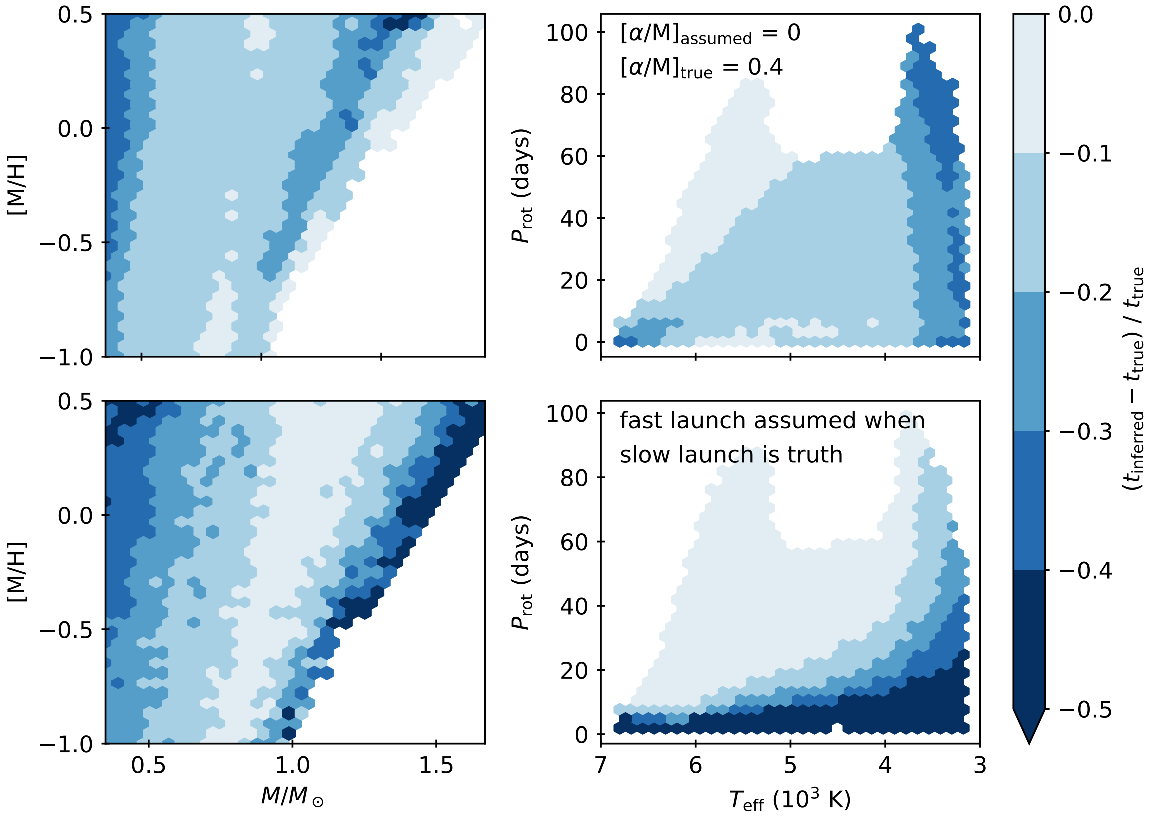

Figure 3.10: *Top*: Fractional bias in inferred age when α-abundance is incorrectly assumed to be solar and the actual enhancement is 0.4 dex. For most of the mass range where gyrochronology is validated, ignoring α-enhancement can lead to 10–20% biases. *Bottom*: Fractional bias in inferred age when fast-launch initial conditions are assumed, but the actual initial conditions are slow-launch. For late G- and K-dwarfs, the bias is less than 10%, but the error is worse for M-dwarfs, which take longer to forget their initial rotation periods.

depended on metallicity, so the left panels of Fig. 3.10 have metallicity on the vertical axis and are colored by age bias.

If one assumes solar metallicity for a metal-rich, $0.75\mathrm{M}_\odot$ star (top of Fig. 3.9), the age will be overestimated by $\sim 15\%$. The bias is much larger for stars more massive than the Sun, i.e., near the Kraft break. Here a subtle change in metallicity changes whether the star has a convective envelope and spins down over time, so the inferred rotation-based age is drastically affected. These effects are slightly worse, but in the opposite direction, for the metal-poor case: for a metal-poor, $0.75 M_\odot$ star, the age will be underestimated by $\sim 40\%$. In addition, the Kraft break occurs at lower masses in metal-poor stars, so the bias is also worse than the metal-rich case for stars slightly less massive than the Sun. On the low-mass end, the bias is reversed: for a metal-rich M-dwarf, assuming solar metallicity results in *underestimating* the age by $\sim$ 30%. However, this is also the regime in which a spread of initial rotation periods persists. Both of these cases are beyond regimes where gyrochronology has been validated: above the Kraft break, the lack of spin-down makes any kind of rotation-dating useless, while M-dwarfs suffer from a lack of calibrators. If we consider the somewhat better-studied regime of 0.5–$1.0 M_\odot$, the bias ranges from -30% (for metal-poor stars) to 15% (for metal-rich stars) when comparing the inferred ages of two stars of identical mass and period, ignoring metallicity. For the observer's case where temperature and period are known (say, for example, they are solar) and metallicity is assumed to be solar, the inferred age for a truly metal-rich ([M/H] = 0.5) star will be overestimated by $\sim$ 15%, while the inferred age for a truly metal-poor ([M/H] = -0.5) will be underestimated by $\sim$ 30%. Similarly, two stars with identical $T_{\rm eff} = 4500$K and $P_{\rm rot} = 40$ days will have ages different by $\sim$ 5% in the metal-rich case and by $\sim$ 10% in the metal-poor case. Metallicity is therefore an important consideration in full evolutionary spin-down models; more calibrators at a range of metallicities should be pursued.

The top row of Fig. 3.10 shows the results of the α-abundance test. If one assumes solar α-abundance for an α-enhanced, solar-metallicity star of $0.75 M_\odot$, detailed abundances enter the systematic error budget at the 10–20% level in a model grid. This bias remains fairly constant in the mass ranges where gyrochronology is useful, but the bias is more drastic in stars near the Kraft break, similarly to the metallicity tests. This suggests that even if the metallicity is known perfectly, rotation-based ages may be biased by as much as 20% if detailed abundances are not known to some level. Since the atmosphere tables used in our model grids are defined only for [α/M] = 0 and 0.4, we cannot say without extrapolation how this bias behaves in α-poor stars.

Finally, the bottom row of Fig. 3.10 shows the bias in age if fast-launch models are used, but the system is truly slow-launch. For late G- and K-dwarfs, assuming the incorrect launch condition generally does not result in more than a 10% bias in age because sufficient time has passed to allow them to "forget" their initial rotation conditions. For late K- and early M-dwarfs, incorrectly assuming initial conditions comes into the systematic error budget at the $\sim$ 10–20% level, with the bias growing worse toward M-dwarfs, which take longer to forget their initial conditions. The bias is also larger for stars near the Kraft break; since stars in this regime do not spin down with age, two identical stars with differing launch conditions never have the same period on the main sequence. This results in an undefined age bias, as shown by the blank bins in the bottom-left panel of Fig. 3.10.

3.4.2 Other underlying assumptions

While we have tested the sensitivity of our assumed braking law to initial conditions and metallicity, we have neglected a number of confounding factors. We assume only one form of the period–age relation. While all period–age relations reproduce the behavior of solar-temperature stars by construction, they tend to make diverging predictions at cooler temperatures (see Fig. 1 in Matt et al. 2015). This is largely a consequence of the scarcity of empirical calibrators for cool stars. The asteroseismic calibrator sample extends only to $\sim 0.8\,\mathrm{M}_\odot$ (van Saders et al. 2016) and open cluster sequences are also truncated at roughly the same mass in systems older than ~ 1 Gyr (Meibom et al. 2015; Agüeros et al. 2018; Curtis et al. 2019). A detailed assessment of systematic age offsets produced by different literature braking laws is beyond the scope of this article. Here instead we have focused on whether under the assumption of a *particular* braking law we can recover the galactochemical trends inferred using other age metrics.

Furthermore, we have neglected the impact of internal angular momentum transport in our models. To maintain solid-body rotation, the transport in the interior must be fast in comparison to the angular momentum loss from the surface, which is not necessarily true during all phases of evolution. In so called "two-zone" models (MacGregor & Brenner 1991), the core and envelope are treated as separate zones, with angular momentum transport occurring between them on a characteristic timescale $\tau_{\text{c-e}}$. Two-zone models can display slower rotation than the solid body case (at fixed age) while the core has had insufficient time to couple (the effective angular momentum reservoir being depleted by magnetized winds is smaller), but faster than solid body rotation once the core and envelope recouple. Recoupling timescales in Sun-like stars are $\tau_{\text{c-e}} \approx$ 10–55 Myr (Denissenkov et al. 2010; Gallet & Bouvier 2015; Lanzafame & Spada 2015; Somers & Pinsonneault 2016), while for $0.5 M_{\odot}$ stars $\tau_{\text{c-e}} \approx 10^2$–$10^3$ Myrs (Gallet & Bouvier 2015; Lanzafame & Spada 2015). During the preparation of this manuscript, Curtis et al. (2019) published rotation periods for K- and M-dwarfs in the 1 Gyr old cluster NGC 6811, and showed that spin-down appears to stall between the ages of Praesepe ($\sim$ 700 Myr) and NGC 6811 (1 Gyr), which they attribute to potential core-envelope decoupling. However, van Saders et al. (2019) showed that the longest-period stars from McQuillan et al. (2014) with $T_{\text{eff}} < 5000$K have periods fully consistent with a braking law of the solid body form that we have adopted here for stars roughly the age of the galactic disk, suggesting that the impact of this stalled braking does not persist for old ages. The impact of core-envelope decoupling on the observed rotation periods in K- and M-stars is uncertain, due again to a lack of calibrators with known ages. While a detailed treatment of core-envelope decoupling is also beyond the scope of this article, we caution that if it is important, the age scale we present here is likely stretched or compressed with respect to the true underlying age scale, particularly at ages of hundreds of Myr (Sun-like stars) to several Gyr (M-dwarfs).

3.5 Summary and Conclusion

We have presented gyrochronological ages for stars from the APOGEE-*Kepler* Cool Dwarf sample. In doing so, we have quantified sources of bias that must be considered when inferring ages from rotation, and we have reproduced chemical–age trends in the literature using an independent means of age determination. Our results are as follows:

- We provide rotation-based age estimates for 483 stars (mostly cool dwarfs) in the *Kepler* field. In contrast with gyrochronology results from solar analogs, we find a substantial population of stars older than 4 Gyr with no evidence for a sharp detection threshold below at least 10 Gyr.
- Our age distribution peaks at younger ages than seen in broader chronology studies, but it is consistent with studies of *Kepler* giants.
- We recover the trend of increasing α-abundance with age for young ($<$ 8 Gyr) stars seen in other studies.
- We find a population of old ($>$ 8 Gyr), α-poor stars seen in recent studies.
- We see a clear trend of increasing velocity dispersion in old stars.
- We observe 3 young, α-rich stars in our sample. Because mass transfer would affect rotation periods, we cannot differentiate between whether these are truly young, single, α-enhanced stars or merger/interaction products. However, these stars are kinematically hot, making them more consistent with an older population, which may favor the merger hypothesis.

- There is tentative evidence for a drop in detection efficiency for α-rich stars relative to α-poor ones, which may indicate that there is an age bias in gyrochronology for stars older than 10 Gyr, even on the lower main sequence.
- We find that ignoring metallicity effects in gyrochronology can result in biases in age estimates as low as -30% for metal-poor stars and as high as 15% for metal-rich stars.
- Similarly, ignoring detailed abundance patterns such as α-enhancement can result in biases at the 10–20% level.
- Initial conditions enter the systematic error budget below the 10% level for late G- and early K-dwarfs, but at $\sim$ 10–20% for late K- and early M-dwarfs.

Our results demonstrate the power of gyrochronology as a tool for problems like galactic evolution. They also underscore the assumptions inherent in rotation-based age inference and the observational biases associated with detecting rotation based on stellar spot modulation. The limits of our study highlight the need for larger and deeper samples if rotation continues to be used to probe the history of the Milky Way. While *Kepler* revolutionized the study of stellar rotation, its pointing near the galactic disk meant that the farthest (and oldest) reaches of the galaxy remain poorly probed. The *Transiting Exoplanet Survey Satellite* (*TESS*, Ricker et al. 2015), due to the orientation of its continuous viewing zones out of the galactic disk, will probe further into the α-enhanced disk than *Kepler*. Consequently, *TESS* will enable gyrochronological study for a much broader population of stars.

Together, the abundance of precise rotation periods from *Kepler* and large spectroscopic datasets such as APOGEE provide valuable resources for inferring stellar ages. Whereas not long ago, isochrone-based techniques offered the most reliable age estimates for large sets of stars, we have now entered an era in which rotation-based ages can compete with and surpass the precision and feasibility of other chronometers. This will be essential in understanding evolution on a galactic scale, which requires detailed knowledge of age with chemistry, kinematics, and position for immense numbers of stars.

Chapter 4

The TESS Stellar Rotation Catalog

Now that we have demonstrated the ability of deep learning to see through TESS systematics to recover rotation periods longer than 13.7 days and established a modeling framework, we will apply these techniques to a sample of stars in the TESS Southern Continuous Viewing Zone (SCVZ). We obtain reliable rotation periods for 9,837 stars and present the first distribution of TESS stellar rotation periods longer than 13 days. We combine these period estimates with spectroscopic temperatures, chemical abundances, and surface spot filling fractions to construct our science sample. With this sample we explore the detectability of rotation in TESS as a function of fundamental stellar parameters and investigate the spot covering fractions of stars at different temperatures and photometric variability amplitudes. Finally, we fit stellar evolutionary models to the sample to investigate the links between stellar age, structure, rotation, and magnetism.

4.1 Data and Sample Selection

For the period search, we targeted stars cool enough to maintain surface convection zones and dynamos capable of producing surface spots. We avoided giant stars, which slow substantially as they evolve onto the giant branch and their envelopes inflate (Ceillier et al. 2017). We selected relatively bright, cool dwarf and subgiant stars in the TESS Southern

Continuous Viewing Zone (SCVZ), a 450 square degree field centered around the southern ecliptic pole. TESS observed the SCVZ continuously for 350 days, taking full-frame images (FFIs) every 30 minutes. The long baseline ensures sufficient coverage for the most slowly-rotating stars we might hope to detect. For example, an M-dwarf rotating once every 100 days will make 3.5 rotations under observation in the CVZs. An old K-dwarf rotating at 45 days will rotate nearly 8 times, and a G-dwarf at 30 days will rotate more than 10.

We selected stars from the TESS Input Catalog (TIC, Stassun et al. 2019) with $T_{\text{eff}} \leq 10,000$ K, TESS magnitude ≤ 15, and ecliptic latitude $\leq -78^{\circ}$ to target the SCVZ. There are 398,977 such stars in the TIC. There are several publicly available light curve sets, pipelines, and tools designed and optimized for TESS data, some of which we list in Table 4.1. Tools like `Lightkurve` (Lightkurve Collaboration et al. 2018) and `eleanor` (Feinstein et al. 2019) are general tools to download, process, and analyze TESS data. `eleanor` is optimized for exoplanet detection, so its default light curve processing is aggressive and can remove the stellar signals we are interested in. `Unpopular` (Hattori et al. 2022) is a light curve processing pipeline optimized for systematics removal while preserving multi-sector astrophysical signals. It may be ideal for the problem of rotation, but it requires downloading large FFI cutouts, or the entire set of FFIs, for it to work optimally. `Lightkurve`, on the other hand, does no automatic processing and provides simple tools for downloading and interacting with image and light curve data. We use `Lightkurve` for all our photometry and light curve processing.

Among the many public light curve datasets, the TESS Quick-Look Pipeline (QLP, e.g., Huang et al. 2020a) and DIAmante (Montalto et al. 2020) are designed for planet searches, so they share the problem of aggressive processing with `eleanor`. The difference imaging analysis (DIA) light curves of Oelkers & Stassun (2018) are for general use, but only sectors 1–5 of the first year are available. The GSFC-ELEANOR-LITE light curves (Powell et al. 2022) are a brand new data set using `eleanor` to create general-use light curves for all TESS stars brighter than 16th magnitude in the TESS band pass. They will be worth considering for large scale investigations in TESS, but currently only two sectors are publicly available. The TESS Science Processing Operations Center (TESS-SPOC, Caldwell et al. 2020) has FFI light curves for nearly 40,000 bright SCVZ targets, with background subtraction and systematics correction, as well as underlying pixel data and apertures, available. They are suitable for general use including rotation, and they are easily downloaded from MAST. Finally, the TESS Asteroseismic Science Operations Center (TASOC, e.g., Handberg et al. 2021) is producing data products for all targets brighter than 15th TESS magnitude. They provide two different light curve products optimized for signals at different timescales with varying levels of processing.

Due to the data availability, relatively low levels of processing, and availability of pixel data and apertures, we determined the TESS-SPOC and TASOC data to be the best available for a rotation search at the time of writing. Their pipelines feature different target and aperture selections, providing two slightly overlapping stellar samples so that we can maximize the number of rotation periods while testing for robustness of periods against the pipelines' different apertures. We outline the pipelines' key differences in the next two sections, but we emphasize that we take a hybrid approach adopting the pipeline apertures and performing custom systematics corrections.

The available pipelines perform aperture photometry and background corrections which can remove stellar astrophysical signals (Hattori et al. 2022). To combat this, we downloaded target pixel files (TPFs) and computed custom aperture photometry, which we describe in Section 4.1.3, using the respective pipeline apertures. The TPFs have undergone cosmic ray rejection and basic dark, flat, and bias correction, but no background subtraction or systematics correction. We refer to the two samples as "TESS-SPOC" and "TASOC" to reference the source of the apertures we used, but we emphasize that these are different

Table 4.1: TESS Full Frame Image Light Curves, Pipelines, and Tools

Name	Reference(s)	Science Use
`Lightkurve`	Lightkurve Collaboration et al. (2018)	general
`eleanor`	Feinstein et al. (2019)	exoplanet detection
`Unpopular`	Hattori et al. (2022)	general
DIA	Oelkers & Stassun (2018)	general
QLP	Huang et al. (2020a,b); Kunimoto et al. (2021)	exoplanet detection
TESS-SPOC	Caldwell et al. (2020)	general
DIAmante	Montalto et al. (2020)	exoplanet detection
T'DA/TASOC	Handberg et al. (2021); Lund et al. (2021)	asteroseismology
GSFC-ELEANOR-LITE	Powell et al. (2022)	general

Note. Software tools are listed first, followed by public light curve data sets. Tools and data sets used in this work are highlighted in blue. All light curve data sets are documented and publicly available as MAST High Level Science Products at `https://archive.stsci.edu/hlsp`, except for DIA (Oelkers & Stassun 2018), which is available at `https://filtergraph.com/tess_ffi`.

products from the officially released data under the same names. We also emphasize that the underlying TPF data are the same between the two samples; the only difference between the computed light curves is the photometric apertures used.

Aperture selection matters most at the faint end. For bright or isolated faint targets, most automated aperture selections will choose roughly the same, correct set of pixels. Faint or crowded targets prove more difficult. For example, `lightkurve`'s default aperture selection uses all pixels (1) $N\sigma$ brighter than the median TPF flux, where N is user-specified, (2) contiguous with the center pixel (or specified target pixel if not the center). This can result in gerrymandered apertures that sometimes do not include the actual target pixels, so a more mature aperture selection is necessary. Both the SPOC and TASOC pipelines have robust, reliable aperture selection algorithms, so the difference between them should be minimal. We will check this by comparing period predictions from the overlapping sample.

4.1.1 TESS-SPOC

The SPOC pipeline (Jenkins et al. 2016) was initially used to calibrate the TESS FFIs and generate TPFs and light curves for all two-minute cadence targets. Caldwell et al. (2020) more recently used the SPOC pipeline to create TPFs and light curves for FFI targets, providing the TESS-SPOC light curves on MAST[1].

A maximum of ten thousand targets per CCD were selected from the TIC for a maximum of 40,000 stars in the SCVZ. For each CCD, the selection order was (1) all two-minute cadence targets; (2) potentially high-value planet host candidates with H magnitude ≤ 10 or distance ≤ 100 pc, flux contamination $\leq 50\%$, and TESS magnitude $Tmag \leq 16$; (3) field star targets brighter than $Tmag \leq 13.5$, log surface gravity ≥ 3.5 (CGS units), and flux contamination $\leq 20\%$. The depth $Tmag \leq 13.5$ was chosen to ensure sufficient signal-to-noise. We estimated the 6-hour combined differential photometric precision (CDPP) of TESS-SPOC FFI light curves to be about 4,000 ppm at $Tmag = 13.5$. At this faint limit, a 5σ detection should vary at the 2% level. About 0.3% of *Kepler* rotators varied at this level (Santos et al. 2019, 2021).

The base level SPOC calibration, which our light curves include, involves traditional CCD bias, dark, and flat field corrections, cosmic ray removal, corrections for variations in pixel sensitivity, and removal of smear signals resulting from the cameras' lack of shutters. Photometric apertures are computed using the same module used for *Kepler*. Briefly, the module uses a synthetic FFI produced from the input catalog and the real pixel response function to compute the optimal aperture for each target. Caldwell et al. (2020) detail the full FFI target selection, Jenkins et al. (2016) describe the SPOC pipeline, and Smith et al. (2016) outline the aperture selection. The TESS-SPOC pipeline has processed FFI data,

---

[1] TESS-SPOC light curves are available at `https://archive.stsci.edu/hlsp/tess-spoc`

producing TPFs and light curves, for all sectors in year 1. We queried all TPFs available for our sample, yielding time-series images for 38,215 targets.

4.1.2 TASOC

The TASOC group within the TESS Asteroseismic Science Consortium (TASC) processes TESS data for all stars brighter than TESS magnitude ≤ 15 for use in asteroseismology (Handberg et al. 2021; Lund et al. 2021). To date, only sectors 1-6 from the first year have been processed, yielding time-series FFI photometry with a 160-day baseline and 30-minute cadence. While there are fewer sectors of data available from TASOC, limiting us to shorter rotation periods than TESS-SPOC, the fainter magnitude limit and lack of number cap (i.e., TESS-SPOC processed not more than 10,000 stars per detector, but TASOC has no such limit) make the TASOC sample complementary to the TESS-SPOC sample. However, the TASOC time series pixel data are not currently available—only the light curves and target apertures are retrievable. To compute light curves, we downloaded the TASOC apertures and applied them to TPFs created using `TESScut` (Brasseur et al. 2019). The `TESScut` TPFs are cutouts from SPOC-calibrated FFIs, so they have undergone the same calibration (dark, bias, flat, cosmic rays, and smear corrections) as the TESS-SPOC data. The only differences in the light curve samples, then, are the stellar sample selection and photometric apertures used.

The TASOC pipeline was run on all TIC targets brighter than $Tmag \leq 15$. Aperture selection is fully described by Handberg et al. (2021), but uses the clustering algorithm DBSCAN (Ester et al. 1996) to find clusters of pixels associated with TIC targets. The watershed image segmentation routine from `scikit-image` (van der Walt et al. 2014) is then used to segment apertures containing more than one target. In general, the apertures created by the TASOC pipeline are larger than those created by TESS-SPOC, resulting in light curves with higher photometric precision. We estimated the TASOC light curves to have 6-hour CDPP of 3,000 ppm at $Tmag = 13.5$. A 5σ detection at this magnitude will vary at the 1.5% level. In *Kepler*, about 0.8% of rotating stars varied at this level (Santos et al. 2019, 2021).

Only the first three sectors of TASOC light curves and apertures are available on MAST[2]; as TASC members we obtained data directly from the consortium database. To obtain the likeliest targets for detecting rotation, we queried data for TIC dwarf stars cooler than 5,000 K, yielding FFI cutouts for 29,609 targets spanning the first 6 sectors of the TESS mission.

4.1.3 Aperture Photometry and Wavelet Transform

Both the TESS-SPOC and TASOC pipelines perform background subtraction and light curve systematics correction. For stellar signals on the same or longer timescales as TESS systematics, these corrections can have the unintended consequence of removing or attenuating the stellar signals (Hattori et al. 2022). We would rather preserve the stellar signals at the expense of some leftover systematics, since neural networks can learn the systematics and regress periods in spite of them. To mitigate the removal of stellar rotation signal, we performed custom photometry using the apertures supplied by the pipelines. For each available TPF, we computed light curves as follows:

1. reject cadences with bad quality flags, which are usually associated with cosmic rays, data downlinks, or angular momentum dumps
2. obtain the post-calibration, pre-background-subtracted image
3. compute the raw light curve using simple aperture photometry and adding all pixels within the aperture

---

[2] TASOC data are increasingly available at `https://archive.stsci.edu/hlsp/tasoc`

4. remove the first three principal components of the time series using `lightkurve.RegressionCorrector`
5. clip 5σ outliers from light curve.

Although neural networks can perform regression in spite of systematics to some extent, *some* systematics removal is necessary. Figure 4.1 shows the Morlet wavelet transform of a TESS-SPOC FFI light curve with no systematics correction. The light curve is dominated by 13.7-day systematics from scattered light, and the wavelet decomposition is completely saturated. We sought to perform as minimal systematics correction as possible in order to preserve the underlying stellar signals. Removing the first three principal components corrected the largest TESS systematics—Earthshine and angular momentum dumps—while leaving smaller systematics and stellar signals mostly intact. We determined the optimal number n_{pca} of principal components to remove by removing 1, 2, 3, 4, and 5 components from a set of 10 light curves, then visually inspecting the resulting light curves to determine for what value of n_{pca} the largest systematics were removed. Meanwhile, removing 5σ outliers cleaned the light curves from systematic jumps and stellar flares. Next we then median-divided the light curves for each target and stitched them together, linearly interpolating to fill any gaps. Finally, we computed Morlet wavelet transforms as detailed in Section 2.3 and binned them to 64×64 pixels to be used as input to the convolutional neural network.

4.1.4 APOGEE Spectroscopy

While the TESS Input Catalog has metallicities and surface gravities for all the stars in our sample, the sources are a heterogeneous combination of photometry and spectroscopy, observations and models. Furthermore, the TIC has no information on detailed abundances, which are useful when investigating changing galactic chemistry with time, and which may

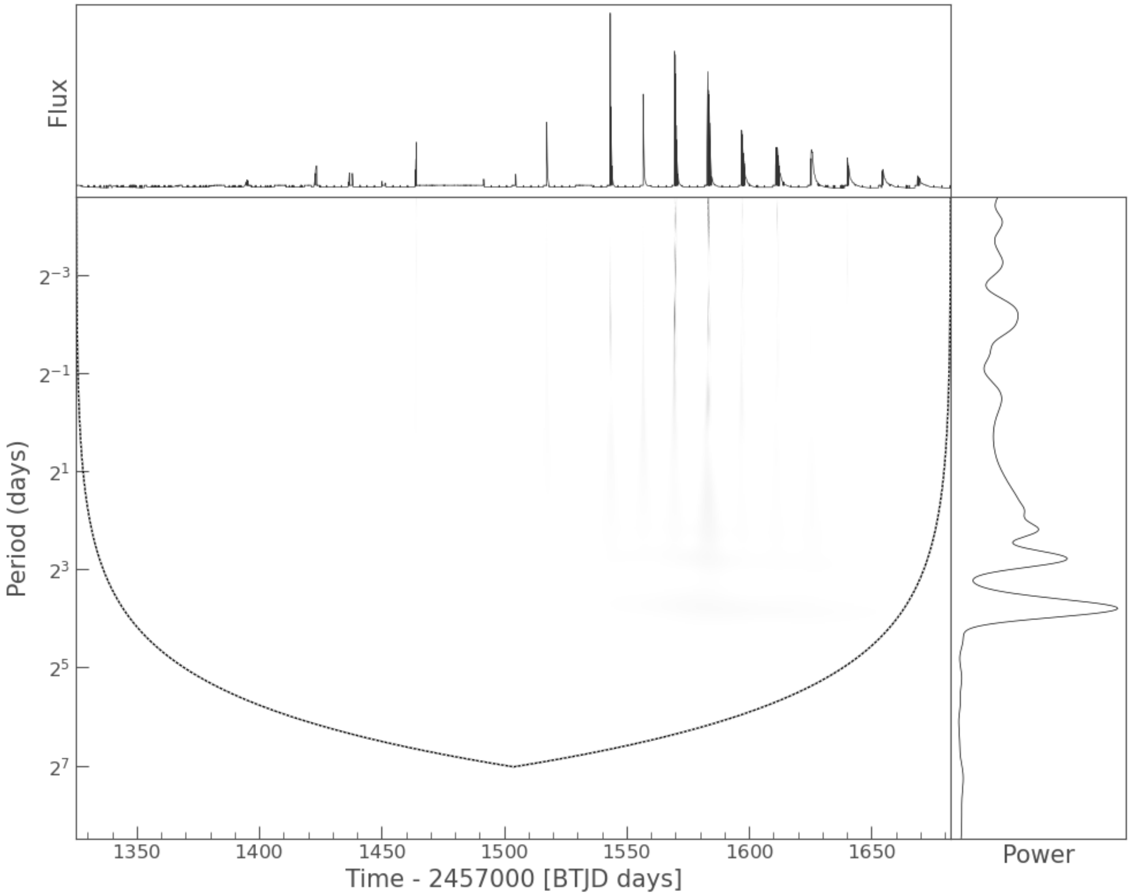

Figure 4.1: The Morlet wavelet transform of a TESS-SPOC light curve with no systematics correction. The top panel shows the light curve, which is overwhelmed by the scattered light systematics every 13.7 days. The bottom panels, showing the full time-frequency wavelet decomposition (left) and the global wavelet power spectrum (right) illustrate that the wavelet transform is completely saturated by the systematics with no corrections.

be important to the connection between rotation and magnetism. We therefore supplement TESS photometric rotation periods with spectroscopic parameters from the Apache Point Observatory Galactic Evolution Experiment (Majewski et al. 2017, APOGEE). APOGEE collects high-resolution ($R \sim 22,500$), near-infrared (1.51–1.70 μm) spectra and provides model-dependent estimates of effective temperature, surface gravity, metallicity, and detailed abundances for hundreds of thousands of stars across the entire sky. The TESS/APOGEE survey within APOGEE-2S (section 5.8 of Santana et al. 2021) targeted

38,000 stars in the TESS SCVZ with 2MASS color and magnitude ranges $7 < H < 11$ and $J - K > 0.3$, and about 9,000 other SCVZ stars were observed for other programs. We cross-matched our TIC targets with APOGEE Data Release 17 (Abdurro'uf et al. 2022) to obtain spectroscopic parameters for 47,142 stars in our sample. Of those stars, 16,545 have TESS-SPOC data products, and 3,156 have data products in our TASOC subsample. These combine to yield 17,796 unique targets with APOGEE spectroscopy and either TESS-SPOC or TASOC target pixel files.

4.2 Deep Learning Framework

To predict rotation periods from TESS light curves, we applied the method outlined in Chapter 2 (Claytor et al. 2022) with a few modifications. Namely, we generated new training sets tailored to both the TESS-SPOC and TASOC samples (mostly to represent the different light curve lengths), and we optimized different neural networks for each data set.

4.2.1 Training Set

In Claytor et al. (2022) we trained a convolutional neural network on a set of synthetic light curves made from physically realistic spot evolution simulations, combined with real TESS noise from SCVZ galaxy light curves. Two weaknesses of our approach was that (1) we were not successful in recovering periods of less than 10 days from our held-out test set, and (2) the neural network overfit within a few (of order 10) iterations over the training set.

The first was due to the choice of a loss function that enabled the network to predict period uncertainty. In the presence of uncertainty, predicted periods are biased toward the mean of the distribution and away from the upper and lower limits. The effect is most pronounced for the top and bottom 10% of the training set period range, affecting the ranges from 0–18 days and 162–180 days. Since the ability to predict period uncertainty is a key strength of our approach, we worked around this problem by using multiple training sets with different period ranges. We created four separate training sets with periods ranging from 0.1 day to 30, 60, 90, and 180 days. Having a shorter upper limit such as 30 days allows us to more successfully probe the short-period range—here only 0–3 days and 27–30 days are severely affected—while having multiple training sets with increasing upper limits gives us multiple period predictions that we can mutually compare for extra tests of reliability. The distributions of all simulation input parameters besides period were the same as in Claytor et al. (2022) (the simulations for the 180 day upper limit *are* the same as in the previous work), and the same simulations were used for both the TESS-SPOC and TASOC training sets. The only other difference was the source of the light curves combined with the simulations to emulate instrumental noise.

The second shortcoming was simply due to the small number ($\sim 2,000$) of galaxy light curve examples. If there are too few examples of noise in the training set, the neural network learns the noise quickly and overfits the data. Since there are many more bright stars than galaxies in TESS, we addressed this by combining our simulations with light curves of stars in temperature ranges that should be quiescent to emulate TESS noise. McQuillan et al. (2014) detected periods in *Kepler* stars hotter than the Sun half as often as in cooler stars. Given TESS's slightly worse photometric precision and redder pass band than *Kepler*, we expect TESS stars hotter than the sun to be even harder to detect in rotation. This makes stars in the temperature range above $\sim 5,800$ K ideal for use as quiescent light curve sources. At first we queried TPFs and computed light curves for TASOC stars in the range 5,800 K $\leq T_{\text{eff}} \leq$ 6,000 K. We kept light curves with at least 4 sectors to allow for gaps in the data while ensuring that there were data for more than half the time baseline. This yielded a set of 23,332 TASOC noise templates, an order of magnitude more than the number of galaxy sources used in the previous exercise. The same range of temperatures

Table 4.2: Details of TESS-SPOC and TASOC Noise Light Curves

	TESS-SPOC	TASOC
Sectors included	1–13	1–6
Minimum number of sectors	7	4
Time baseline (days)	350	160
T_{eff} range of sources (K)	6,000–7,000	5,800–6,000
Number of sources	17,637	23,332

in TESS-SPOC, requiring that light curves have at least 7 sectors to cover more than half of the time baseline, has only 6,000 targets, so a larger temperature range was required. We used the range 6,000 K $\leq T_{\text{eff}} \leq$ 7,000 K, which contained 17,637 sources. Table 4.2 details the noise light curves samples that make up the TESS-SPOC and TASOC training sets.

4.2.2 Convolutional Neural Network

We began with the same CNN as in Claytor et al. (2022), but we experimented with slightly different architectures to optimize different networks to the TESS-SPOC and TASOC training sets. The original architecture (outlined in Table 2.2) had three convolution layers with (A) 8, 16, and 32 kernels, respectively, but we also tried (B) 16, 32, and 64 kernels; (C) 32, 64, and 128; and (D) 64, 128, and 256. More kernels or filters per layer allow the network to learn more features if they are present in the data, but they may also cause the network to overfit the data faster. We trained each architecture individually on each training set and chose the architecture with the best overall recovery on a held-out validation sample. For the TESS-SPOC set, architecture C performed best overall, but architecture A was optimal for the TASOC set. We discuss the details of architecture optimization in Appendix B.

4.3 Rotational Modeling

With newly obtained TESS rotation periods, we will be able to look for trends of rotation detectability and variability across fundamental stellar parameters. Stars spin down and become less active as they age (Skumanich 1972), so we expect both detectability and variability to decrease with age. We also know activity to vary with Rossby number, the ratio of rotation period to the convective overturn timescale (e.g., Wright et al. 2011). To validate these relationships and look for potential departures from expected behavior in TESS, we will need to derive ages and Rossby numbers for our sample.

While the abundant ground- and space-based data provide countless observational windows into the nature of stars, there are still fundamental quantities that we cannot easily measure for single stars but must infer from stellar evolution models. Such parameters include age, mass, and convective depth and timescale (and therefore Rossby number). We therefore employ the stellar evolution and rotational modeling using `kiauhoku` (Chapter 3 and Claytor et al. 2020) to infer these fundamental parameters for our stars with rotation periods and APOGEE spectroscopy.

The models were generated using the non-rotating version of the Yale Rotating Stellar Evolution Code (YREC, Demarque et al. 2008), then angular momentum evolution was applied post-hoc following the magnetic braking law of van Saders et al. (2016). The models are fully described in Chapter 3 (Claytor et al. 2020), but we list the input physics and solar calibration here in Table 4.3. The angular momentum evolution includes weakened magnetic braking beginning about halfway through the main sequence (van Saders et al. 2016), but does not include core-envelope decoupling (Spada & Lanzafame 2020) or the apparent stalling of spin-down that may occur in young, cool stars (Curtis et al. 2019).

Table 4.3: Summary of Input Physics to Stellar Evolution Models

Parameter	Value/Source
Atmosphere	Castelli & Kurucz (2004)
Convective overshoot	False
Diffusion	False
Equation of state	OPAL (Rogers & Nayfonov 2002)
High-temperature opacities	OP (Mendoza et al. 2007)
Low-temperature opacities	Ferguson et al. (2005)
Mixing length α	1.86
Mixture and solar Z/X	Grevesse & Sauval (1998)
Nuclear reaction rates	Adelberger et al. (2011)
Solar X	0.7089
Solar Y	0.2728
Solar Z	0.0183
$\Delta Y/\Delta Z$	1.4
Surface $(Z/X)_\odot$	0.02289
Angular momentum evolution	van Saders et al. (2016)
Initial rotation period	8.134 d
Critical Rossby number	2.16
Critical ω for saturation	3.394×10^{-5} s^{-1}
f_k	6.575
Disk coupling timescale	0.281 Myr

Using the Markov-chain Monte Carlo (MCMC) tools in `kiauhoku`, we interpolated and fit stellar evolution models to observational data. For the MCMC we used a χ^2 log-likelihood of the form

$$\mathcal{L} = -\frac{1}{2}\sum_i \frac{(x_i - x_i')^2}{\sigma_{x_i}^2},$$

where x_i and σ_{x_i} are the observational input parameters and uncertainties, respectively, x_i' is the computed value from the model, and i iterates over the input parameters.

We performed two MCMC runs with slightly different input parameters. For the first run, we used APOGEE temperature, metallicity, and α-element abundance, our CNN-predicted rotation period, and luminosity from the TIC (Stassun et al. 2019). For the cases where no luminosity was available, we instead used APOGEE surface gravity. We used the chains from this run to infer ages, masses, and all other fundamental parameters besides the convective overturn timescale ($\tau_{\rm cz}$). Because $\tau_{\rm cz}$ is determined entirely by H-R diagram position (in our models it depends only on convective zone properties, not on rotation), our second MCMC run did not include rotation period so $\tau_{\rm cz}$ would not be biased in the few instances when the period and luminosity (or surface gravity) were not mutually consistent. The likelihood in the second run was otherwise identical to that of the first. The convective overturn timescale is the only inferred parameter we use from the second run; all other quantities are from the first.

4.4 Rotation Periods of TESS Stars

We predicted periods for TESS-SPOC targets with at least 7 sectors and TASOC targets with at least 4 sectors, the same as for the training light curves. To determine reliability we followed the method of Claytor et al. (2022) and used a cut in fractional predicted uncertainty to denote reliability. We do not treat the predicted σ_P as a formal uncertainty (see Section 2.4 for a discussion of the loss function and predicted parameters). Rather, the quantity σ_P/P serves as a metric of relative credibility of period predictions. $\sigma_P/P \leq 35\%$ translated to $\sim$10% median percent error in the training set recovery, so we adopt this predicted uncertainty cut as our baseline for reliability. Since there are four neural networks, each with its own period range, we obtained four sets of period candidates for both the TESS-SPOC and TASOC data sets. If two or more neural networks yielded predictions passing our reliability cut for the same star, we averaged the predictions and added their standard deviation in quadrature to the predicted uncertainty. If the newly combined fractional uncertainty was larger than 35%, we discarded the star. Following this procedure, we obtained 5,272 TESS-SPOC stars with reliable periods and 5,023 reliable TASOC periods. These combine for a total of 9,837 unique targets, 458 of which overlap between the two samples. Figure 4.2 shows a small selection of light curves for which we obtained periods. The periods are plotted against TIC effective temperature in Figure 4.3 to illustrate, for the first time, the distribution of main sequence stellar rotation periods longer than 13 days in TESS.

4.4.1 Features of the Period Distribution: Biases

Since the TESS-SPOC sample spans a wider range in temperature than our TASOC sample, we will focus our main discussion of the period distribution on the TESS-SPOC sample. In this period distribution there are two apparent edges worth noting. First, there is temperature edge at 6,000 K. The underlying sample distribution has no such edge, so it must be produced by the period search. 6,000 K is the lower bound of the noise source sample used for the TESS-SPOC training set, so above this temperature there is some overlap between the training light curves and the "real" data. It is possible that inclusion in the training set as a noise template (multiple instances with varying injected simulated rotation signals) confuses the neural network and causes it to assign a large uncertainty to these targets. Another possibility is that spot modulation amplitudes drop above 6,000 K, where the convective envelope disappears and stars become less active. However, since activity scales with Rossby number $Ro = P_{\rm rot}/\tau_{\rm cz}$, where the convective timescale scales monotonically with temperature, we expect a hot star detection edge to be curved rather than vertical. We therefore favor the former explanation for this feature.

The other edge is in rotation period and occurs at roughly 27 days. While slow rotators tend to be less active than fast rotators at fixed temperature, the spot modulation amplitudes at which we expect to lose detections vary in period across temperature. In other words, a period detection edge produced by astrophysical variability should not be flat. Rather, the 27-day detection edge is likely related to the 27-day sector length in TESS. Without a

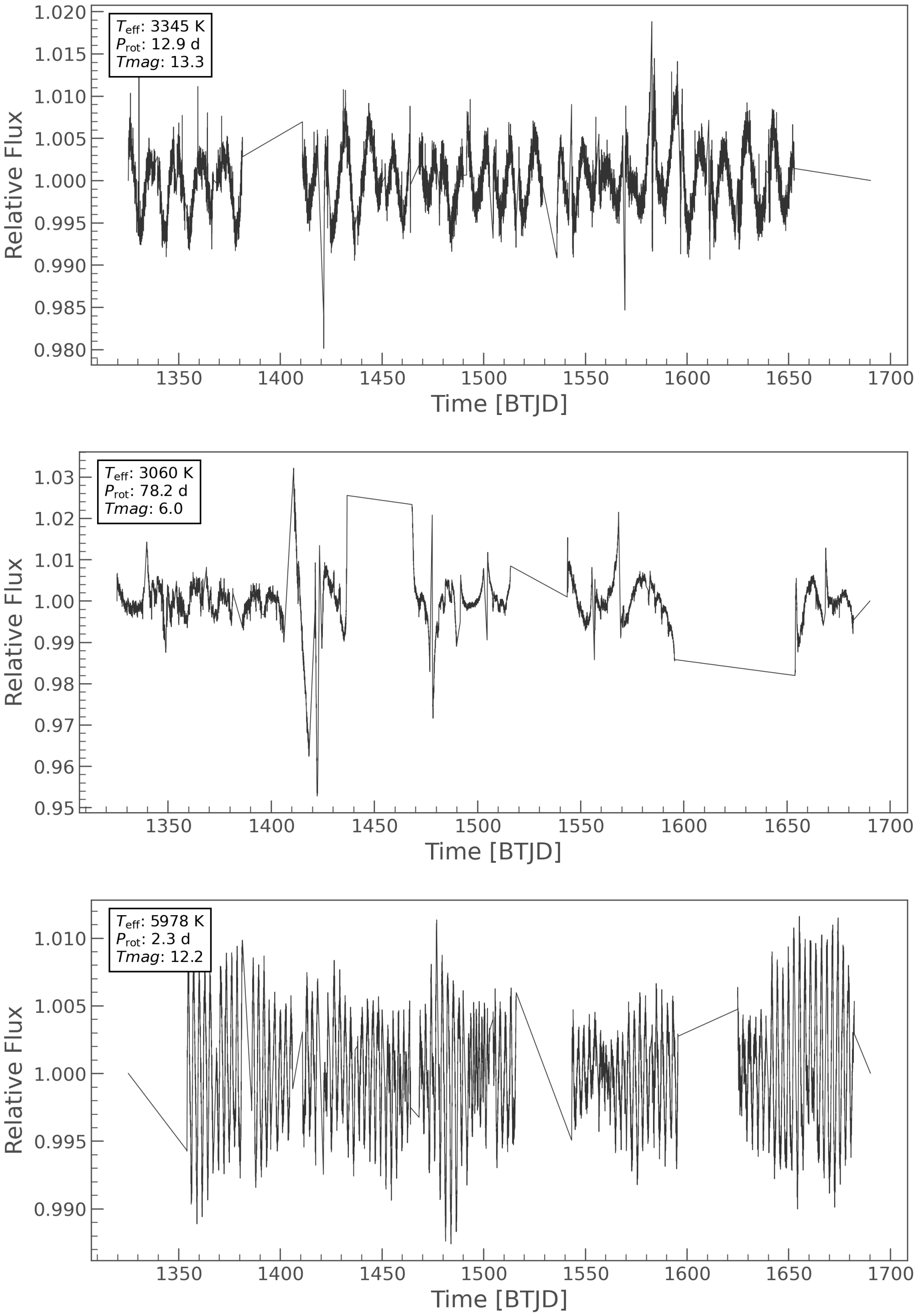

Figure 4.2: A selection of light curves for which we successfully estimated rotation periods using the neural network. *Top*: an M dwarf with strong, coherent spot modulation. *Middle*: a slowly-rotating M dwarf with several missing sectors. *Bottom*: a rapidly rotating G dwarf.

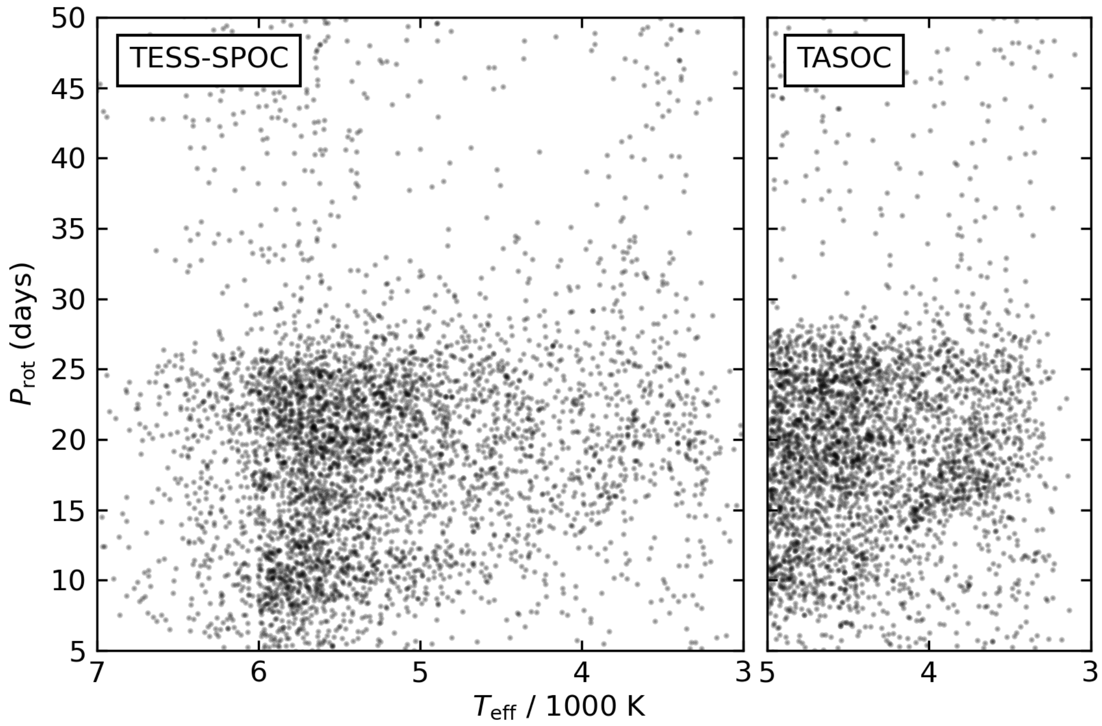

Figure 4.3: Period–temperature distribution for the TESS-SPOC (left) and TASOC (right) samples.

reliable absolute flux calibration in each sector, stitching sector light curves together can destroy coherent signals longer than 27 days in period. While we include sector-to-sector stitching in all our training sets, the 27-day edge suggests that the training sets do not fully capture the sector effects in TESS, or at the very least the sector effects make period predictions much less certain beyond 27 days.

4.4.2 Features of the Period Distribution: Populations

The period–temperature distribution displays a sloped, short-period edge, similar to what was seen in *Kepler* (McQuillan et al. 2014; Santos et al. 2019, 2021). This edge represents the point at which field stars converge onto the slowly-rotating sequence (Curtis et al. 2020).

The distribution also displays a gap in rotation period, occurring at roughly 12 days at 5,000 K and increasing to 20 days at 4,000 K. McQuillan et al. (2013) first identified this

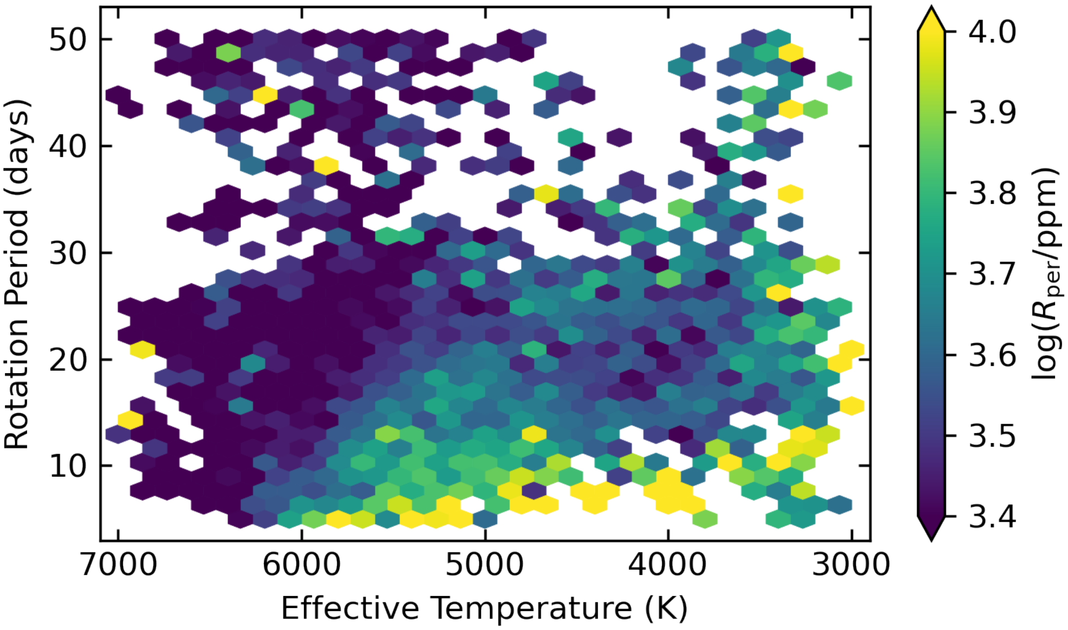

Figure 4.4: Hexbin plot of the TESS rotation period distribution versus TIC temperature, with bins colored by average photometric variability range R_{per}. As expected, amplitudes generally decrease with increasing period at fixed temperature. Interestingly, the amplitudes near the rotation gap are smaller than those away from the gap in the same temperature and period ranges, in agreement with Reinhold et al. (2019); Reinhold & Hekker (2020). The bins above a temperature of 5,000 K and above a period of 30 days nearly all have only a single star; this region is sparsely populated and most stars here are likely spurious detections.

gap in the *Kepler* field, and it has also been recovered in other field star samples using K2 (Reinhold & Hekker 2020; Gordon et al. 2021). We present here the first recovery of the rotation period gap using TESS.

We computed the photometric variability range R_{per} for all the stars with predicted periods. Like McQuillan et al. (2014), to compute R_{per} we measured the interval between the 5th and 95th percentile of normalized flux in each period bin, then took the median of those values. Figure 4.4 shows another look at the rotation period distribution, now colored by R_{per}. As we expect, stellar variability generally decreases with increasing periods at fixed temperature, since slowly rotating stars are less magnetically active than faster stars.

There is a significant dip in the variability between 3,500 K and 4,500 K, most notably near the location of the rotation period gap, which goes from about (5,000 K, 12 d) and curves upward to (4,000 K, $\sim$20 d) (refer to Figure 4.3). This is consistent with Reinhold et al. (2019); Reinhold & Hekker (2020), who found a similar dip in variability near the period gap in *Kepler* and K2 stars. They argued that the dip in variability causes the apparent gap in rotation periods, where stars in the gap exhibit modulation too small to be detected in rotation. Our recovery of the variability dip lends credit to this hypothesis, but we cannot rule out the core–envelope decoupling scenario of Spada & Lanzafame (2020).

Figure 4.5 shows the TESS-SPOC period–temperature distribution using different $R_{\rm per}$ floor values. Requiring $\log(R_{\rm per}/{\rm ppm}) > 3.5$ removes many stars from the top-left corner of the diagram, which are hot but have apparently long rotation periods. While we do not expect to find many stars in this regime based on Galactic population synthesis (e.g., van Saders et al. 2019), the stars that are here should have low variability because they are hot and therefore have thin-to-nonexistent outer convective envelopes, and because they spin relatively slowly. The stars that are lost from the top panel to the middle panel of Figure 4.5 are likely mostly spurious detections whose measured $R_{\rm per}$ is actually the photometric noise, as well as a handful of correctly measured, low-variability stars. As we continue to increase the $R_{\rm per}$ floor, we see two effects. First, we lose more low-variability stars on the hot, long-period edge. This is precisely what we expect to see in a period sample: raising the variability floor, we should lose the lowest-Rossby number stars first. These are the slowly rotating, hot stars in the top left “corner” of the distribution. Second, the gap becomes more apparent, consistent with Reinhold & Hekker (2020), although it is difficult to determine whether stars are lost from the gap at higher rates than outside the gap.

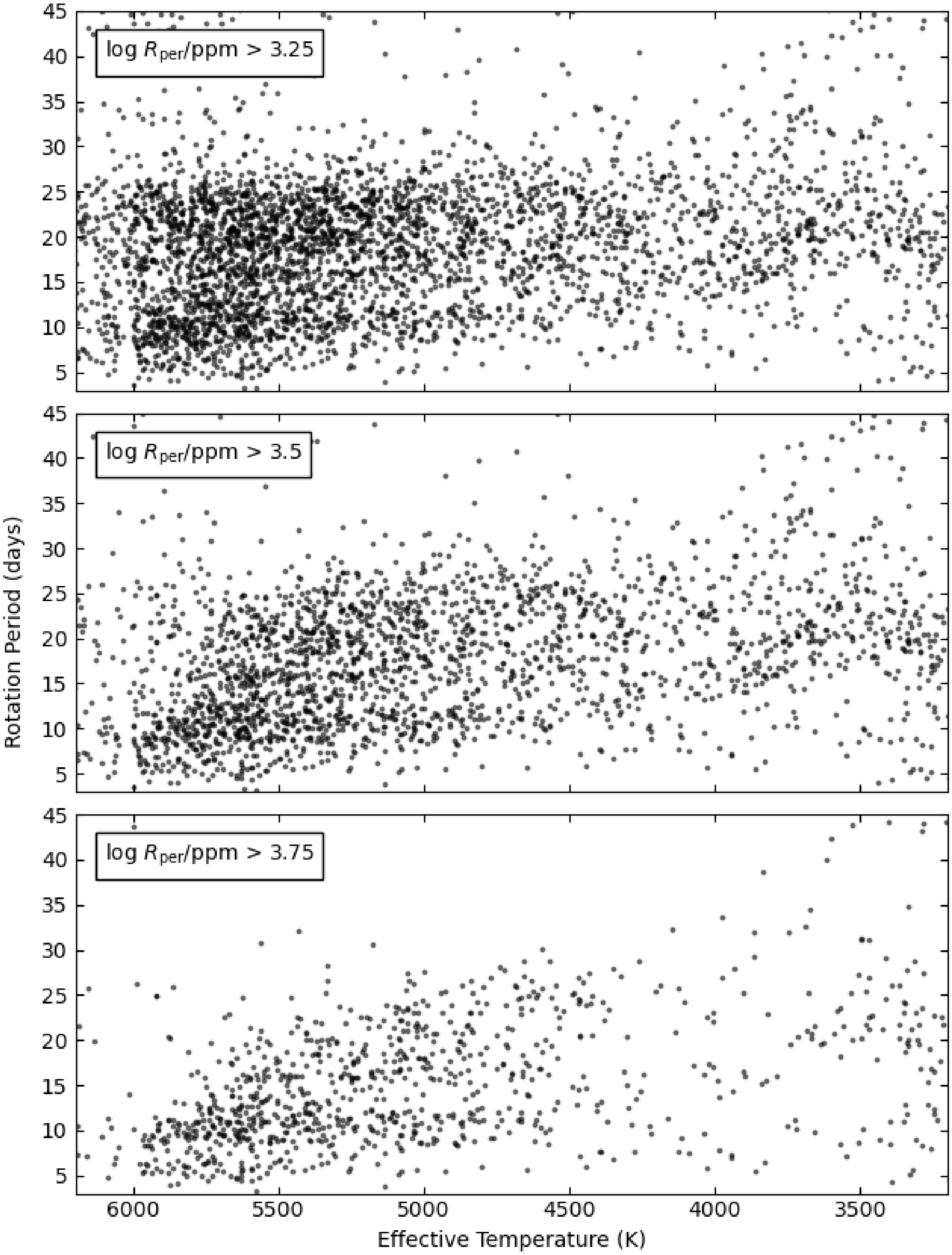

Figure 4.5: Distribution of periods and TIC temperatures for the TESS-SPOC sample, with varying lower bound on photometric variability range $R_{\rm per}$. All stars shown pass our reliability criterion ($\sigma_P/P \leq 35\%$).

4.4.3 Comparison between TESS-SPOC and TASOC

In the TASOC sample (e.g., in the right panel of Figure 4.3), we again see a weak presence of the period gap as well as the sloped short-period edge. the TASOC sample also show the 27-day horizontal detection edge exhibited by the TESS-SPOC sample, resulting from the increase in uncertainty past 27 days from sector-to-sector stitching.

There are 458 stars in common between the TASOC and TESS-SPOC samples. We predicted two periods for each of these stars using different neural networks fit to different training sets tailored to the different light curve lengths. While the underlying pixel data between the two samples were the same, the apertures used to perform photometry were different, and the TESS-SPOC light curves were more than twice as long (13 sectors) as the TASOC light curves (6 sectors). In addition, the two training sets used different underlying samples of stars for noise and systematics. This gives us a sample to compare period predictions for robustness against photometric aperture, training set, and duration of observation.

In Figure 4.6 we compare the period predictions for the overlap sample. The predictions mostly agree, with a median relative error of 7%. The predictions that disagree have relatively large predicted uncertainty, though the fact that they make our 35% reliability cut means that there will be some contamination in our period sample. 76% of stars in the overlap sample have period predictions agreeing to within 20%. The discrepancies likely arise from the different aperture selection, different light curve durations, or differences in the underlying training sets, although here we do not attempt to isolate the main contributor.

4.4.4 Comparison with other large field rotation samples

The TESS rotation period distribution is the product of the underlying distribution of periods, the presence of modulation in the light curve, the availability of data products,

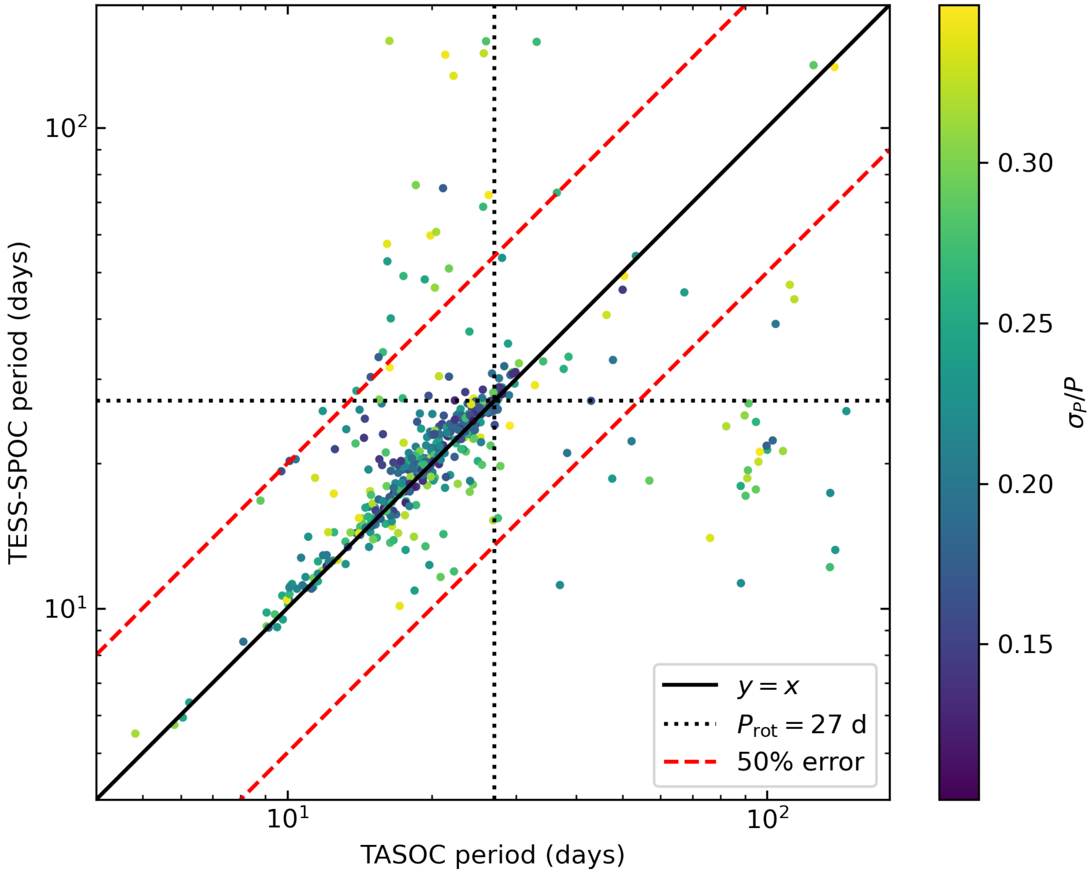

Figure 4.6: Period comparisons for the 458 stars in both the TESS-SPOC and TASOC samples. The solid black line represents perfect agreement, while the dashed red lines are $\pm 50\%$ error. The black dotted lines are at 27 days on either axis, showing the TESS sector length. There is generally good agreement for most stars, with median percent error of 7%, and most of the disagreeing estimates have relatively large predicted uncertainty.

and the ability to detect periods across various stellar parameters. To try and understand the relative influence of these effects, we must compare the TESS period distribution with other large period data sets, particularly *Kepler* and K2. Figure 4.7 shows the period distributions from *Kepler* and K2, while Figure 4.8 shows our newly obtained TESS distribution. We represent temperature bins as vertical histograms in the style of McQuillan et al. (2014) to increase the clarity of the period gap in the cool-temperature regime. The number of

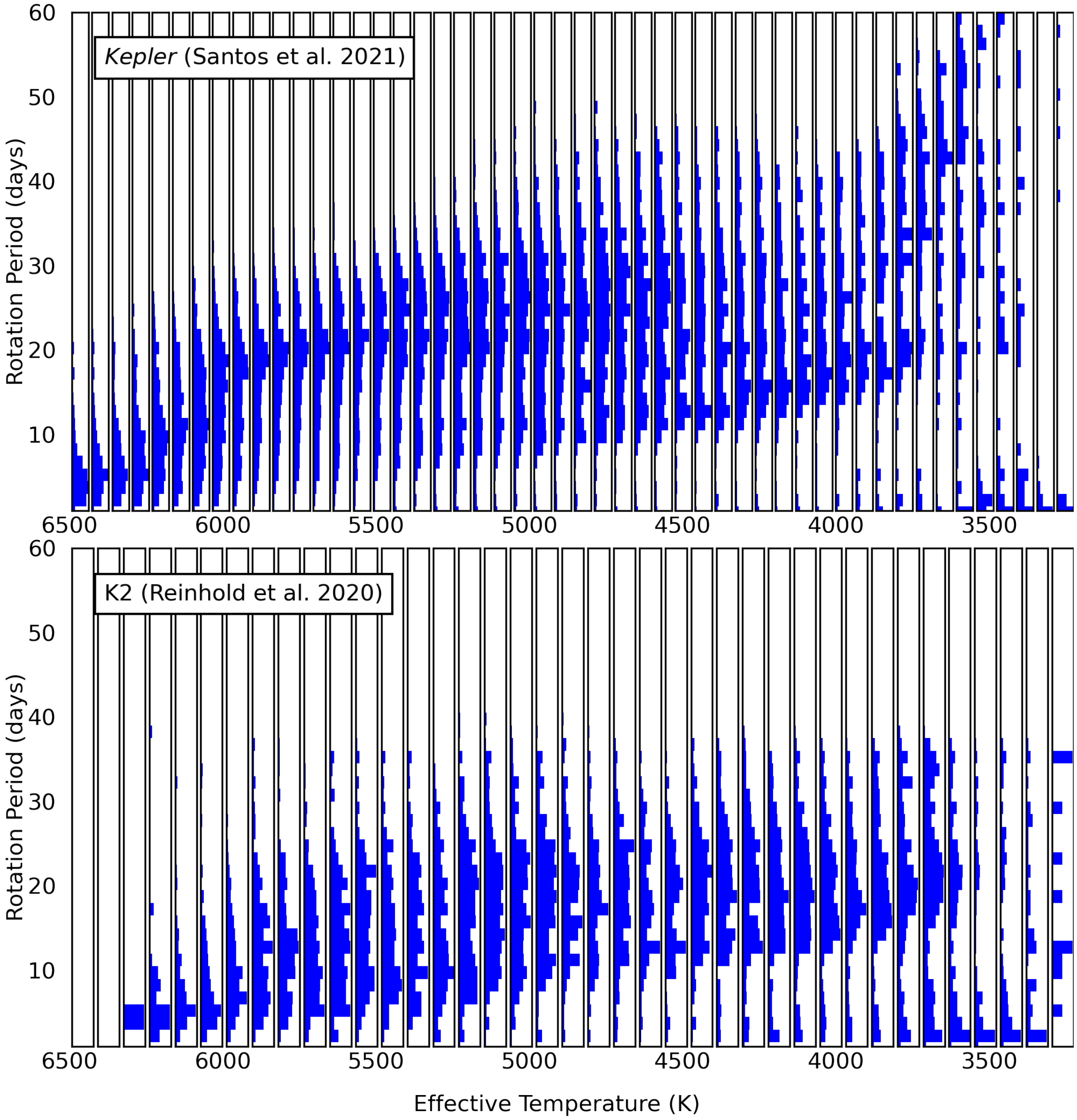

Figure 4.7: Histogram representations for the period–temperature distribution of *Kepler* (Santos et al. 2019, 2021, top) and K2 (Reinhold & Hekker 2020, bottom).

temperature and period bins is adjusted in each panel to account for the total number of stars in each sample.

The top panel of Figure 4.7 displays 52,338 carefully vetted *Kepler* rotation periods from Santos et al. (2021). The *Kepler* period distribution exhibits a pileup on its upper

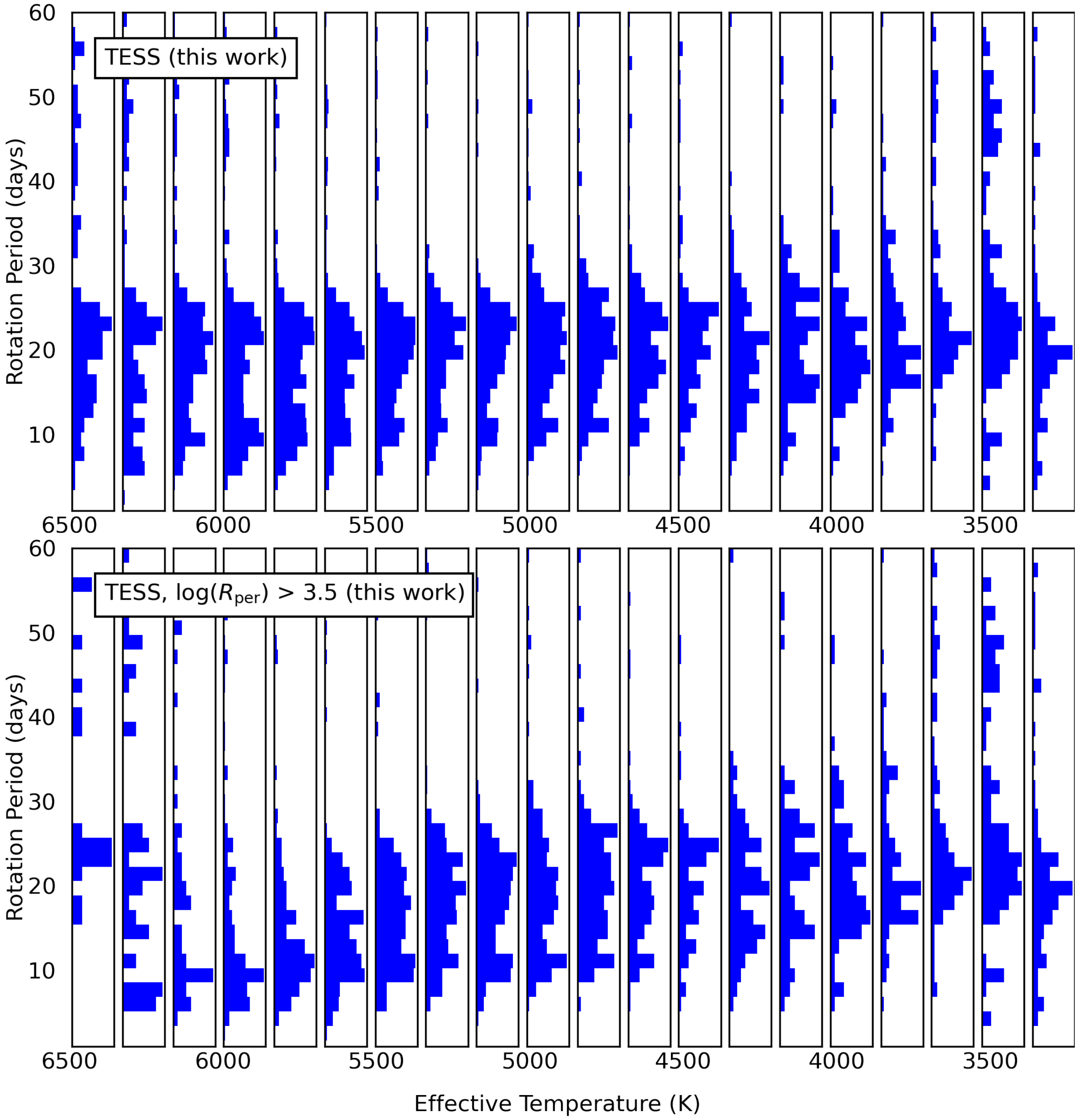

Figure 4.8: Histogram representations for the period–temperature distribution of TESS, with no photometric variability cut (top), and restricting to $\log(R_{\rm per}/{\rm ppm}) > 3.5$ (bottom). Temperatures are from the TIC.

edge for stars hotter than $\sim 5,500$ K, which is a prediction of the weakened magnetic braking hypothesis (van Saders et al. 2016, 2019) and has been well-studied in the *Kepler* field (Hall et al. 2021; Masuda et al. 2022; David et al. 2022). Also present is the rotation period gap, clearly visible at ~ 15 days at 5,000 K, ~ 17 days at 4,500 K, and continuing to increase and widen at cooler temperatures.

The bottom panel of Figure 4.7 shows 13,847 rotation periods from stars in K2 measured by Reinhold & Hekker (2020). These represent a high-fidelity subsample with normalized Lomb-Scargle peak height > 0.5 and variability range $R_{\rm var} > 0.1\%$. Peak heights range from 0 to 1 and quantify how sinusoidal a light curve is, with a perfect sinusoid returning unit peak height, and noisy, non-sinusoidal data returning values close to zero. $R_{\rm var}$ is defined similarly to $R_{\rm per}$ above, except that $R_{\rm var}$ is the variability range over the entire light curve, rather than a median of ranges per period bin. The K2 distribution shows the period gap most strongly between 5,000 K and about 4,250 K, but it is weakly visible in cooler stars, where it appears to increase in period and widen as in *Kepler*. The hot star pileup is not apparent here. This is likely due to the relatively large temperature uncertainty in the K2 Ecliptic Plane Input Catalog (median 140 K, Huber et al. 2016), which blurs out features in the temperature distribution. van Saders et al. (2019) suggested the pileup was absent from the original McQuillan et al. (2014) *Kepler* period distribution for the same reason. Finally, periods longer than about 35 days are largely absent from the K2 distribution because of K2's 80-day observing campaigns in each field.

The TESS distribution in the top panel of Figure 4.8 shows periods for 5,056 TESS-SPOC stars with $\sigma_P/P \leq 35\%$, representing the most credible detections. The period gap is present and is most apparent at temperatures between 4,000 and 5,000 K. It is still visible at temperatures cooler than 4,000 K, but the dearth of reliable detections at periods nearing 30 days makes the gap more difficult to detect. In addition to the gap, we detect a handful of M-dwarfs rotating with periods between 40 and 60 days; similar stars were also observed in the *Kepler* period distribution. We visually inspected the light curves for these stars and confirmed them to be true rotation detections with photometric variability $R_{\rm per}$ approaching 1%. On the hot end, the distribution lacks the pileup seen in *Kepler* because

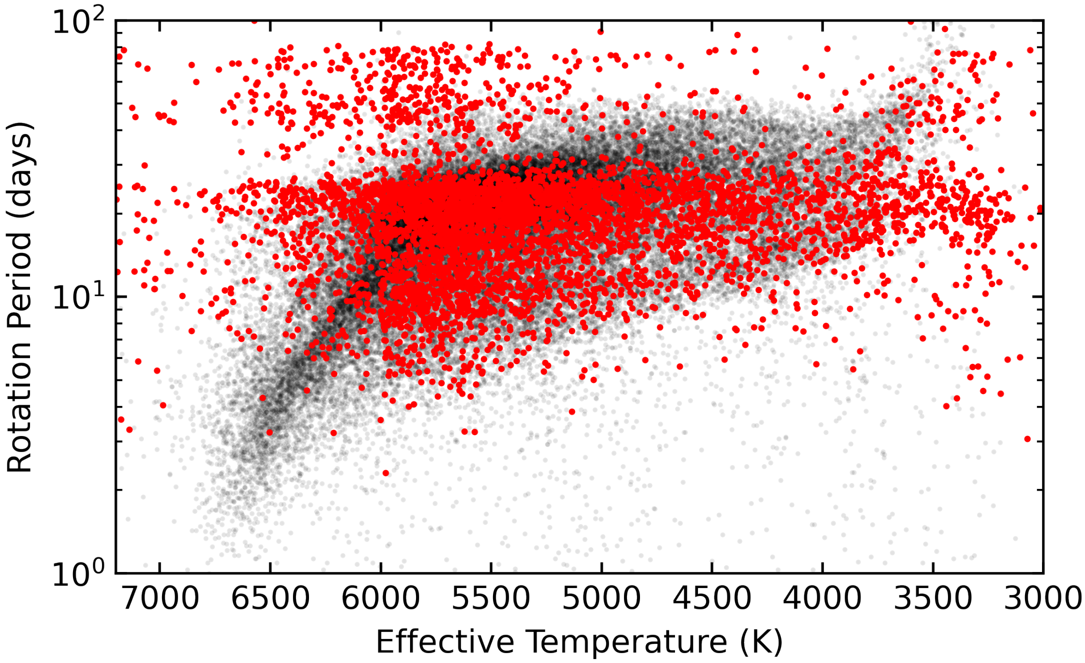

Figure 4.9: The *Kepler* period–temperature distribution from Santos et al. (2019, 2021) (black points) with our new TESS rotation periods overplotted (red points). TESS temperatures are from the TIC.

of the abundance of hot stars apparently rotating with ∼20-day periods. These are likely spurious detections, as their measured amplitudes are close to the noise floor (close to 100 ppm for $Tmag = 8$ and 1% for $Tmag = 15$). When we raise the variability floor in the bottom panel of Figure 4.8, the hot, slow rotators mostly disappear, but the gap and the slowly rotating M-dwarfs remain.

We offer one final view of the TESS period distribution, now plotted over the *Kepler* distribution of Santos et al. (2019, 2021), in Figure 4.9. The short-period edge of the TESS distribution has the same location and slope of *Kepler*'s, suggesting a physical origin for the edge rather than arising from star formation. The rotation period gap agrees as well, following *Kepler*'s for as long as the TESS gap remains visible into the hot stars. TESS appears to see stars in regions *Kepler* does not: the slowly rotating, hot stars ($T_{\rm eff} > 5000$ K and $P_{\rm rot} > 30$ d) have amplitudes close to the noise floor and are likely spurious detections. On the other hand, the slowly rotating M dwarfs, with TESS periods up to 90 days, have been vetted by eye and are mostly real rotation detections. Interestingly, TESS also has some more rapidly rotating M-dwarfs, comparable to those seen by K2 and MEarth (Reinhold & Hekker 2020; Newton et al. 2016, 2018), suggesting the stellar populations that make up the TESS SCVZ are different from those in *Kepler*.

4.4.5 Modeling Results

Taking the stars with reliable periods from either TESS-SPOC or TASOC, we cross matched with APOGEE DR17 spectroscopic parameters estimated with the APOGEE Stellar Parameters and Abundances Pipeline (ASPCAP, García Pérez et al. 2016). To ensure a high quality sample, we removed objects with the ASPCAP STAR_BAD and SNR_BAD flags set. We then filtered out targets with *Gaia* eDR3 Renormalized Unit Weight Error (RUWE) > 1.2 and flux contamination ratio $> 10\%$ to clean the sample of potential binary or nearby flux contaminants. This yielded a sample of 3,400 stars, which we designate as our "gold" sample. We fit models to these stars according to the procedure in Section 4.3, taking the posterior medians as the nominal fit parameters.

The ages for our stars, which are estimated using both TIC luminosities and our TESS rotation periods, are shown in Figure 4.10. We separate stars with rotation periods less than 10 days, which are more likely to be spun-up by close binary companions than be true rapid rotators Simonian et al. (2019). The age distribution peaks at about 3.5 Gyr, which is consistent with the isochrone-derived age distribution of Buder et al. (2019), but inconsistent with our rotationally-derived ages in the *Kepler* field (Claytor et al. 2020), whose distribution peaked closer to 2 Gyr. Berger et al. (2020) used isochrones to derive an age distribution of the *Kepler* stars, which peaked at 2.5 Gyr. There is tentative agreement with the seismic age distribution of *Kepler* stars presented by Silva Aguirre et al. (2018):

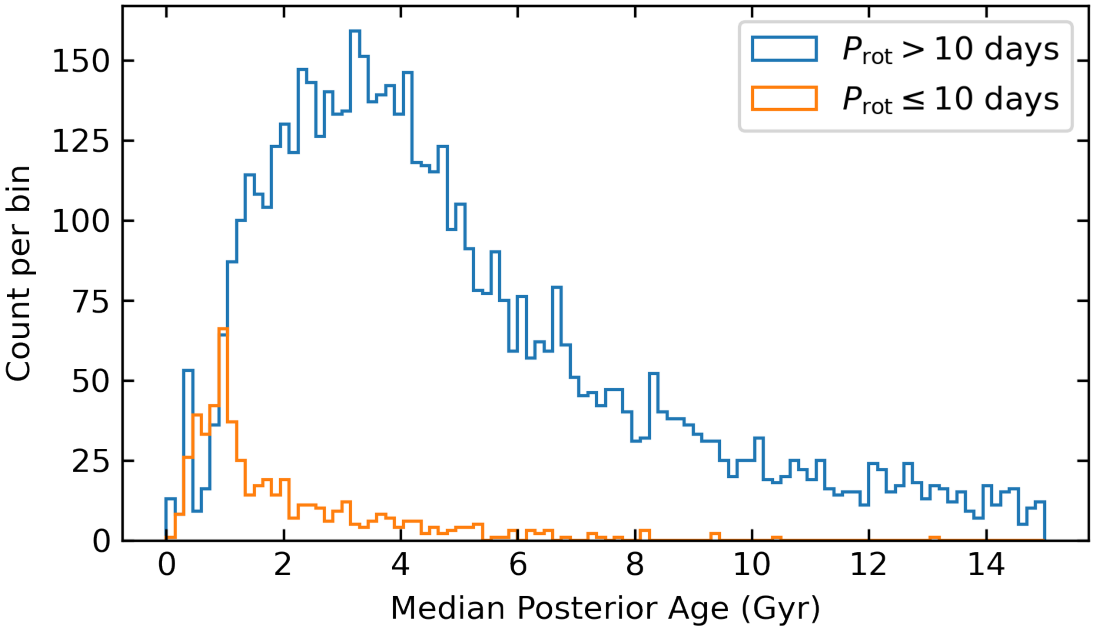

Figure 4.10: The distribution of rotation-based ages in the TESS SCVZ. We separate stars with periods less than 10 days, which are more likely to be tidally synchronized binaries than true rapid rotators (Simonian et al. 2019).

their distribution peaks near 2 Gyr, but there is a nearby second peak at 3.5 Gyr. It is possible that the *Kepler* field ages are distributed differently than those in other fields. Since *Kepler* pointed along the edge of the Galactic plane, we might expect its ages to be younger than those in the TESS CVZs, which are directed out of the plane and may represent a fundamentally older sample.

With rotation-based ages and high-resolution APOGEE spectroscopic abundances, we can also look for Galactic chemical evolution trends in TESS (e.g., Silva Aguirre et al. 2018; Claytor et al. 2020). Stars of different ages show different chemical abundances, particularly in metals (e.g., Fe) and α-elements (e.g., O, Mg, Ca) (e.g., Bensby et al. 2014). These trends are caused by the dominance of type-II supernovae early in the Galaxy's lifetime, and then of type-Ia supernovae later in time (e.g., Feltzing et al. 2017). We expect old stars to have low metallicity but high α enhancement, while young stars should

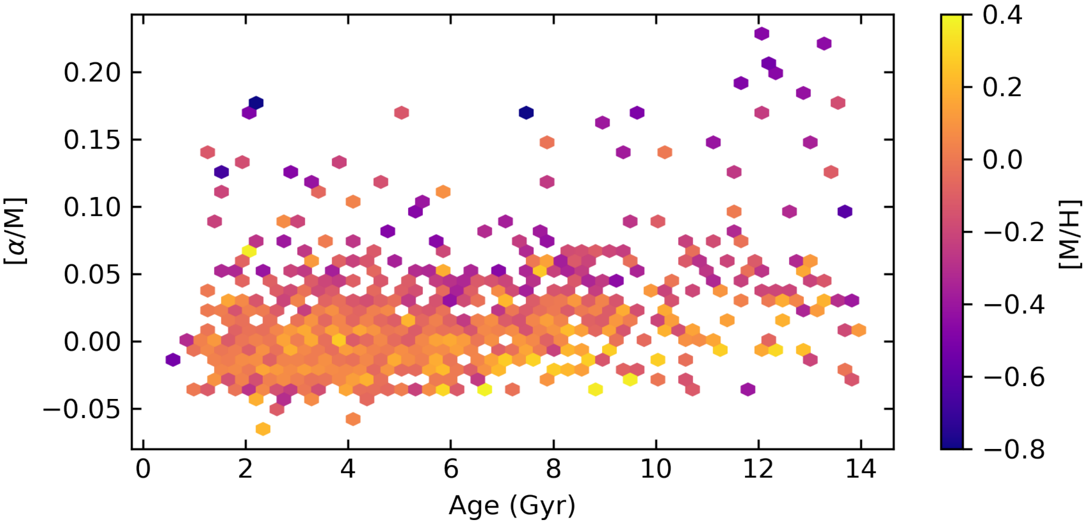

Figure 4.11: Stars of different ages exhibit different α-element abundances due to Galactic chemical evolution. Using rotation-based ages, we can corroborate the same trends in new parts of the sky.

have higher metallicity and lower α-element abundances (Haywood et al. 2013; Bensby et al. 2014; Martig et al. 2016; Feltzing et al. 2017; Buder et al. 2019). These young and old populations are representative of the classical Galactic "thin" and "thick" disks, respectively.

Figure 4.11 shows stellar α-element abundance as a function of rotation-based age in the TESS SCVZ. As expected, young stars are generally α-poor and metal-rich. There is a slight increasing trend of α enhancement with age. Older than about 8 Gyr, there is a larger spread in α enhancement, but the distribution of these stars' α abundances is more positive than that of the younger stars. The relative dearth of stars in the older regime is most likely caused by detection bias. Old stars tend to rotate more slowly and be less active, making them difficult to detect in rotation. Finally, we also detect a few young α-rich stars. These are known from other samples (e.g., Martig et al. 2015; Silva Aguirre et al. 2018; Claytor et al. 2020) and are likely to be the products of stellar mergers. In this scenario, two old,

α-enhanced stars merge, destroying the stars' rotation histories and yielding a fast-rotating, apparently young, α-enhanced product (Zhang et al. 2021).

Finally, with rotationally characterized stars we can begin to investigate trends of photometric activity with model-derived parameters like age and Rossby number. We define Rossby number as the ratio of the rotation period over the convective overturn timescale $\tau_{\rm cz}$, the latter of which is inferred from our models. To quantify the photometric activity, here we will use the photometric activity index $S_{\rm ph}$ rather than $R_{\rm per}$ so that we can compare the trends in the TESS SCVZ with those in the *Kepler* field observed by Santos et al. (2019, 2021), and Mathur et al. (in prep.). Like Mathur et al., we compute $S_{\rm ph}$ by partitioning the light curve into segments of duration $5P_{\rm rot}$, then taking the standard deviation of the light curve flux over each segment. This creates a time series of standard deviations; $S_{\rm ph}$ is taken to be the median value. The ages and and Rossby numbers for the Mathur et al. sample were computed using the same procedure and models underlying this work, so we can directly compare the *Kepler* and TESS distributions. We select the subset of our "gold" sample with the best-converged MCMC chains for the purest comparison with *Kepler*. We also discard stars with periods less than 10 days as before, leaving 161 stars with TESS periods, APOGEE spectroscopic parameters, and well-determined Rossby numbers and ages.

Figure 4.13 shows the photometric activity index $S_{\rm ph}$ versus the Rossby number for 161 of our APOGEE–TESS stars plotted over the distribution of stars from *Kepler*. As expected, activity decreases with increasing Rossby number. The TESS distribution generally agrees with the *Kepler* distribution. We have a few stars close to the high-activity saturated regime (e.g., Wright et al. 2011), but most of our stars are magnetically unsaturated. The TESS detection limits are clear here, as our lowest-activity star with a period detection has $S_{\rm ph} = 345$ ppm, compared to *Kepler*'s lower limit in the tens of ppm. We have a few

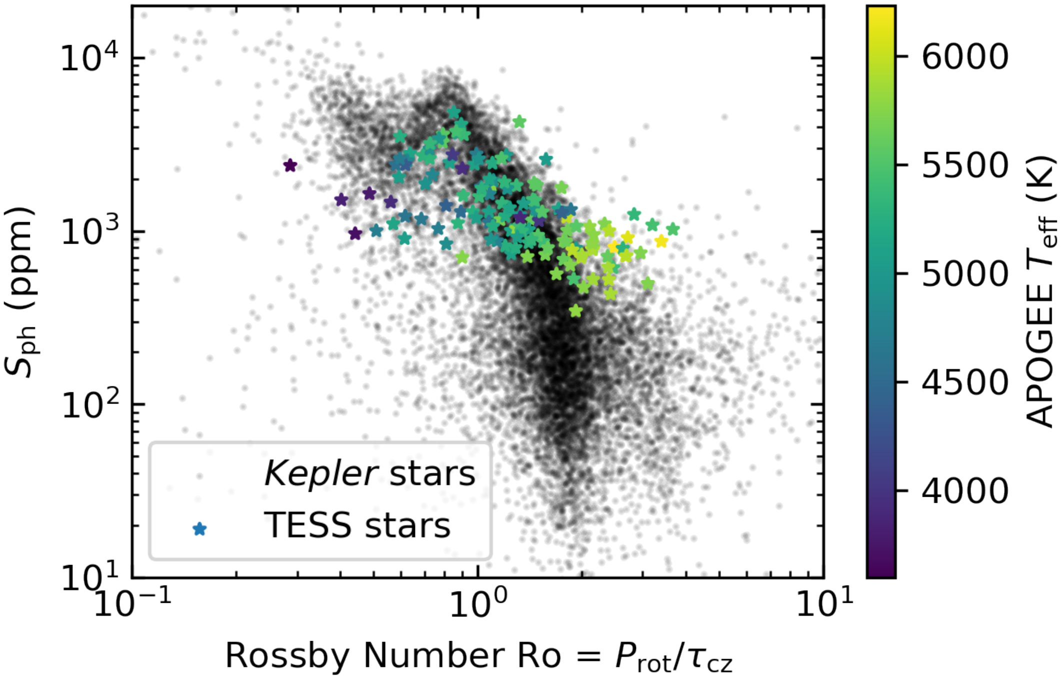

Figure 4.12: The stellar activity index $S_{\rm ph}$ versus Rossby number for 161 of the most reliably modeled stars in our APOGEE–TESS sample, plotted over the *Kepler* sample of Santos et al. (2019, 2021) and Mathur et al. (in prep.). As expected from theory and as seen in the *Kepler* field, photometric activity decreases with increasing Rossby number.

hot stars at Ro $\gtrsim$ 2 where *Kepler* has almost none. These are the likely spurious period detections from before (e.g., Figure 4.3).

We show $S_{\rm ph}$ as a function of rotation-based age in Figure 4.13. Photometric activity decreases with age, an effect of stellar spin-down. The TESS distribution follows the range and morphology of the *Kepler* distribution all the way down to the TESS rotation detection limit of $S_{\rm ph} \approx 350$ ppm.

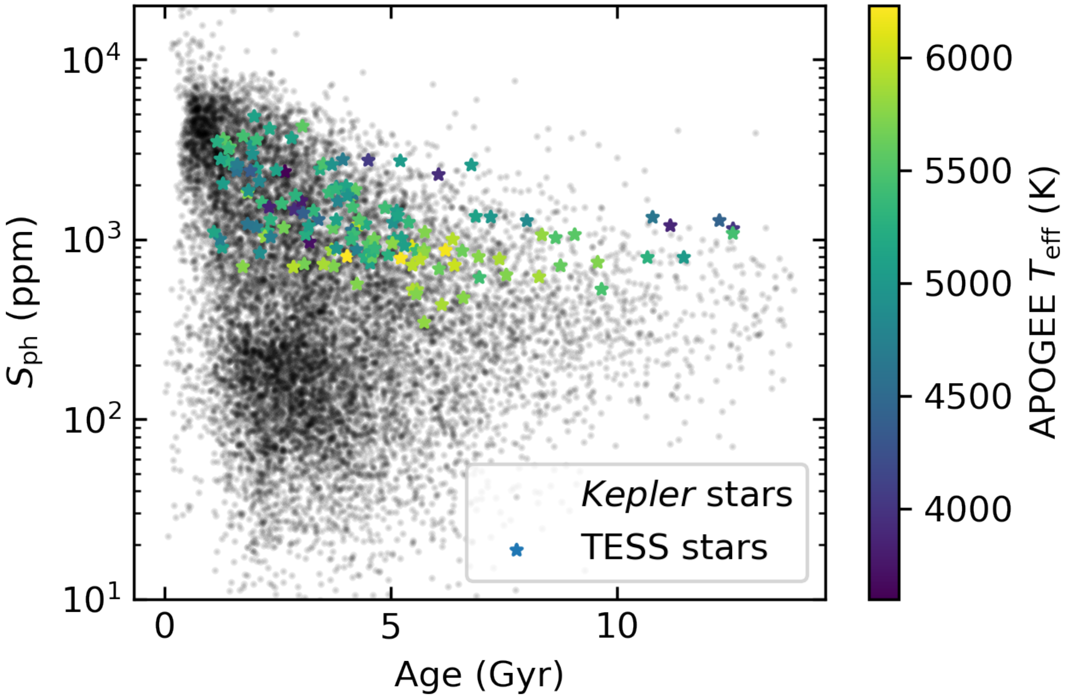

Figure 4.13: The stellar activity index S_{ph} versus rotation-based age for 161 of the most reliably modeled stars in our APOGEE–TESS sample, plotted over the *Kepler* sample of Santos et al. (2019, 2021) and Mathur et al. (in prep.). Photometric activity decreases as stars age, an effect of spin-down seen in the *Kepler* field and predicted by theory.

4.5 Detectability of Rotation

Here we consider the detectability of rotation as a function of various fundamental stellar parameters. To produce a measurable photometric signal, a star must be spotted, and the spots must contrast with the ambient stellar surface. The spots must also change in distance from the limb from the observer's perspective as the star rotates; a (circular, idealized) spot centered perfectly on the pole, however large or dark, will produce no rotational modulation. Similarly, a star viewed perfectly pole-on should produce no rotational modulation, as any spots in view will remain in view and contribute the same amount of attenuation at all times during the rotational phase.

Excluding pole-on orientations and perfectly pole-centered spots, the size, number, location, and contrast of surface spots affect the modulation amplitude. These properties are driven by the strength of magnetism at the stellar surface, which itself is powered by rotation and convection. Magnetism is generally stronger with faster rotation and deeper convective envelopes. Convective depth in low-mass stars is influenced largely by opacity, so effective temperature and metallicity help determine the thickness of the outer convective envelope. At cooler effective temperatures, metals in the outer layers of stars are less ionized and radiation is more easily absorbed, driving up the opacity. Higher opacity results in a steeper temperature gradient, making the layers more prone to convection. The cooler the effective temperature, the deeper the boundary where convection transports energy more efficiently than radiation. Similarly, higher metallicity means there are more electrons per atom to absorb radiation, so the opacity is higher as well. At a fixed rotation period, at lower temperature and higher metallicity, we expect deeper convective envelopes, stronger magnetism, more surface spots, and more easily detectable rotational modulation.

Besides changing with static stellar parameters, the strength of a star's magnetism changes as the star ages. Main-sequence stars with outer convective envelopes are born spinning fast and spin down as they age as they lose angular momentum to magnetized stellar winds (Kraft 1967; Skumanich 1972). The decrease in rotation speed results in a weakening magnetic field, fewer spots, and less flux modulation, making rotation more difficult to detect in older stars than in younger stars at fixed mass and composition.

While we might expect rotation to be harder to detect in lower metallicity stars, an age dependence enters the picture because of the variation of Galactic composition with age. Stars' initial composition patterns are set by the compositions of the clouds in which they form, which are in turn enriched by stars that have lived and died before them. Galactochemical evolution is often traced using the relative abundances of α elements to metals and metals to hydrogen (APOGEE provides values for [α/M] and [M/H], which we adopt). The background Galactic composition was governed by the dominance of core-collapse supernovae in the early Milky Way, followed by dominance of type Ia supernovae beginning about 8 Gyr ago. Both types of supernovae enriched the the interstellar medium (ISM) with metals, but in different ratios. Consequently, stars display decreasing [α/M] and increasing [M/H] with time (reversed as a function of age). Because the background abundance ratios change with time, any apparent changes in rotation detectability with stellar abundances may actually be caused by the decreasing detectability with age.

To investigate the detectability of rotation with fundamental stellar properties, let us consider the fraction of targets for which we detected periods in stellar parameter bins. While the neural network returns a period prediction for all targets, we can use the predicted uncertainty to determine whether those predictions are reliable. As in Claytor et al. (2022), we label targets with $\sigma_P/P < 0.35$ (corresponding to $\sim$10% median percent error) as successful detections, and anything else as a nondetection.

Figure 4.14 shows the rotation detection fraction versus temperature and metallicity. Only bins with at least five targets are shown so that the diagram is not muddled by small number fluctuations. As expected, cooler stars, especially cooler than 5,200 K, are detected in period significantly more often than hotter stars. In the range $5,200\ \mathrm{K} < T_{\mathrm{eff}} \lesssim 5,800\ \mathrm{K}$, where the detections begin to decrease as a function of temperature, there appears to be a weak trend in metallicity, with higher-metallicity ([M/H] $\gtrsim -0.1$) stars being detected in period more frequently than lower-metallicity stars. This is consistent with Amard et al. (2020); See et al. (2021), who found that rotation is more easily detected in *Kepler* stars with higher metallicity at fixed mass. However, Amard et al. (2020); See et al. (2021) do not separate the metallicity dependence from age, so it is difficult to say whether metallicity is the fundamental cause of the increased detectability. We see the same bias toward higher metallicity among our rotators, either due to the deeper convective envelope resulting from

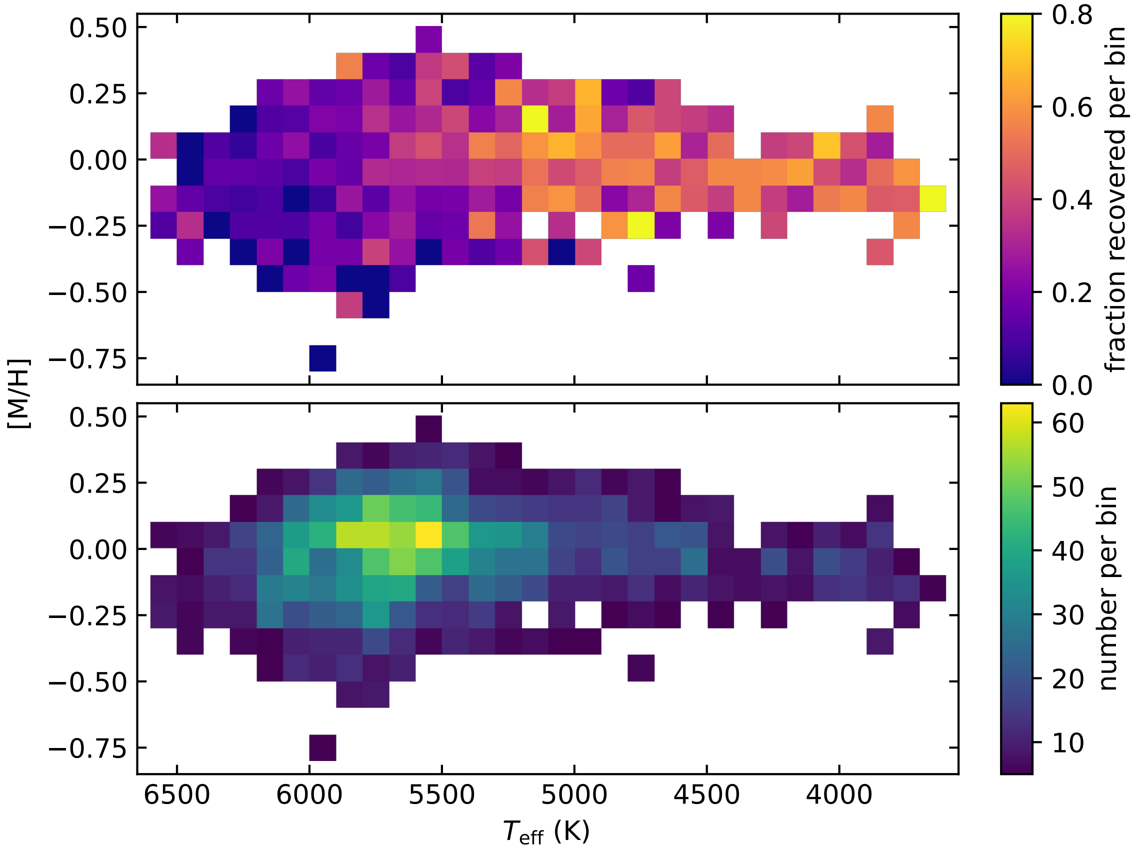

Figure 4.14: The detectability of rotation across APOGEE temperature and metallicity. We preferentially detect rotation in cool stars, which have deeper convective envelopes and are more active. When the detectability drops off as a function of temperature, we see a weak trend of increasing detectability with increasing metallicity. This may be due to metallicity increasing the convective depth at fixed temperature. It may also be an age effect, as young, active stars tend to be more metal-rich.

enhanced opacity, or to the fact that younger, more active stars are enriched by metals from Galactic chemical evolution.

Another view of the detection fraction is shown in Figure 4.15, this time as a function of metallicity and α-element enhancement. At fixed metallicity, we detect fewer stars in rotation at high [α/M] due to the underlying relationship between age and α-enhancement. High-α stars tend to be older, spin more slowly, and are less active, so we expect them to be more difficult to detect in rotation. This view also allows us to inspect the period detection

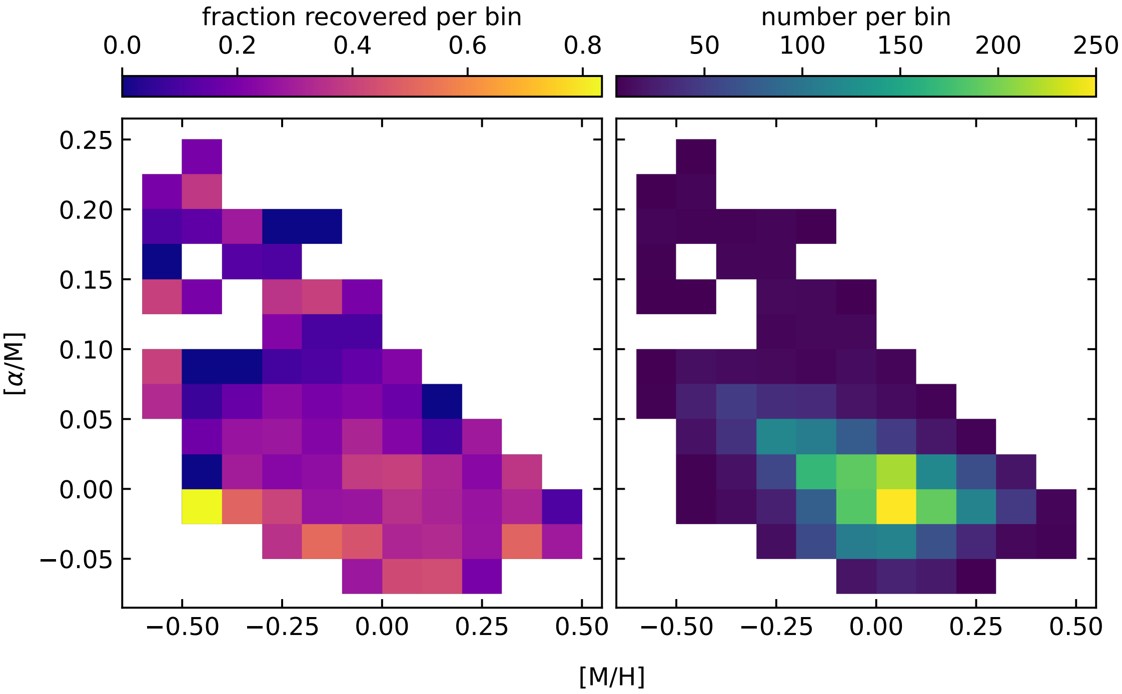

Figure 4.15: The detectability of rotation across APOGEE metallicity and α-element abundace. We detect fewer stars in rotation at high [α/M] because these stars tend to be old, slowly rotating, and less active. At fixed [α/M], there is scatter in the trend of detectability with metallicity from bin to bin.

fraction across metallicity at fixed α-enhancement. Since [α/M] varies so strongly with age, we can see how detectability changes with metallicity while nearly fixing age. At fixed [α/M], there is significant scatter in the detection fraction across metallicity. Some bins (e.g., $0 < [\alpha/M] < 0.025$) show gradually increasing detectability with increasing metallicity, while others (e.g., $-0.05 < [\alpha/M] < 0$) worsen in detection at higher metallicity. Thus, we can conclude that the apparently enhanced detection fraction at higher metallicity is due mainly to the underlying age distribution—metal-rich stars tend to be younger, spin faster, and are more active—rather than to higher levels of activity resulting from metal-driven opacity deepening the convective envelopes.

4.6 Spot Filling Fraction

The links between temperature, metallicity, age, convection, rotation, and photometric variability shed light on the generation of magnetism in cool, main-sequence stars. The strength of rotational modulation in the light curve, and therefore the detectability of rotation, hint at the presence of cool spots created by magnetic fields concentrated near the stellar surface. Because spots are created by the same dynamo that rotation and convection drive, the prevalence of those spots and how they connect to the distribution of rotation periods may tell us something new about the stellar interior and the emergence of magnetism.

Cao (2022) found that fitting APOGEE spectra with two temperature components allows one to infer the surface spot filling fraction and the temperature contrast of a star. Since star spots are a different temperature than the ambient stellar surface, the temperature dependence of spectral features is changed in a measurable way. They used a modified version of the FERRE code (Allende Prieto et al. 2006), the spectral fitting code used by the ASPCAP pipeline, with two temperature components to infer spot filling fractions for all stars in APOGEE DR16. Through collaboration, we obtained spot filling fractions and updated effective temperatures for the stars in our sample with APOGEE spectra.

We began with the 3,400 stars in our "gold" sample, which are cleaned of stars with ASPCAP STAR_BAD and SNR_BAD flags set, and have RUWE < 1.2 and flux contamination ratio < 0.1. Spot filling fractions inferred using two temperature components are particularly sensitive to binary interlopers, so we cleaned the sample further to remove risk of contamination. We made cuts in *Gaia* eDR3 magnitudes and colors using $M_G > 4.4$ and $G_{BP} - G_{RP} > 1$ to target below the field main-sequence turnoff and ensure all our stars are securely on the main sequence. This yielded 1,029 cool, main-sequence stars, but a few (less than 50) showed an excess in M_G, indicating that they

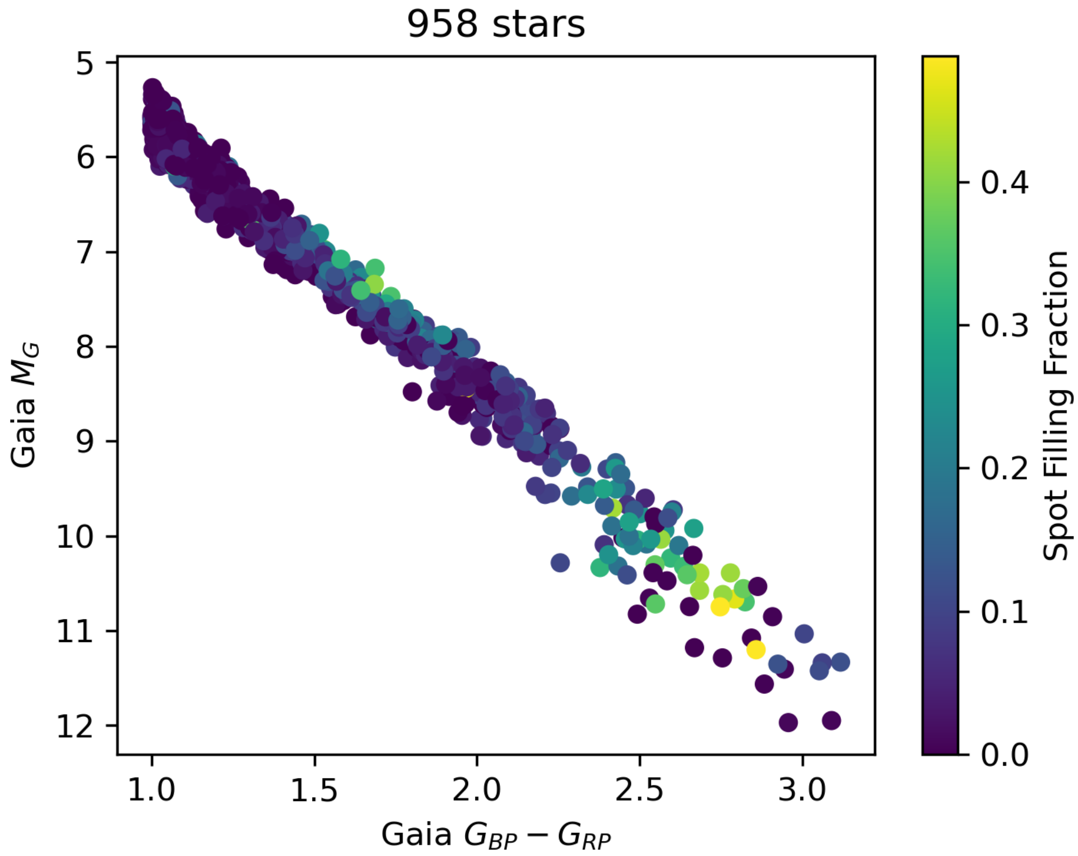

Figure 4.16: *Gaia* eDR3 color-magnitude diagram of our platinum cool main-sequence sample, colored by surface spot filling fraction. The sample is carefully cleaned of potential binary systems, which can interlope as falsely high spot filling fractions.

were likely leftover binary systems (e.g., Berger et al. 2018). To remove these, we fit a line to the main sequence and computed the magnitude excess as $\Delta M_G = \langle M_G \rangle - M_G$, where $\langle M_G \rangle$ was the fit main-sequence magnitude. The distribution of magnitude excesses had two clear peaks, with a trough we visually identified at $\Delta M_G = 0.4$. We removed stars with $\Delta M_G > 0.4$, leaving 958 stars. We designate these as our "platinum" sample, a pure, cool, main-sequence sample robustly free from binary contamination.

The platinum sample is shown in Figure 4.16, with points colored by spot filling fraction. While most stars in our sample exhibit low spot filling fractions less than 10%, two regimes have substantially higher fractions. At the red end of the main sequence, with $G_{BP} - G_{RP} > 2.3$ mag, M-dwarfs show filling fractions up to 50%. Since M-dwarfs tend to have higher photometric variability, we might reasonably assume they should have fuller spot coverage as well. The other regime is near $1.5 < G_{BP} - G_{RP} < 2$, in the mid-K range. Here, filling fractions reach ≈ 0.3–0.4, with a clear gradient of increasing filling fraction with increasing intrinsic brightness.

With spot filling fractions, we can now investigate the detectability of rotation as a function of surface spot coverage. We might expect more spotted stars to be easier to detect in rotation, as they should have higher photometric variability. Figure 4.17 shows the 213 platinum sample K-dwarfs with $1.5 < G_{BP} - G_{RP} < 2$, divided into rotation-detected and non-detected subsamples. The left panel shows the subsamples' distributions of spot filling fractions, while the right panel shows the cumulative frequency distributions. The cumulative distribution seems to suggest that the stars detected in rotation have higher spot filling fractions on average, but there are too few stars in this regime to confirm any difference in spot filling fraction between the period detection and nondetection samples. A Kolmogorov–Smirnov (K-S) test returns a p-value of 0.0736. With this, we can reject the null hypothesis that the two samples are drawn from the same underlying distribution with only 93% (i.e., less than 2σ) significance. Furthermore the K-S statistic is very sensitive to the lower bound of spot filling fraction, which is close to the edge of the grid. If we change the lower bound on filling fraction to 0.1, the K-S p-value is 0.17, now favoring undetected stars for more spot coverage (a reversal from before) with 83% significance.

Figure 4.18 shows the period–temperature distribution of our platinum sample, again colored by spot filling fraction, with the rotation sequences from benchmark open clusters Pleiades (Rebull et al. 2016), Praesepe (Douglas et al. 2017, 2019), NGC 6811 (Curtis et al. 2019), Ruprecht 147 (Curtis et al. 2020), and M67 (Curtis et al. 2020; Dungee 2022). Here we use the two-component fit effective temperature, rather than the TIC or ASPCAP

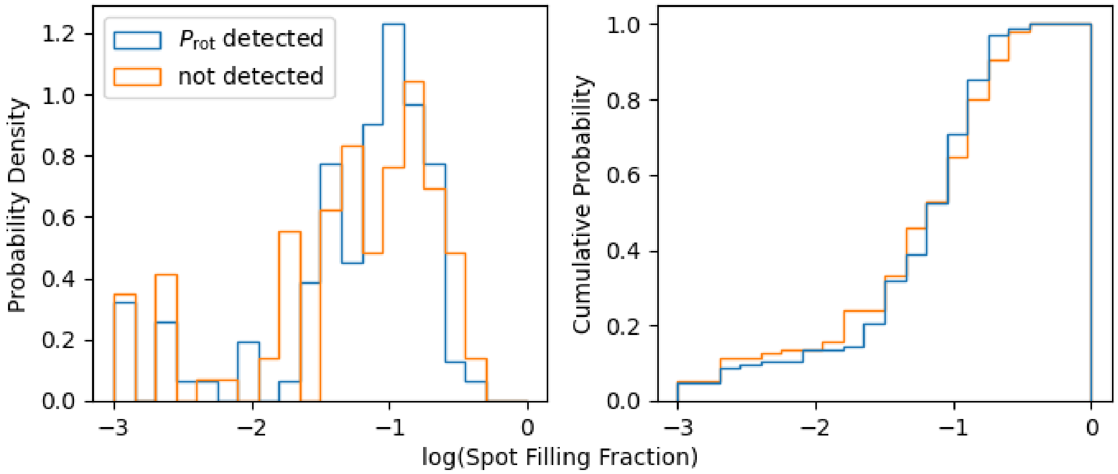

Figure 4.17: The distribution of spot filling fractions separated by whether rotation was detected in the *Gaia* color range $1.5 < G_{BP} - G_{RP} < 2$. While we might expect more spotted stars to be easier to detect in rotation, there are too few stars to draw any statistically significant conclusions.

values, for consistency with the spot filling fractions. As a function of temperature, TESS spot filling fractions are low at the hot end, increase in the mid-K range, decrease again in the early M range, and finally increase in the late M dwarfs. At fixed temperature, we might expect filling fractions to be higher at shorter periods, where stars rotate faster and are more magnetically active. However, we do not see such a trend with any significance. It may be that we lack enough stars in these narrow temperature ranges for the expected trend to show. Another possibility is that, due to the TESS detection edge in period at about 27 days, we do not reach periods long enough for spot filling fractions to substantially decrease.

The increase in spot filling fraction occurs in the color and temperature range where open clusters NGC 6811 and Rup 147 were shown to exhibit an unexpected epoch of stalled rotational braking (Curtis et al. 2019, 2020). NGC 6811 is 1 Gyr old (Curtis et al. 2019), but for temperatures cooler than 5,000 K its rotation sequence rests upon that of the 670-Myr-old Praesepe (Douglas et al. 2017, 2019). Somewhere between the ages of these clusters, stellar spin-down departs from the classical picture from gyrochronology. By 2.7 Gyr (Rup

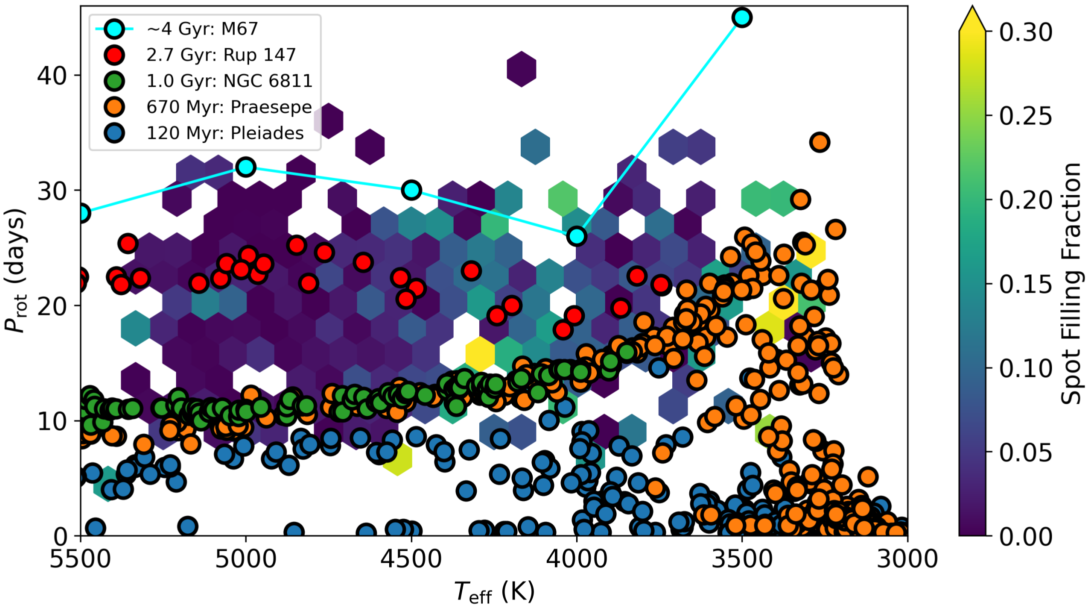

Figure 4.18: The TESS period distribution, colored by spot filling fraction, and plotted with rotation sequences of benchmark open clusters. In the K temperature range (between 4,000 and 4,500 K), NGC 6811 and Rup 147 exhibit stalled rotational braking, a departure from current gyrochronological models. The spot filling fractions are elevated here as well.

147, Curtis et al. 2020), stars at the hot end have resumed braking, but the cooler stars lag behind, suggesting that the epoch of stalled braking lasts longer for lower-mass stars.

Curtis et al. (2020) showed that a two-zone model, which allows the core and envelope to rotate at different rates, can almost reproduce the stalled spin-down behavior exhibited by these clusters. In these models, such as those by Spada & Lanzafame (2020), the core and envelope decouple, and the envelope continues to spin down from magnetic braking while the core maintains its rotation speed. As the core and envelope recouple, angular momentum is transferred from the core to the envelope, and braking is temporarily slowed or halted. After recoupling, the star undergoes classical, Skumanich-like braking behavior. While Curtis et al. (2020) argued in favor of the two-zone model, they could not rule out a temporary reduction in the braking torque, either from reduced wind or weakening of the magnetic field, as a possible cause. The coincidence of elevated spot filling fractions, stalled braking, and the rotation period gap in young, cool dwarfs suggests that the mechanisms causing them may be one and the same.

We note that the anomalously high K-dwarf spot filling fractions in open clusters are the subject of work by Cao et al. (in prep.), but the exploration of filling fractions in field dwarfs, and especially with rotation in TESS, is novel work.

4.7 Summary & Conclusion

We used deep learning to predict reliable periods for 9,837 main sequence stars near the southern ecliptic pole from year-long TESS full-frame image light curves. Our periods represent the first large-scale recovery and measurement of rotation in TESS stars rotating more slowly than 13.7 days, the limit previously imposed by TESS's complicated systematics. We fit stellar evolutionary models to the stars using rotation and high-resolution spectroscopic parameters to determine stellar ages, masses, convection timescales, Rossby numbers, and more. We investigated the detectability of rotation as a function of fundamental stellar parameters as well as new spot filling fractions inferred from spectroscopy. Our key results and conclusions are as follows:

- We detect the intermediate rotation period gap, first discovered in the *Kepler* field and seen in K2 field star samples across the ecliptic plane, the first such detection from TESS stars. The period gap in TESS closely aligns with the gaps from previous missions, cementing the conclusion that the gap is a product of stellar structure and evolution and not star formation history.

- The rotation period gap coincides with a dip in photometric variability, corroborating the findings of Reinhold et al. (2019); Reinhold & Hekker (2020) in other field star populations. This hints that a decrease in variability may partly explain the gap, but we cannot rule out a core–envelope decoupling hypothesis.

- The distribution of rotation periods in TESS closely resembles the distributions seen by *Kepler* and K2. Its lower edge features a slope of increasing period with decreasing temperature, similar to the distributions from previous missions, and we detect slowly rotating M-dwarfs with a similar location and distribution as in *Kepler*.
- The likelihood of detecting rotation is a strong function of variability amplitude, which is itself a function of age, rotation period, convection, temperature, and metallicity.
- In *Gaia* color regimes with a range of spot filling fractions, stars detected in rotation showed no significant difference in spot filling fraction compared to stars with no period detection.
- Field stars with elevated spot filling fractions coincide with open cluster stars that exhibit a temporary stall in magnetic braking. These coincide at least partly with the period gap and its variability depression, suggesting a common cause.

After four years of science operations, the secrets of main sequence stellar rotation are no longer off limits to us with TESS. While TESS systematics have presented unique challenges that remain difficult to solve with conventional period-finding techniques, deep learning presents a way to circumvent TESS systematics without having to solve systematics removal for every individual case.

Since first observing the southern hemisphere in 2018, TESS has also observed the North, revisited both hemispheres, and continues to observe the entire sky in its search for transiting exoplanets. As it does, it continues to build a vast trove of stellar light curves that are now available to search for rotation. Unlike Kepler and K2, TESS offers a look at stellar rotation across the entire sky and throughout our Galaxy. With the ability to explore rotation and its evolution in stars throughout the entire sky, a complete picture of rotation, activity, and magnetism may be within our grasp.

Chapter 5

Summary & Future Work

In this work we developed a deep learning approach to estimate, for the first time, long (> 13 d) rotation periods from TESS and performed the first rotational science with long-period TESS stars. We employed simulation-driven inference using convolutional neural networks (CNNs) and demonstrated the ability to recover literature periods up to 45 days. Generating new training sets tailored to different sets of light curves and optimizing new network architectures, we obtained reliable rotation periods for 9,837 stars in the TESS Southern Continuous Viewing Zone (SCVZ), spanning 5 to 60 days. We combined these periods with spectroscopic parameters from APOGEE to explore how the detectability of rotation varies with fundamental stellar parameters. Using a grid-based modeling approach, we inferred masses, radii, ages, and Rossby numbers for 6,632 stars with TESS period and APOGEE spectroscopy, then we compared evolution trends in the TESS SCVZ to those seen in the *Kepler* field. Finally, using spot filling fractions derived from APOGEE spectra, we investigated relationships between surface spot coverage, rotation, and activity. Our final conclusions are as follows:

- CNNs can be used to successfully learn systematics in TESS photometric time series and regress long periods in spite of them, something no conventional period-finding technique has been able to do in TESS.

- With the right choice of loss function, CNNs can also predict the uncertainty in the rotation period, which can be used to filter out bad predictions.
- The success rate of predicting periods depends strongly on the photometric variability of the star, but filtering predictions by uncertainty somewhat weakens this dependence.
- In our approach, the range of periods our CNN could successfully predict was smaller than the input range of the training set, as uncertain predictions were biased toward the median period.
- The rotation period gap is present in the TESS SCVZ and lies in the same temperature and period ranges as in the *Kepler* field. The gap is therefore a universal feature among Milky Way stars and is caused by a change in braking law and/or a depression in photometric variability, rather than a local pause in star formation.
- The period gap aligns with a depression in photometric variability, suggesting that a decrease in variability may partly explain the gap, but we cannot rule out a change in magnetic braking.
- The TESS period–temperature distribution has the same short-period edge as the *Kepler* distribution, cementing the hypothesis that this edge and its value are set by stellar rotational evolution, rather than by the age distribution.
- The detectability of rotation depends strongly on the temperature and age, the former due to its influence on the convective depth, and the latter due to its effect on rotation speed.
- The age distribution of TESS SCVZ stars resembles the distribution of ages in some parts of the sky, but there may be tension with the *Kepler* age distribution,

suggesting the TESS SCVZ may sample a fundamentally different stellar population than *Kepler*.

- Between temperatures of 4,000 K and 4,500 K, stars exhibit elevated spot filling fractions, a change in magnetic braking, the rotation period gap, and a dip in variability, suggesting all these may share a common cause.

5.1 Data Products

This work involved the development of several data products, tools, and software packages, which we outline with publication status below.

- `butterpy`, a Python package to simulate star spot evolution and the corresponding light curves (Claytor et al. 2021; Claytor et al. 2022). The package is open source on GitHub and installable with `pip` from the Python Package Index.
- SMARTS-TESS, the full training set of simulated rotational light curves described in Chapter 2 and Claytor et al. (2022). SMARTS-TESS is publicly available as a MAST High-Level Science Product.
- `kiauhoku`, a Python package to interact with, interpolate, and sample stellar evolutionary model grids. The package is open source on GitHub and installable with `pip` from the Python Package Index.
- Rotation period table for 9,837 TESS SCVZ stars, spanning periods of 5 to 60 days, to be published with Chapter 4.
- Stellar properties table for 6,632 TESS SCVZ stars with reliable period estimates, APOGEE infrared spectroscopic parameters, and model-inferred masses, ages, and other fundamental parameters, to be published with Chapter 4.

5.2 Future Work

TESS has now observed the northern hemisphere, carving out another continuous viewing zone around the northern ecliptic pole. It has also repeated observations for both the South and North, totaling two years of coverage for each hemisphere. We plan to apply the method described here to the stars in the North (year 2) to supplement the rotation period catalog. The revisits to the South (year 3) and North (year 4) will also provide opportunities to look for changing periodicity in TESS stars.

Since our training light curves contain sector gaps, our method is not strictly limited to use in the CVZs. We could apply this procedure to stars with fewer sectors of coverage to obtain rotation periods for a larger part of the sky.

During the completion of this work, Holcomb et al. (2022); Colman (2022), and others made substantial progress on the front of short (< 13 d) rotation period measurements in TESS. It will be useful to compare estimates and biases for stars common to our samples.

In addition to rotation period, our training light curves encompass activity levels, surface differential rotation, spot lifetimes, and more. While currently our CNNs only predict values for the period, they could be modified to predict any of the underlying model parameters. In the future, we may want to predict activity levels to compare with photometric variability metrics like $S_{\rm ph}$ and $R_{\rm per}$ to quantify the effects of TESS systematics on light curve amplitudes. The newly available spot filling fraction measurements could also be useful to compare with CNN-inferred spot properties, to determine if spot properties can be inferred from the light curve without the need for additional data.

With long TESS periods no longer off limits, we can obtain period estimates for stars in both CVZs and across the entire sky. As we do, TESS will ultimately provide periods for more stars than *Kepler*, and in fundamentally different regions of space. With TESS we will sharpen our view of period distributions across the sky, shedding new light on the connections between rotation and magnetism.

Appendix A

Elemental Trends of *Kepler* Dwarfs with Age

APOGEE defines [α/M] as the combination of O, Mg, Si, S, Ca, and Ti (García Pérez et al. 2016). While [α/M] should capture the general enrichment and depletion trends from different kinds of supernovae, we may consider the evolution of individual elements as well. Fig. A.1 shows the evolution of the individual α-elements, as well as aluminum, across time. While aluminum is not an α-process element, we include it because its enrichment is generally driven by the same processes as α-process elements (e.g., Nomoto et al. 2013).

Magnesium and silicon show the strongest trends with age, which is expected since they, along with oxygen, dominate the value of [α/M] in our dwarf sample. Interestingly, oxygen shows little-to-no trend with age. It does have the most scatter at fixed age; this scatter may blur out any trends across time.

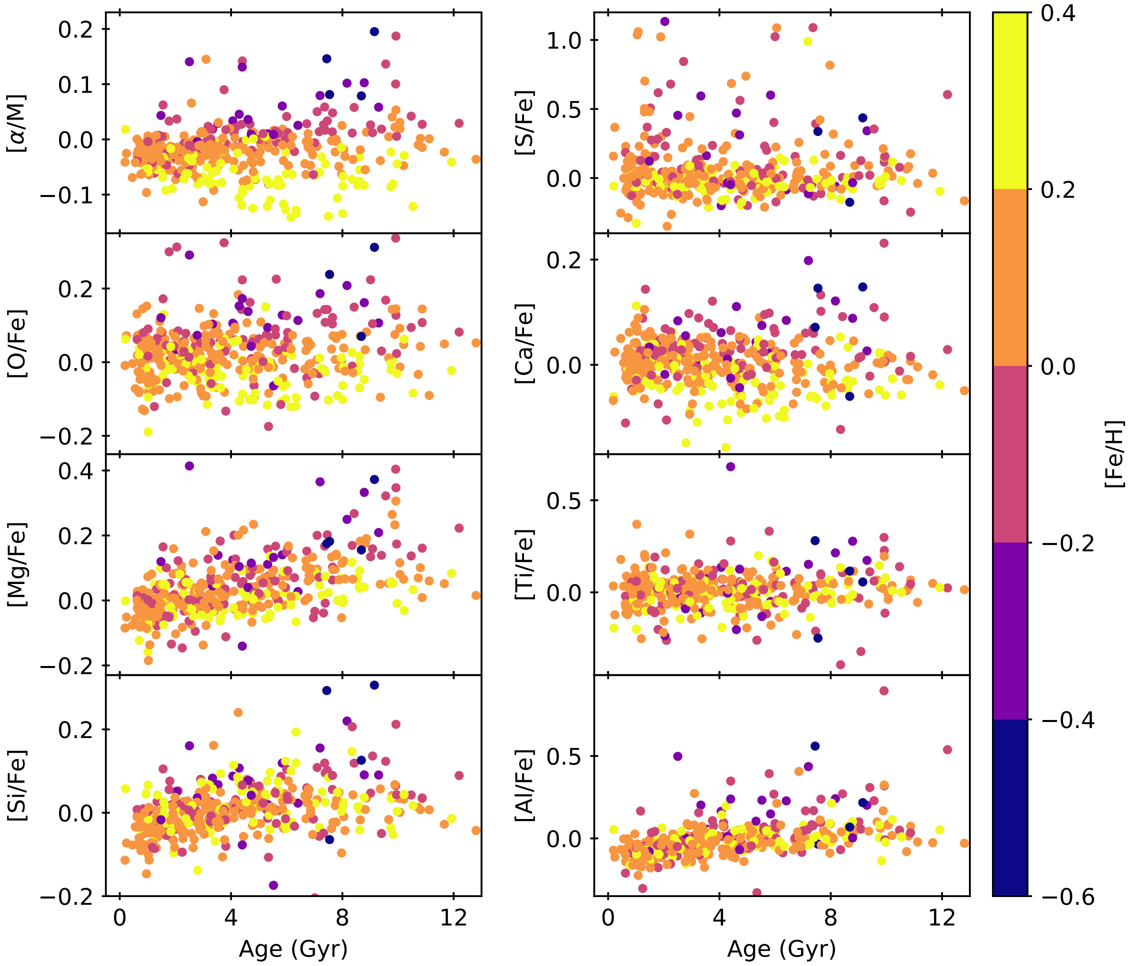

Figure A.1: The enrichment of α-process elements (and aluminum) with age.

Appendix B

Optimizing the Neural Network Architecture

In Section 4.2.2 we lay out the various convolutional neural network (CNN) architectures that we trained and assessed to optimize our network's performance. Here we discuss the details of that optimization and the justification for our choices of architecture.

For both the TESS-SPOC and TASOC data products, we trained four different CNNs, each with 3 convolution layers, but each CNN had different numbers of convolution kernels to give the networks different flexibility in learning features. The architectures were (A) 8, 16, and 32 kernels; (B) 6, 32, and 64 kernels; (C) 32, 64, and 128; and (D) 64, 128, and 256. We also used four different training sets for both TESS-SPOC and TASOC, each with a different upper limit on rotation period. The period upper limits were 30, 60, 90, and 180 days, intended to optimize different networks for different period ranges. We trained all four architectures on each period range, compared performance metrics, and chose the architecture that had the best performance on average across all four training sets. For performance metrics, we considered, (1) average test loss, (2) median predicted relative uncertainty, (3) percentage of test targets recovered to within 10% and 20% accuracy, and (4) the 1st and 99th percentiles of the filtered predicted periods. To illustrate the meaning of these values, we will use the 180-day TESS-SPOC training set as an example.

During training, each training set is partitioned into a training, validation, and test set. The training set is used to fit the network parameters, the validation set is used to determine when to stop training to avoid overfitting, and the test set is used to assess performance. We monitored the average loss for all three partitions during training so that we can construct learning curves, which show the loss values versus training epoch. Figure B.1 shows the learning curves for all four architectures on the 180-day training set. The solid lines represent the training loss, while the dashed lines represent the test loss. Left unchecked, training loss will continue to decrease, but the loss on a held-out validation set will plateau or begin to increase once the network begins overfitting, which we use as our stopping criterion. The test loss is highest for run A, the simplest architecture we used. This indicates that run A is not complex enough to fully learn the features in the data, or at least that it begins overfitting before it can fully learn the features. Run B performs better, but is comparable to runs C and D, which fully train in fewer epochs. We can rule out run A for this case, but more metrics are needed to properly assess which run performs best.

As we discuss in Chapter 2, one of the strengths of our method is the ability to predict an uncertainty, which we can use as a metric of prediction reliability. Specifically, we use the fractional uncertainty σ_P/P to normalize for period dependence. A better-trained network should have lower values of σ_P/P, indicating more reliable predictions. We use the median σ_P/P as an additional metric of performance in addition to using it to filter out bad predictions. Figure B.2 shows the *filtered* period predictions for each run, but note that the median fractional uncertainty listed in each panel is computed over the *unfiltered* predictions. Run B has the lowest predicted uncertainty, so by this metric it performs the best and has the most reliable predictions.

Besides the predicted uncertainty, we also use accuracy metrics to assess performance. The “acc10” and “acc20” metrics quantify what fraction of test targets are recovered to within 10% and 20% accuracy after filtering by predicted uncertainty. The “acc10”

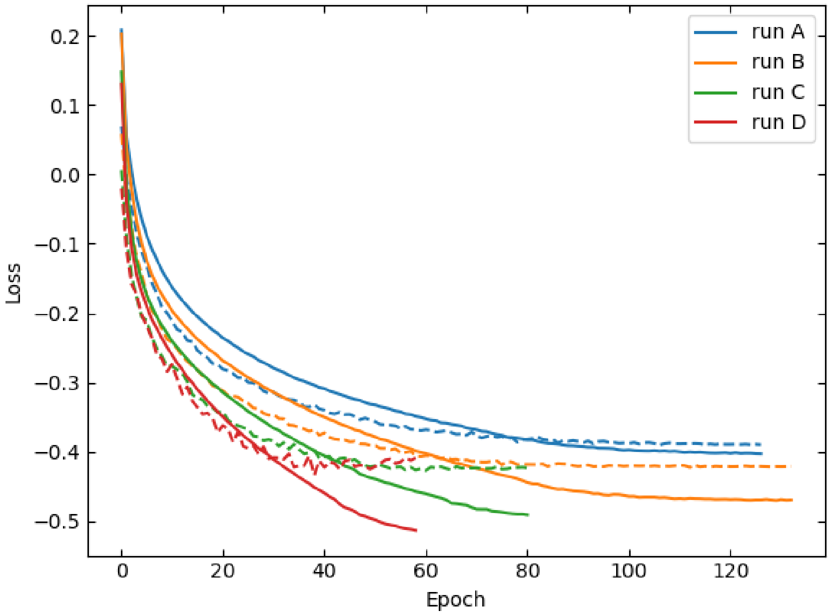

Figure B.1: Learning curves of all four CNN architectures for the 180-day training set. The solid lines track the training loss, while the dashed lines show the test loss, which was used to assess performance of the networks once trained.

metrics for each run are near 50%, which also means that the median relative error on the predictions is near 10% for all runs. Run B has the highest accuracy metrics, so it once again performs best.

In Section 2.6.1, we discussed a potential shortcoming of our CNN approach owing to our choice of loss function. Namely, predicting uncertainty biases predictions toward the median of the distribution, making period prediction near the edges of the training set period range more difficult. We attempt to mitigate this by tabulating the 1st and 99th percentiles of each (unfiltered and filtered) predicted period range. Figure B.3 shows the distribution of predicted periods for both the unfiltered (left) and filtered (right) predictions. Though it is difficult to assess by eye, run A has the lowest 1st percentile (12.1 d) in the filtered sample, although all runs have first percentiles in the 12–13 day range. This also gives us a lower limit for where we can expect successful period predictions from this

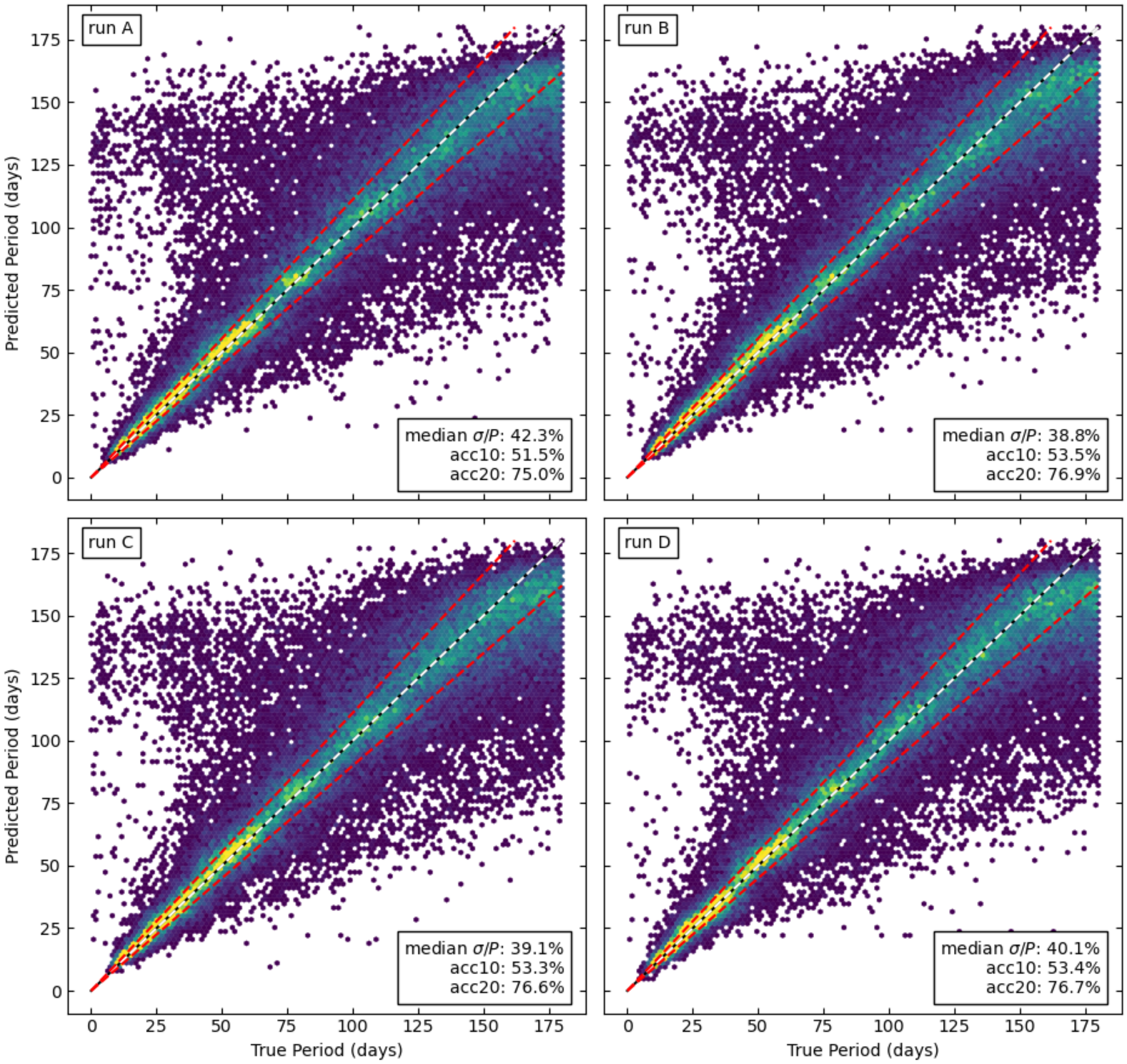

Figure B.2: Period detections for different CNN architectures, filtered by predicted relative uncertainty. Architectures are increasingly complex from A to D, and recovery statistics are shown in the legend of each panel.

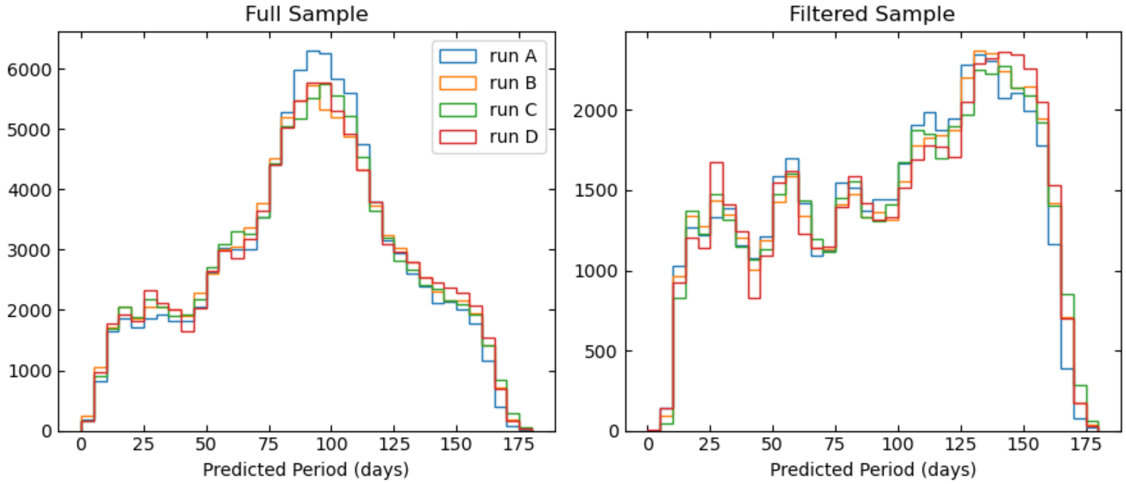

Figure B.3: Distributions of predicted rotation periods for different CNN architectures, for both the unfiltered (left) and filtere (right) samples.

training set: networks trained on the 180-day set struggle to predict periods less than 12 days, motivating the need for training sets with smaller period ranges.

We prioritized metrics as follows: we considered the average test loss to rule out runs that failed to compete in loss value (e.g., runs B, C, and D achieved comparable loss values, but run A fell short). We then prioritized the accuracy metrics and predicted uncertainty together, then if those were comparable we used the 1st and 99th percentile values to break ties.

When considering all our metrics for the 180-day TESS-SPOC training set, run B performs the best overall. We then repeated this process for each training set and chose the architecture that performed best over all training sets. Following this procedure, we chose architecture C for the TESS-SPOC data and architecture A for TASOC. We note that it may be optimal to use the optimal architecture for each training set, rather than adopt one architecture for all sets. We will consider before publication and release of the final period catalog.

References

Abdurro'uf, Accetta, K., Aerts, C., Silva Aguirre, V., Ahumada, R., Ajgaonkar, N., Filiz Ak, N., Alam, S., Allende Prieto, C., Almeida, A., & et al. 2022, ApJS, 259, 35

Adelberger, E. G., García, A., Robertson, R. G. H., Snover, K. A., Balantekin, A. B., Heeger, K., Ramsey-Musolf, M. J., Bemmerer, D., Junghans, A., Bertulani, C. A., Chen, J. W., Costantini, H., Prati, P., Couder, M., Uberseder, E., Wiescher, M., Cyburt, R., Davids, B., Freedman, S. J., Gai, M., Gazit, D., Gialanella, L., Imbriani, G., Greife, U., Hass, M., Haxton, W. C., Itahashi, T., Kubodera, K., Langanke, K., Leitner, D., Leitner, M., Vetter, P., Winslow, L., Marcucci, L. E., Motobayashi, T., Mukhamedzhanov, A., Tribble, R. E., Nollett, K. M., Nunes, F. M., Park, T. S., Parker, P. D., Schiavilla, R., Simpson, E. C., Spitaleri, C., Strieder, F., Trautvetter, H. P., Suemmerer, K., & Typel, S. 2011, Reviews of Modern Physics, 83, 195

Affer, L., Micela, G., Favata, F., & Flaccomio, E. 2012, MNRAS, 424, 11

Agüeros, M. A., Bowsher, E. C., Bochanski, J. J., Cargile, P. A., Covey, K. R., Douglas, S. T., Kraus, A., Kundert, A., Law, N. M., Ahmadi, A., & Arce, H. G. 2018, ApJ, 862, 33

Aigrain, S., Llama, J., Ceillier, T., Chagas, M. L. d., Davenport, J. R. A., García, R. A., Hay, K. L., Lanza, A. F., McQuillan, A., Mazeh, T., de Medeiros, J. R., Nielsen, M. B., & Reinhold, T. 2015, MNRAS, 450, 3211

Aigrain, S., Pont, F., & Zucker, S. 2012, MNRAS, 419, 3147

Allende Prieto, C., Beers, T. C., Wilhelm, R., Newberg, H. J., Rockosi, C. M., Yanny, B., & Lee, Y. S. 2006, ApJ, 636, 804

Amard, L., Roquette, J., & Matt, S. P. 2020, MNRAS, 499, 3481

Angus, R., Aigrain, S., Foreman-Mackey, D., & McQuillan, A. 2015, MNRAS, 450, 1787

Angus, R., Morton, T., Aigrain, S., Foreman-Mackey, D., & Rajpaul, V. 2018, MNRAS, 474, 2094

Arenou, F., Luri, X., Babusiaux, C., Fabricius, C., Helmi, A., Muraveva, T., Robin, A. C., Spoto, F., Vallenari, A., Antoja, T., Cantat-Gaudin, T., Jordi, C., Leclerc, N., Reylé, C., Romero-Gómez, M., Shih, I.-C., Soria, S., Barache, C., Bossini, D., Bragaglia, A., Breddels, M. A., Fabrizio, M., Lambert, S., Marrese, P. M., Massari, D., Moitinho, A., Robichon, N., Ruiz-Dern, L., Sordo, R., Veljanoski, J., Eyer, L., Jasniewicz, G., Pancino, E., Soubiran, C., Spagna, A., Tanga, P., Turon, C., & Zurbach, C. 2018, A&A, 616, A17

Avallone, E. A., Tayar, J. N., van Saders, J. L., Berger, T. A., Claytor, Z. R., Beaton, R. L., Teske, J., Godoy-Rivera, D., & Pan, K. 2022, ApJ, 930, 7

Baglin, A., Auvergne, M., Barge, P., Deleuil, M., Catala, C., Michel, E., Weiss, W., & COROT Team. 2006, in ESA Special Publication, Vol. 1306, The CoRoT Mission Pre-Launch Status - Stellar Seismology and Planet Finding, ed. M. Fridlund, A. Baglin, J. Lochard, & L. Conroy, 33

Bao, W., Yue, J., & Rao, Y. 2017, PLOS ONE, 12, 1

Barnes, S. A. 2003, ApJ, 586, 464

—. 2007, ApJ, 669, 1167

Barnes, S. A. & Kim, Y.-C. 2010, ApJ, 721, 675

Barnes, S. A., Weingrill, J., Fritzewski, D., Strassmeier, K. G., & Platais, I. 2016, ApJ, 823, 16

Basri, G. & Nguyen, H. T. 2018, ApJ, 863, 190

Basri, G., Walkowicz, L. M., Batalha, N., Gilliland, R. L., Jenkins, J., Borucki, W. J., Koch, D., Caldwell, D., Dupree, A. K., Latham, D. W., Marcy, G. W., Meibom, S., & Brown, T. 2011, AJ, 141, 20

Bazot, M., Nielsen, M. B., Mary, D., Christensen-Dalsgaard, J., Benomar, O., Petit, P., Gizon, L., Sreenivasan, K. R., & White, T. R. 2018, A&A, 619, L9

Bensby, T., Feltzing, S., & Lundström, I. 2003, A&A, 410, 527

Bensby, T., Feltzing, S., & Oey, M. S. 2014, A&A, 562, A71

Berger, T. A., Huber, D., Gaidos, E., & van Saders, J. L. 2018, ApJ, 866, 99

Berger, T. A., Huber, D., van Saders, J. L., Gaidos, E., Tayar, J., & Kraus, A. L. 2020, AJ, 159, 280

Berta, Z. K., Irwin, J., Charbonneau, D., Burke, C. J., & Falco, E. E. 2012, AJ, 144, 145

Blancato, K., Ness, M., Huber, D., Lu, Y., & Angus, R. 2020, arXiv e-prints, arXiv:2005.09682

Borucki, W. J., Koch, D., Basri, G., Batalha, N., Brown, T., Caldwell, D., Caldwell, J., Christensen-Dalsgaard, J., Cochran, W. D., DeVore, E., Dunham, E. W., Dupree, A. K., Gautier, T. N., Geary, J. C., Gilliland, R., Gould, A., Howell, S. B., Jenkins, J. M., Kondo, Y., Latham, D. W., Marcy, G. W., Meibom, S., Kjeldsen, H., Lissauer, J. J., Monet, D. G., Morrison, D., Sasselov, D., Tarter, J., Boss, A., Brownlee, D., Owen, T., Buzasi, D., Charbonneau, D., Doyle, L., Fortney, J., Ford, E. B., Holman, M. J., Seager, S., Steffen, J. H., Welsh, W. F., Rowe, J., Anderson, H., Buchhave, L., Ciardi, D., Walkowicz, L., Sherry, W., Horch, E., Isaacson, H., Everett, M. E., Fischer, D., Torres, G., Johnson, J. A., Endl, M., MacQueen, P., Bryson, S. T., Dotson, J., Haas, M., Kolodziejczak, J., Van Cleve, J., Chandrasekaran, H., Twicken, J. D., Quintana, E. V., Clarke, B. D., Allen, C., Li, J., Wu, H., Tenenbaum, P., Verner, E., Bruhweiler, F., Barnes, J., & Prsa, A. 2010, Science, 327, 977

Bovy, J., Rix, H.-W., & Hogg, D. W. 2012a, ApJ, 751, 131

Bovy, J., Rix, H.-W., Liu, C., Hogg, D. W., Beers, T. C., & Lee, Y. S. 2012b, ApJ, 753, 148

Brasseur, C. E., Phillip, C., Fleming, S. W., Mullally, S. E., & White, R. L. 2019, Astrocut: Tools for creating cutouts of TESS images

Breton, S. N., Santos, A. R. G., Bugnet, L., Mathur, S., García, R. A., & Pallé, P. L. 2021, A&A, 647, A125

Brown, T. M., Latham, D. W., Everett, M. E., & Esquerdo, G. A. 2011, AJ, 142, 112

Buder, S., Lind, K., Ness, M. K., Asplund, M., Duong, L., Lin, J., Kos, J., Casagrande, L., Casey, A. R., Bland-Hawthorn, J., de Silva, G. M., D'Orazi, V., Freeman, K. C., Martell, S. L., Schlesinger, K. J., Sharma, S., Simpson, J. D., Zucker, D. B., Zwitter, T., Čotar, K., Dotter, A., Hayden, M. R., Hyde, E. A., Kafle, P. R., Lewis, G. F., Nataf, D. M., Nordlander, T., Reid, W., Rix, H. W., Skúladóttir, Á., Stello, D., Ting, Y. S., Traven, G., Wyse, R. F. G., & Galah Collaboration. 2019, A&A, 624, A19

Caldwell, D. A., Tenenbaum, P., Twicken, J. D., Jenkins, J. M., Ting, E., Smith, J. C., Hedges, C., Fausnaugh, M. M., Rose, M., & Burke, C. 2020, Research Notes of the American Astronomical Society, 4, 201

Canto Martins, B. L., Gomes, R. L., Messias, Y. S., de Lira, S. R., Leão, I. C., Almeida, L. A., Teixeira, M. A., das Chagas, M. L., Bravo, J. P., Bewketu Belete, A., & De Medeiros, J. R. 2020, ApJS, 250, 20

Cao, L. 2022, in Fifty Years of the Skumanich Relations, ed. T. S. Metcalfe, 23

Carroll, B. W. & Ostlie, D. A. 2006, An introduction to modern astrophysics and cosmology (Pearson Addison-Wesley)

Castelli, F. & Kurucz, R. L. 2004, arXiv e-prints

Ceillier, T., Tayar, J., Mathur, S., Salabert, D., García, R. A., Stello, D., Pinsonneault, M. H., van Saders, J., Beck, P. G., & Bloemen, S. 2017, A&A, 605, A111

Ceillier, T., van Saders, J., García, R. A., Metcalfe, T. S., Creevey, O., Mathis, S., Mathur, S., Pinsonneault, M. H., Salabert, D., & Tayar, J. 2016, MNRAS, 456, 119

Chanamé, J. & Ramírez, I. 2012, ApJ, 746, 102

Chiappini, C., Anders, F., Rodrigues, T. S., Miglio, A., Montalbán, J., Mosser, B., Girardi, L., Valentini, M., Noels, A., Morel, T., Minchev, I., Steinmetz, M., Santiago, B. X., Schultheis, M., Martig, M., da Costa, L. N., Maia, M. A. G., Allende Prieto, C., de Assis Peralta, R., Hekker, S., Themeßl, N., Kallinger, T., García, R. A., Mathur, S., Baudin, F., Beers, T. C., Cunha, K., Harding, P., Holtzman, J., Majewski, S., Mészáros, S., Nidever, D., Pan, K., Schiavon, R. P., Shetrone, M. D., Schneider, D. P., & Stassun, K. 2015, A&A, 576, L12

Claytor, Z. R., Lucas, M., & Llama, J. 2021, Butterpy: realistic star spot evolution and light curves in Python

Claytor, Z. R., van Saders, J. L., Llama, J., Sadowski, P., Quach, B., & Avallone, E. A. 2022, ApJ, 927, 219

Claytor, Z. R., van Saders, J. L., Santos, Â. R. G., García, R. A., Mathur, S., Tayar, J., Pinsonneault, M. H., & Shetrone, M. 2020, ApJ, 888, 43

Colman, I. 2022, in Fifty Years of the Skumanich Relations, ed. T. S. Metcalfe, 36

Cox, J. P. & Giuli, R. T. 1968, Principles of Stellar Structure (New York: Gordon and Breach)

Cranmer, K., Brehmer, J., & Louppe, G. 2020, Proceedings of the National Academy of Sciences, 117, 30055

Cranmer, S. R. & Saar, S. H. 2011, ApJ, 741, 54

Creevey, O. L., Metcalfe, T. S., Schultheis, M., Salabert, D., Bazot, M., Thévenin, F., Mathur, S., Xu, H., & García, R. A. 2017, A&A, 601, A67

Curtis, J. L., Agüeros, M. A., Douglas, S. T., & Meibom, S. 2019, ApJ, 879, 49

Curtis, J. L., Agüeros, M. A., Matt, S. P., Covey, K. R., Douglas, S. T., Angus, R., Saar, S. H., Cody, A. M., Vanderburg, A., Law, N. M., Kraus, A. L., Latham, D. W., Baranec, C., Riddle, R., Ziegler, C., Lund, M. N., Torres, G., Meibom, S., Aguirre, V. S., & Wright, J. T. 2020, ApJ, 904, 140

Davenport, J. R. A. 2017, ApJ, 835, 16

Davenport, J. R. A. & Covey, K. R. 2018, ApJ, 868, 151

David, T. J., Angus, R., Curtis, J. L., van Saders, J. L., Colman, I. L., Contardo, G., Lu, Y., & Zinn, J. C. 2022, arXiv e-prints, arXiv:2203.08920

Demarque, P., Guenther, D. B., Li, L. H., Mazumdar, A., & Straka, C. W. 2008, Ap&SS, 316, 31

Denissenkov, P. A., Pinsonneault, M., Terndrup, D. M., & Newsham, G. 2010, ApJ, 716, 1269

Dotter, A. 2016, ApJS, 222, 8

Douglas, S. T., Agüeros, M. A., Covey, K. R., Cargile, P. A., Barclay, T., Cody, A., Howell, S. B., & Kopytova, T. 2016, ApJ, 822, 47

Douglas, S. T., Agüeros, M. A., Covey, K. R., & Kraus, A. 2017, ApJ, 842, 83

Douglas, S. T., Curtis, J. L., Agüeros, M. A., Cargile, P. A., Brewer, J. M., Meibom, S., & Jansen, T. 2019, ApJ, 879, 100

Dungee, R. 2022, in Fifty Years of the Skumanich Relations, ed. T. S. Metcalfe, 32

Edvardsson, B., Andersen, J., Gustafsson, B., Lambert, D. L., Nissen, P. E., & Tomkin, J. 1993, A&A, 500, 391

Eisenstein, D. J., Weinberg, D. H., Agol, E., Aihara, H., Allende Prieto, C., Anderson, S. F., Arns, J. A., Aubourg, É., Bailey, S., Balbinot, E., & et al. 2011, AJ, 142, 72

Epstein, C. R. & Pinsonneault, M. H. 2014, ApJ, 780, 159

Ester, M., Kriegel, H.-P., Sander, J., & Xu, X. 1996, in Proceedings of the Second International Conference on Knowledge Discovery and Data Mining, KDD'96 (AAAI Press), 226–231

Feiden, G., Guinan, E., Boyajian, T., Kok, Y., Basturk, O., Roberson, A., & Ribas, I. 2011, in American Astronomical Society Meeting Abstracts, Vol. 217, American Astronomical Society Meeting Abstracts #217, 140.18

Feinstein, A. D., Montet, B. T., Ansdell, M., Nord, B., Bean, J. L., Günther, M. N., Gully-Santiago, M. A., & Schlieder, J. E. 2020, AJ, 160, 219

Feinstein, A. D., Montet, B. T., Foreman-Mackey, D., Bedell, M. E., Saunders, N., Bean, J. L., Christiansen, J. L., Hedges, C., Luger, R., Scolnic, D., & Cardoso, J. V. d. M. 2019, PASP, 131, 094502

Feltzing, S. & Gustafsson, B. 1998, Astronomy and Astrophysics Supplement Series, 129, 237

Feltzing, S., Howes, L. M., McMillan, P. J., & Stonkutė, E. 2017, MNRAS, 465, L109

Ferguson, J. W., Alexander, D. R., Allard, F., Barman, T., Bodnarik, J. G., Hauschildt, P. H., Heffner-Wong, A., & Tamanai, A. 2005, ApJ, 623, 585

Fleming, D. P., Barnes, R., Davenport, J. R. A., & Luger, R. 2019, arXiv e-prints

Flesch, E. W. 2015, Publ. Astron. Soc. Aust., 32, e010

Foreman-Mackey, D., Hogg, D. W., Lang, D., & Goodman, J. 2013, PASP, 125, 306

Gaia Collaboration, Brown, A. G. A., Vallenari, A., Prusti, T., de Bruijne, J. H. J., Babusiaux, C., Bailer-Jones, C. A. L., Biermann, M., Evans, D. W., Eyer, L., Jansen, F., Jordi, C., Klioner, S. A., Lammers, U., Lindegren, L., Luri, X., Mignard, F., Panem, C., Pourbaix, D., Randich, S., Sartoretti, P., Siddiqui, H. I., Soubiran, C., van Leeuwen, F., Walton, N. A., Arenou, F., Bastian, U., Cropper, M., Drimmel, R., Katz, D., Lattanzi, M. G., Bakker, J., Cacciari, C., Castañeda, J., Chaoul, L., Cheek, N., De Angeli, F., Fabricius, C., Guerra, R., Holl, B., Masana, E., Messineo, R., Mowlavi, N., Nienartowicz, K., Panuzzo, P., Portell, J., Riello, M., Seabroke, G. M., Tanga, P., Thévenin, F., Gracia-Abril, G., Comoretto, G., Garcia-Reinaldos, M., Teyssier, D., Altmann, M., Andrae, R., Audard, M., Bellas-Velidis, I., Benson, K., Berthier, J., Blomme, R., Burgess, P., Busso, G., Carry, B., Cellino, A., Clementini, G., Clotet, M., Creevey, O., Davidson, M., De Ridder, J., Delchambre, L., Dell'Oro, A., Ducourant, C., Fernández-Hernández, J., Fouesneau, M., Frémat, Y., Galluccio, L., García-Torres, M., González-Núñez, J., González-Vidal, J. J., Gosset, E., Guy, L. P., Halbwachs, J. L., Hambly, N. C., Harrison, D. L., Hernández, J., Hestroffer, D., Hodgkin, S. T., Hutton, A., Jasniewicz, G., Jean-Antoine-Piccolo, A., Jordan, S., Korn, A. J., Krone-Martins, A., Lanzafame, A. C., Lebzelter, T., Löffler, W., Manteiga, M., Marrese, P. M., Martín-Fleitas, J. M., Moitinho, A., Mora, A., Muinonen, K., Osinde, J., Pancino, E., Pauwels, T., Petit, J. M., Recio-Blanco, A., Richards, P. J., Rimoldini, L., Robin, A. C., Sarro, L. M., Siopis, C., Smith, M., Sozzetti, A., Süveges, M., Torra, J., van Reeven, W., Abbas, U., Abreu Aramburu, A., Accart, S., Aerts, C., Altavilla, G., Álvarez, M. A., Alvarez, R., Alves, J., Anderson, R. I., Andrei, A. H., Anglada Varela, E., Antiche, E., Antoja, T., Arcay, B., Astraatmadja, T. L., Bach, N., Baker, S. G., Balaguer-Núñez, L., Balm, P., Barache, C., Barata, C., Barbato, D., Barblan, F., Barklem, P. S., Barrado, D., Barros, M., Barstow, M. A., Bartholomé Muñoz, S., Bassilana, J. L., Becciani, U., Bellazzini, M., Berihuete, A., Bertone, S., Bianchi, L., Bienaymé, O., Blanco-Cuaresma, S., Boch, T., Boeche, C., Bombrun, A., Borrachero, R., Bossini, D., Bouquillon, S., Bourda, G., Bragaglia, A., Bramante, L., Breddels, M. A., Bressan, A., Brouillet, N., Brüsemeister, T., Brugaletta, E., Bucciarelli, B., Burlacu, A., Busonero, D., Butkevich, A. G., Buzzi, R., Caffau, E., Cancelliere, R., Cannizzaro, G., Cantat-Gaudin, T., Carballo, R., Carlucci, T., Carrasco, J. M., Casamiquela, L., Castellani, M., Castro-Ginard, A., Charlot, P., Chemin, L., Chiavassa, A., Cocozza, G., Costigan, G., Cowell, S., Crifo, F., Crosta, M., Crowley, C., Cuypers, J., Dafonte, C., Damerdji, Y., Dapergolas, A., David, P., David, M., de Laverny, P., De Luise, F., De March, R., de Martino, D., de Souza, R., de Torres, A., Debosscher, J., del Pozo, E., Delbo, M., Delgado, A., Delgado, H. E., Di Matteo, P., Diakite, S., Diener, C., Distefano, E., Dolding, C., Drazinos, P., Durán, J., Edvardsson, B., Enke, H., Eriksson, K., Esquej, P., Eynard Bontemps, G., Fabre, C., Fabrizio, M., Faigler, S., Falcão, A. J., Farràs Casas, M., Federici, L., Fedorets, G., Fernique, P., Figueras, F., Filippi, F., Findeisen, K., Fonti, A., Fraile, E., Fraser, M., Frézouls, B., Gai, M., Galleti, S., Garabato, D., García-Sedano, F., Garofalo, A., Garralda, N., Gavel, A., Gavras, P., Gerssen, J., Geyer, R., Giacobbe, P., Gilmore, G., Girona, S., Giuffrida, G., Glass, F., Gomes, M., Granvik, M., Gueguen, A., Guerrier, A., Guiraud, J., Gutiérrez-Sánchez, R., Haigron, R., Hatzidimitriou, D., Hauser, M., Haywood, M., Heiter, U., Helmi, A., Heu, J., Hilger, T., Hobbs, D., Hofmann, W., Holland, G., Huckle, H. E., Hypki, A., Icardi, V., Janßen, K., Jevardat de Fombelle, G., Jonker, P. G., Juhász, Á. L., Julbe, F., Karampelas, A., Kewley, A., Klar, J., Kochoska, A., Kohley, R., Kolenberg, K., Kontizas, M., Kontizas, E., Koposov, S. E., Kordopatis, G., Kostrzewa-Rutkowska, Z., Koubsky, P., Lambert, S., Lanza, A. F., Lasne, Y., Lavigne, J. B., Le Fustec, Y., Le Poncin-Lafitte, C., Lebreton, Y., Leccia, S., Leclerc, N., Lecoeur-Taibi, I., Lenhardt, H., Leroux, F., Liao, S., Licata, E., Lindstrøm, H. E. P., Lister, T. A., Livanou, E., Lobel, A., López, M., Managau, S., Mann, R. G., Mantelet, G., Marchal, O., Marchant, J. M., Marconi, M., Marinoni, S., Marschalkó, G., Marshall, D. J., Martino, M., Marton, G., Mary, N., Massari, D., Matijevič, G., Mazeh, T., McMillan, P. J., Messina, S., Michalik, D., Millar, N. R., Molina, D., Molinaro, R., Molnár, L., Montegriffo, P., Mor, R., Morbidelli, R., Morel, T., Morris, D., Mulone, A. F., Muraveva, T., Musella, I., Nelemans, G., Nicastro, L., Noval, L., O'Mullane, W., Ordénovic, C., Ordóñez-Blanco, D., Osborne, P., Pagani, C., Pagano, I., Pailler, F., Palacin, H., Palaversa, L., Panahi, A., Pawlak, M., Piersimoni, A. M., Pineau, F. X., Plachy, E., Plum, G., Poggio, E., Poujoulet, E., Prša, A., Pulone, L., Racero, E., Ragaini, S., Rambaux, N., Ramos-Lerate, M., Regibo, S., Reylé, C., Riclet, F., Ripepi, V., Riva, A., Rivard, A., Rixon, G., Roegiers, T., Roelens, M., Romero-Gómez, M., Rowell, N., Royer, F., Ruiz-Dern, L., Sadowski, G., Sagristà Sellés, T., Sahlmann, J., Salgado, J., Salguero, E., Sanna, N., Santana-Ros, T., Sarasso, M., Savietto, H., Schultheis, M., Sciacca, E., Segol, M., Segovia, J. C., Ségransan, D., Shih, I. C., Siltala, L., Silva, A. F., Smart, R. L., Smith, K. W., Solano, E., Solitro, F., Sordo, R., Soria Nieto, S., Souchay, J., Spagna, A., Spoto, F., Stampa, U., Steele, I. A., Steidelmüller, H., Stephenson, C. A., Stoev, H., Suess, F. F., Surdej, J., Szabados, L., Szegedi-Elek, E., Tapiador, D., Taris, F., Tauran, G., Taylor, M. B., Teixeira, R., Terrett, D., Teyssand ier, P., Thuillot, W., Titarenko, A., Torra Clotet, F., Turon, C., Ulla, A., Utrilla, E., Uzzi, S., Vaillant, M., Valentini, G., Valette, V., van Elteren, A., Van Hemelryck, E., van Leeuwen, M., Vaschetto, M., Vecchiato, A., Veljanoski, J., Viala, Y., Vicente, D., Vogt, S., von Essen, C., Voss, H., Votruba, V., Voutsinas, S., Walmsley, G., Weiler, M., Wertz, O., Wevers, T., Wyrzykowski, Ł., Yoldas, A., Žerjal, M., Ziaeepour, H., Zorec, J., Zschocke, S., Zucker, S., Zurbach, C., & Zwitter, T. 2018, A&A, 616, A1

Gallet, F. & Bouvier, J. 2015, A&A, 577, A98

García, R. A., Ceillier, T., Salabert, D., Mathur, S., van Saders, J. L., Pinsonneault, M., Ballot, J., Beck, P. G., Bloemen, S., Campante, T. L., Davies, G. R., do Nascimento, J. D., J., Mathis, S., Metcalfe, T. S., Nielsen, M. B., Suárez, J. C., Chaplin, W. J., Jiménez, A., & Karoff, C. 2014a, A&A, 572, A34

García, R. A., Hekker, S., Stello, D., Gutiérrez-Soto, J., Handberg, R., Huber, D., Karoff, C., Uytterhoeven, K., Appourchaux, T., Chaplin, W. J., Elsworth, Y., Mathur, S., Ballot, J., Christensen-Dalsgaard, J., Gilliland, R. L., Houdek, G., Jenkins, J. M., Kjeldsen, H., McCauliff, S., Metcalfe, T., Middour, C. K., Molenda-Zakowicz, J., Monteiro, M. J. P. F. G., Smith, J. C., & Thompson, M. J. 2011, MNRAS, 414, L6

García, R. A., Mathur, S., Pires, S., Régulo, C., Bellamy, B., Pallé, P. L., Ballot, J., Barceló Forteza, S., Beck, P. G., & Bedding, T. R. 2014b, A&A, 568, A10

García Pérez, A. E., Allende Prieto, C., Holtzman, J. A., Shetrone, M., Mészáros, S., Bizyaev, D., Carrera, R., Cunha, K., García-Hernández, D. A., Johnson, J. A., Majewski, S. R., Nidever, D. L., Schiavon, R. P., Shane, N., Smith, V. V., Sobeck, J., Troup, N., Zamora, O., Weinberg, D. H., Bovy, J., Eisenstein, D. J., Feuillet, D., Frinchaboy, P. M., Hayden, M. R., Hearty, F. R., Nguyen, D. C., O'Connell, R. W., Pinsonneault, M. H., Wilson, J. C., & Zasowski, G. 2016, AJ, 151, 144

Gilbert, E. A., Barclay, T., Schlieder, J. E., Quintana, E. V., Hord, B. J., Kostov, V. B., Lopez, E. D., Rowe, J. F., Hoffman, K., Walkowicz, L. M., Silverstein, M. L., Rodriguez, J. E., Vanderburg, A., Suissa, G., Airapetian, V. S., Clement, M. S., Raymond, S. N., Mann, A. W., Kruse, E., Lissauer, J. J., Colón, K. D., Kopparapu, R. k., Kreidberg, L., Zieba, S., Collins, K. A., Quinn, S. N., Howell, S. B., Ziegler, C., Vrijmoet, E. H., Adams, F. C., Arney, G. N., Boyd, P. T., Brande, J., Burke, C. J., Cacciapuoti, L., Chance, Q., Christiansen, J. L., Covone, G., Daylan, T., Dineen, D., Dressing, C. D., Essack, Z., Fauchez, T. J., Galgano, B., Howe, A. R., Kaltenegger, L., Kane, S. R., Lam, C., Lee, E. J., Lewis, N. K., Logsdon, S. E., Mandell, A. M., Monsue, T., Mullally, F., Mullally, S. E., Paudel, R. R., Pidhorodetska, D., Plavchan, P., Reyes, N. T., Rinehart, S. A., Rojas-Ayala, B., Smith, J. C., Stassun, K. G., Tenenbaum, P., Vega, L. D., Villanueva, G. L., Wolf, E. T., Youngblood, A., Ricker, G. R., Vanderspek, R. K., Latham, D. W., Seager, S., Winn, J. N., Jenkins, J. M., Bakos, G. Å., Briceño, C., Ciardi, D. R., Cloutier, R., Conti, D. M., Couperus, A., Di Sora, M., Eisner, N. L., Everett, M. E., Gan, T., Hartman, J. D., Henry, T., Isopi, G., Jao, W.-C., Jensen, E. L. N., Law, N., Mallia, F., Matson, R. A., Shappee, B. J., Le Wood, M., & Winters, J. G. 2020, AJ, 160, 116

Gondoin, P. 2008, A&A, 478, 883

Goodfellow, I., Bengio, Y., & Courville, A. 2016, Deep Learning (MIT Press), `http://www.deeplearningbook.org`

Gordon, T. A., Davenport, J. R. A., Angus, R., Foreman-Mackey, D., Agol, E., Covey, K. R., Agüeros, M. A., & Kipping, D. 2021, ApJ, 913, 70

Grevesse, N. & Sauval, A. J. 1998, Space Sci. Rev., 85, 161

Guiglion, G., Matijevič, G., Queiroz, A. B. A., Valentini, M., Steinmetz, M., Chiappini, C., Grebel, E. K., McMillan, P. J., Kordopatis, G., Kunder, A., Zwitter, T., Khalatyan, A., Anders, F., Enke, H., Minchev, I., Monari, G., Wyse, R. F. G., Bienaymé, O., Bland-Hawthorn, J., Gibson, B. K., Navarro, J. F., Parker, Q., Reid, W., Seabroke, G. M., & Siebert, A. 2020, A&A, 644, A168

Hall, O. J., Davies, G. R., van Saders, J., Nielsen, M. B., Lund, M. N., Chaplin, W. J., García, R. A., Amard, L., Breimann, A. A., Khan, S., See, V., & Tayar, J. 2021, Nature Astronomy, 5, 707

Handberg, R., Lund, M. N., White, T. R., Hall, O. J., Buzasi, D. L., Pope, B. J. S., Hansen, J. S., von Essen, C., Carboneau, L., Huber, D., Vanderspek, R. K., Fausnaugh, M. M., Tenenbaum, P., Jenkins, J. M., & T'DA Collaboration. 2021, AJ, 162, 170

Hartman, J. D., Bakos, G. Á., Noyes, R. W., Sipőcz, B., Kovács, G., Mazeh, T., Shporer, A., & Pál, A. 2011, AJ, 141, 166

Hartman, J. D., Gaudi, B. S., Pinsonneault, M. H., Stanek, K. Z., Holman, M. J., McLeod, B. A., Meibom, S., Barranco, J. A., & Kalirai, J. S. 2009, ApJ, 691, 342

Hathaway, D. H. 2011, Sol. Phys., 273, 221

—. 2015, Living Reviews in Solar Physics, 12, 4

Hathaway, D. H., Wilson, R. M., & Reichmann, E. J. 1994, Sol. Phys., 151, 177

Hattori, S., Foreman-Mackey, D., Hogg, D. W., Montet, B. T., Angus, R., Pritchard, T. A., Curtis, J. L., & Schölkopf, B. 2022, AJ, 163, 284

Hayden, M. R., Bovy, J., Holtzman, J. A., Nidever, D. L., Bird, J. C., Weinberg, D. H., Andrews, B. H., Majewski, S. R., Allende Prieto, C., Anders, F., Beers, T. C., Bizyaev, D., Chiappini, C., Cunha, K., Frinchaboy, P., García-Herńand ez, D. A., García Pérez, A. E., Girardi, L., Harding, P., Hearty, F. R., Johnson, J. A., Mészáros, S., Minchev, I., O'Connell, R., Pan, K., Robin, A. C., Schiavon, R. P., Schneider, D. P., Schultheis, M., Shetrone, M., Skrutskie, M., Steinmetz, M., Smith, V., Wilson, J. C., Zamora, O., & Zasowski, G. 2015, ApJ, 808, 132

Haywood, M., Di Matteo, P., Lehnert, M. D., Katz, D., & Gómez, A. 2013, A&A, 560, A109

He, K., Zhang, X., Ren, S., & Sun, J. 2015, arXiv e-prints, arXiv:1512.03385

Hedges, C., Angus, R., Barentsen, G., Saunders, N., Montet, B. T., & Gully-Santiago, M. 2020, Research Notes of the American Astronomical Society, 4, 220

Hezaveh, Y. D., Perreault Levasseur, L., & Marshall, P. J. 2017, Nature, 548, 555

Holcomb, R. 2020, in American Astronomical Society Meeting Abstracts, American Astronomical Society Meeting Abstracts, 274.04

Holcomb, R. J., Robertson, P., Hartigan, P., Oelkers, R. J., & Robinson, C. 2022, arXiv e-prints, arXiv:2206.10629

Holtzman, J. A., Hasselquist, S., Shetrone, M., Cunha, K., Allende Prieto, C., Anguiano, B., Bizyaev, D., Bovy, J., Casey, A., Edvardsson, B., Johnson, J. A., Jönsson, H., Meszaros, S., Smith, V. V., Sobeck, J., Zamora, O., Chojnowski, S. D., Fernandez-Trincado, J., Garcia-Hernandez, D. A., Majewski, S. R., Pinsonneault, M., Souto, D., Stringfellow, G. S., Tayar, J., Troup, N., & Zasowski, G. 2018, AJ, 156, 125

Hon, M., Stello, D., García, R. A., Mathur, S., Sharma, S., Colman, I. L., & Bugnet, L. 2019, MNRAS

Huang, C. X., Vanderburg, A., Pál, A., Sha, L., Yu, L., Fong, W., Fausnaugh, M., Shporer, A., Guerrero, N., Vanderspek, R., & Ricker, G. 2020a, Research Notes of the American Astronomical Society, 4, 204

—. 2020b, Research Notes of the American Astronomical Society, 4, 206

Huber, D., Bryson, S. T., Haas, M. R., Barclay, T., Barentsen, G., Howell, S. B., Sharma, S., Stello, D., & Thompson, S. E. 2016, The Astrophysical Journal Supplement Series, 224, 2

Irwin, J. & Bouvier, J. 2009, in The Ages of Stars, ed. E. E. Mamajek, D. R. Soderblom, & R. F. G. Wyse, Vol. 258, 363–374

Jenkins, J. M., Twicken, J. D., McCauliff, S., Campbell, J., Sanderfer, D., Lung, D., Mansouri-Samani, M., Girouard, F., Tenenbaum, P., Klaus, T., Smith, J. C., Caldwell, D. A., Chacon, A. D., Henze, C., Heiges, C., Latham, D. W., Morgan, E., Swade, D., Rinehart, S., & Vanderspek, R. 2016, in Society of Photo-Optical Instrumentation

Engineers (SPIE) Conference Series, Vol. 9913, Software and Cyberinfrastructure for Astronomy IV, ed. G. Chiozzi & J. C. Guzman, 99133E

Johnson, D. R. H. & Soderblom, D. R. 1987, AJ, 93, 864

Jönsson, H., Holtzman, J. A., Allende Prieto, C., Cunha, K., García-Hernández, D. A., Hasselquist, S., Masseron, T., Osorio, Y., Shetrone, M., Smith, V., Stringfellow, G. S., Bizyaev, D., Edvardsson, B., Majewski, S. R., Mészáros, S., Souto, D., Zamora, O., Beaton, R. L., Bovy, J., Donor, J., Pinsonneault, M. H., Poovelil, V. J., & Sobeck, J. 2020, AJ, 160, 120

Karoff, C., Metcalfe, T. S., Santos, Â. R. G., Montet, B. T., Isaacson, H., Witzke, V., Shapiro, A. I., Mathur, S., Davies, G. R., Lund, M. N., Garcia, R. A., Brun, A. S., Salabert, D., Avelino, P. P., van Saders, J., Egeland, R., Cunha, M. S., Campante, T. L., Chaplin, W. J., Krivova, N., Solanki, S. K., Stritzinger, M., & Knudsen, M. F. 2018, ApJ, 852, 46

Kawaler, S. D. 1988, ApJ, 333, 236

Kingma, D. P. & Ba, J. 2014, arXiv e-prints, arXiv:1412.6980

Kjeldsen, H. & Bedding, T. R. 1995, A&A, 293, 87

Kochanek, C. S., Shappee, B. J., Stanek, K. Z., Holoien, T. W. S., Thompson, T. A., Prieto, J. L., Dong, S., Shields, J. V., Will, D., Britt, C., Perzanowski, D., & Pojmański, G. 2017, PASP, 129, 104502

Kraft, R. P. 1967, ApJ, 150, 551

Krishnamurthi, A., Pinsonneault, M. H., Barnes, S., & Sofia, S. 1997, ApJ, 480, 303

Kunimoto, M., Huang, C., Tey, E., Fong, W., Hesse, K., Shporer, A., Guerrero, N., Fausnaugh, M., Vanderspek, R., & Ricker, G. 2021, Research Notes of the American Astronomical Society, 5, 234

Lanzafame, A. C. & Spada, F. 2015, A&A, 584, A30

Lightkurve Collaboration. 2020, How to remove scattered light from TESS data using the `RegressionCorrector`?, `https://docs.lightkurve.org/tutorials/04-how-to-remove-tess-scattered-light-using-regressioncorrector.html`

Lightkurve Collaboration, Cardoso, J. V. d. M., Hedges, C., Gully-Santiago, M., Saunders, N., Cody, A. M., Barclay, T., Hall, O., Sagear, S., Turtelboom, E., Zhang, J., Tzanidakis, A., Mighell, K., Coughlin, J., Bell, K., Berta-Thompson, Z., Williams, P., Dotson, J., & Barentsen, G. 2018, Lightkurve: Kepler and TESS time series analysis in Python, Astrophysics Source Code Library

Lindegren, L., Hernández, J., Bombrun, A., Klioner, S., Bastian, U., Ramos-Lerate, M., de Torres, A., Steidelmüller, H., Stephenson, C., Hobbs, D., Lammers, U., Biermann, M., Geyer, R., Hilger, T., Michalik, D., Stampa, U., McMillan, P. J., Castañeda, J., Clotet, M., Comoretto, G., Davidson, M., Fabricius, C., Gracia, G., Hambly, N. C., Hutton, A., Mora, A., Portell, J., van Leeuwen, F., Abbas, U., Abreu, A., Altmann, M., Andrei, A., Anglada, E., Balaguer-Núñez, L., Barache, C., Becciani, U., Bertone, S., Bianchi, L., Bouquillon, S., Bourda, G., Brüsemeister, T., Bucciarelli, B., Busonero, D., Buzzi, R., Cancelliere, R., Carlucci, T., Charlot, P., Cheek, N., Crosta, M., Crowley, C., de Bruijne, J., de Felice, F., Drimmel, R., Esquej, P., Fienga, A., Fraile, E., Gai, M., Garralda, N., González-Vidal, J. J., Guerra, R., Hauser, M., Hofmann, W., Holl, B., Jordan, S., Lattanzi, M. G., Lenhardt, H., Liao, S., Licata, E., Lister, T., Löffler, W., Marchant, J., Martin-Fleitas, J.-M., Messineo, R., Mignard, F., Morbidelli, R., Poggio, E., Riva, A., Rowell, N., Salguero, E., Sarasso, M., Sciacca, E., Siddiqui, H., Smart, R. L., Spagna, A., Steele, I., Taris, F., Torra, J., van Elteren, A., van Reeven, W., & Vecchiato, A. 2018, A&A, 616, A2

Liu, Y., San Liang, X., & Weisberg, R. H. 2007, Journal of Atmospheric and Oceanic Technology, 24, 2093

Llama, J., Jardine, M., Mackay, D. H., & Fares, R. 2012, MNRAS, 422, L72

Lomb, N. R. 1976, Ap&SS, 39, 447

Lu, Y. L., Angus, R., Agüeros, M. A., Blancato, K., Ness, M., Rowland, D., Curtis, J. L., & Grunblatt, S. 2020, AJ, 160, 168

Lund, M. N., Handberg, R., Buzasi, D. L., Carboneau, L., Hall, O. J., Pereira, F., Huber, D., Hey, D., Van Reeth, T., & T'DA Collaboration. 2021, ApJS, 257, 53

MacGregor, K. B. & Brenner, M. 1991, ApJ, 376, 204

Mackay, D. H., Jardine, M., Collier Cameron, A., Donati, J. F., & Hussain, G. A. J. 2004, MNRAS, 354, 737

Maeder, A. & Meynet, G. 2000, ARA&A, 38, 143

Majewski, S. R., Schiavon, R. P., Frinchaboy, P. M., Allende Prieto, C., Barkhouser, R., Bizyaev, D., Blank, B., Brunner, S., Burton, A., Carrera, R., Chojnowski, S. D., Cunha, K., Epstein, C., Fitzgerald, G., García Pérez, A. E., Hearty, F. R., Henderson, C., Holtzman, J. A., Johnson, J. A., Lam, C. R., Lawler, J. E., Maseman, P., Mészáros, S., Nelson, M., Nguyen, D. C., Nidever, D. L., Pinsonneault, M., Shetrone, M., Smee, S., Smith, V. V., Stolberg, T., Skrutskie, M. F., Walker, E., Wilson, J. C., Zasowski, G., Anders, F., Basu, S., Beland, S., Blanton, M. R., Bovy, J., Brownstein, J. R., Carlberg, J., Chaplin, W., Chiappini, C., Eisenstein, D. J., Elsworth, Y., Feuillet, D., Fleming, S. W., Galbraith-Frew, J., García, R. A., García-Hernández, D. A., Gillespie, B. A., Girardi, L., Gunn, J. E., Hasselquist, S., Hayden, M. R., Hekker, S., Ivans, I., Kinemuchi, K., Klaene, M., Mahadevan, S., Mathur, S., Mosser, B., Muna, D., Munn, J. A., Nichol, R. C., O'Connell, R. W., Parejko, J. K., Robin, A. C., Rocha-Pinto, H., Schultheis, M., Serenelli, A. M., Shane, N., Silva Aguirre, V., Sobeck, J. S., Thompson, B., Troup, N. W., Weinberg, D. H., & Zamora, O. 2017, AJ, 154, 94

Mamajek, E. E. & Hillenbrand, L. A. 2008, ApJ, 687, 1264

Mann, A. W., Gaidos, E., Lépine, S., & Hilton, E. J. 2012, ApJ, 753, 90

Maoz, D., Mannucci, F., Li, W., Filippenko, A. V., Della Valle, M., & Panagia, N. 2011, MNRAS, 412, 1508

Marilli, E., Frasca, A., Covino, E., Alcalá, J. M., Catalano, S., Fernández, M., Arellano Ferro, A., Rubio-Herrera, E., & Spezzi, L. 2007, A&A, 463, 1081

Martig, M., Fouesneau, M., Rix, H.-W., Ness, M., Mészáros, S., García-Hernández, D. A., Pinsonneault, M., Serenelli, A., Silva Aguirre, V., & Zamora, O. 2016, MNRAS, 456, 3655

Martig, M., Rix, H.-W., Silva Aguirre, V., Hekker, S., Mosser, B., Elsworth, Y., Bovy, J., Stello, D., Anders, F., García, R. A., Tayar, J., Rodrigues, T. S., Basu, S., Carrera, R., Ceillier, T., Chaplin, W. J., Chiappini, C., Frinchaboy, P. M., García-Hernández, D. A., Hearty, F. R., Holtzman, J., Johnson, J. A., Majewski, S. R., Mathur, S., Mészáros, S., Miglio, A., Nidever, D., Pan, K., Pinsonneault, M., Schiavon, R. P., Schneider, D. P., Serenelli, A., Shetrone, M., & Zamora, O. 2015, MNRAS, 451, 2230

Masuda, K., Petigura, E. A., & Hall, O. J. 2022, MNRAS, 510, 5623

Mathur, S., García, R. A., Régulo, C., Creevey, O. L., Ballot, J., Salabert, D., Arentoft, T., Quirion, P. O., Chaplin, W. J., & Kjeldsen, H. 2010, A&A, 511, A46

Mathur, S., Huber, D., Batalha, N. M., Ciardi, D. R., Bastien, F. A., Bieryla, A., Buchhave, L. A., Cochran, W. D., Endl, M., Esquerdo, G. A., Furlan, E., Howard, A., Howell, S. B., Isaacson, H., Latham, D. W., MacQueen, P. J., & Silva, D. R. 2017, ApJS, 229, 30

Matt, S. & Pudritz, R. E. 2008, ApJ, 678, 1109

Matt, S. P., Brun, A. S., Baraffe, I., Bouvier, J., & Chabrier, G. 2015, ApJ, 799, L23

Matt, S. P., MacGregor, K. B., Pinsonneault, M. H., & Greene, T. P. 2012, ApJ, 754, L26

McQuillan, A., Aigrain, S., & Mazeh, T. 2013, MNRAS, 432, 1203

McQuillan, A., Mazeh, T., & Aigrain, S. 2014, ApJS, 211, 24

Meibom, S., Barnes, S. A., Latham, D. W., Batalha, N., Borucki, W. J., Koch, D. G., Basri, G., Walkowicz, L. M., Janes, K. A., Jenkins, J., Van Cleve, J., Haas, M. R., Bryson, S. T., Dupree, A. K., Furesz, G., Szentgyorgyi, A. H., Buchhave, L. A., Clarke, B. D., Twicken, J. D., & Quintana, E. V. 2011, ApJ, 733, L9

Meibom, S., Barnes, S. A., Platais, I., Gilliland, R. L., Latham, D. W., & Mathieu, R. D. 2015, Nature, 517, 589

Mendoza, C., Seaton, M. J., Buerger, P., Bellorín, A., Meléndez, M., González, J., Rodríguez, L. S., Delahaye, F., Palacios, E., Pradhan, A. K., & Zeippen, C. J. 2007, MNRAS, 378, 1031

Montalto, M., Borsato, L., Granata, V., Lacedelli, G., Malavolta, L., Manthopoulou, E. E., Nardiello, D., Nascimbeni, V., & Piotto, G. 2020, MNRAS, 498, 1726

Netto, Y. & Valio, A. 2020, A&A, 635, A78

Newton, E. R., Irwin, J., Charbonneau, D., Berta-Thompson, Z. K., Dittmann, J. A., & West, A. A. 2016, ApJ, 821, 93

Newton, E. R., Mondrik, N., Irwin, J., Winters, J. G., & Charbonneau, D. 2018, AJ, 156, 217

Nielsen, M. B., Gizon, L., Cameron, R. H., & Miesch, M. 2019, A&A, 622, A85

Nomoto, K., Kobayashi, C., & Tominaga, N. 2013, Annual Review of Astronomy and Astrophysics, 51, 457

Nordström, B., Mayor, M., Andersen, J., Holmberg, J., Pont, F., Jørgensen, B. R., Olsen, E. H., Udry, S., & Mowlavi, N. 2004, A&A, 418, 989

Oelkers, R. J., Rodriguez, J. E., Stassun, K. G., Pepper, J., Somers, G., Kafka, S., Stevens, D. J., Beatty, T. G., Siverd, R. J., Lund, M. B., Kuhn, R. B., James, D., & Gaudi, B. S. 2018, AJ, 155, 39

Oelkers, R. J. & Stassun, K. G. 2018, AJ, 156, 132

Pepper, J., Pogge, R. W., DePoy, D. L., Marshall, J. L., Stanek, K. Z., Stutz, A. M., Poindexter, S., Siverd, R., O'Brien, T. P., Trueblood, M., & Trueblood, P. 2007, PASP, 119, 923

Pinsonneault, M. 1997, ARA&A, 35, 557

Pires, S., Mathur, S., García, R. A., Ballot, J., Stello, D., & Sato, K. 2015, A&A, 574, A18

Pizzolato, N., Maggio, A., Micela, G., Sciortino, S., & Ventura, P. 2003, A&A, 397, 147

Pont, F. & Eyer, L. 2004, MNRAS, 351, 487

Powell, B. P., Kruse, E., Montet, B. T., Feinstein, A. D., Lewis, H. M., Foreman-Mackey, D., Barclay, T., Quintana, E. V., Colón, K. D., Kostov, V. B., Boyd, P., Smale, A. P., Mullally, S. E., Schlieder, J. E., Schnittman, J. D., Carroll, M. L., Carriere, L. E., Salmon, E. M., Strong, S. L., Acks, N. D., Pfaff, B. E., Gerner, L. E., & Burch, T. M. 2022, Research Notes of the American Astronomical Society, 6, 111

Rebull, L. M., Stauffer, J. R., Bouvier, J., Cody, A. M., Hillenbrand, L. A., Soderblom, D. R., Valenti, J., Barrado, D., Bouy, H., Ciardi, D., Pinsonneault, M., Stassun, K., Micela, G., Aigrain, S., Vrba, F., Somers, G., Christiansen, J., Gillen, E., & Collier Cameron, A. 2016, AJ, 152, 113

Rebull, L. M., Stauffer, J. R., Hillenbrand, L. A., Cody, A. M., Bouvier, J., Soderblom, D. R., Pinsonneault, M., & Hebb, L. 2017, ApJ, 839, 92

Reinhold, T., Bell, K. J., Kuszlewicz, J., Hekker, S., & Shapiro, A. I. 2019, A&A, 621, A21

Reinhold, T. & Hekker, S. 2020, A&A, 635, A43

Ricker, G. R., Winn, J. N., Vanderspek, R., Latham, D. W., Bakos, G. Á., Bean, J. L., Berta-Thompson, Z. K., Brown, T. M., Buchhave, L., Butler, N. R., Butler, R. P., Chaplin, W. J., Charbonneau, D., Christensen-Dalsgaard, J., Clampin, M., Deming, D., Doty, J., De Lee, N., Dressing, C., Dunham, E. W., Endl, M., Fressin, F., Ge, J., Henning, T., Holman, M. J., Howard, A. W., Ida, S., Jenkins, J. M., Jernigan, G., Johnson, J. A., Kaltenegger, L., Kawai, N., Kjeldsen, H., Laughlin, G., Levine, A. M., Lin, D., Lissauer, J. J., MacQueen, P., Marcy, G., McCullough, P. R., Morton, T. D., Narita, N., Paegert, M., Palle, E., Pepe, F., Pepper, J., Quirrenbach, A., Rinehart, S. A., Sasselov, D., Sato, B., Seager, S., Sozzetti, A., Stassun, K. G., Sullivan, P., Szentgyorgyi, A., Torres, G., Udry, S., & Villasenor, J. 2015, Journal of Astronomical Telescopes, Instruments, and Systems, 1, 014003

Rogers, F. J. & Nayfonov, A. 2002, ApJ, 576, 1064

Rüdiger, G., Küker, M., Käpylä, P. J., & Strassmeier, K. G. 2019, A&A, 630, A109

Santana, F. A., Beaton, R. L., Covey, K. R., O'Connell, J. E., Longa-Peña, P., Cohen, R., Fernández-Trincado, J. G., Hayes, C. R., Zasowski, G., Sobeck, J. S., Majewski, S. R., Chojnowski, S. D., De Lee, N., Oelkers, R. J., Stringfellow, G. S., Almeida, A., Anguiano, B., Donor, J., Frinchaboy, P. M., Hasselquist, S., Johnson, J. A., Kollmeier, J. A., Nidever, D. L., Price-Whelan, A. M., Rojas-Arriagada, A., Schultheis, M., Shetrone, M., Simon, J. D., Aerts, C., Borissova, J., Drout, M. R., Geisler, D., Law, C. Y., Medina, N., Minniti, D., Monachesi, A., Muñoz, R. R., Poleski, R., Roman-Lopes, A., Schlaufman, K. C., Stutz, A. M., Teske, J., Tkachenko, A., Van Saders, J. L., Weinberger, A. J., & Zoccali, M. 2021, AJ, 162, 303

Santos, A. R. G., Breton, S. N., Mathur, S., & García, R. A. 2021, ApJS, 255, 17

Santos, A. R. G., García, R. A., Mathur, S., Bugnet, L., van Saders, J. L., Metcalfe, T. S., Simonian, G. V. A., & Pinsonneault, M. H. 2019, ApJS, 244, 21

Scargle, J. D. 1982, ApJ, 263, 835

Schofield, M., Chaplin, W. J., Huber, D., Campante, T. L., Davies, G. R., Miglio, A., Ball, W. H., Appourchaux, T., Basu, S., Bedding, T. R., Christensen-Dalsgaard, J., Creevey, O., García, R. A., Handberg, R., Kawaler, S. D., Kjeldsen, H., Latham, D. W., Lund, M. N., Metcalfe, T. S., Ricker, G. R., Serenelli, A., Silva Aguirre, V., Stello, D., & Vanderspek, R. 2019, ApJS, 241, 12

Schönrich, R., Binney, J., & Dehnen, W. 2010, MNRAS, 403, 1829

Schrijver, C. J. & Harvey, K. L. 1994, Sol. Phys., 150, 1

See, V., Roquette, J., Amard, L., & Matt, S. P. 2021, ApJ, 912, 127

Serenelli, A., Johnson, J., Huber, D., Pinsonneault, M., Ball, W. H., Tayar, J., Silva Aguirre, V., Basu, S., Troup, N., Hekker, S., Kallinger, T., Stello, D., Davies, G. R., Lund, M. N., Mathur, S., Mosser, B., Stassun, K. G., Chaplin, W. J., Elsworth, Y., García, R. A., Handberg, R., Holtzman, J., Hearty, F., García-Hernández, D. A., Gaulme, P., & Zamora, O. 2017, ApJS, 233, 23

Shappee, B. J., Prieto, J. L., Grupe, D., Kochanek, C. S., Stanek, K. Z., De Rosa, G., Mathur, S., Zu, Y., Peterson, B. M., Pogge, R. W., Komossa, S., Im, M., Jencson, J., Holoien, T. W. S., Basu, U., Beacom, J. F., Szczygieł, D. M., Brimacombe, J., Adams, S., Campillay, A., Choi, C., Contreras, C., Dietrich, M., Dubberley, M., Elphick, M., Foale, S., Giustini, M., Gonzalez, C., Hawkins, E., Howell, D. A., Hsiao, E. Y., Koss, M., Leighly, K. M., Morrell, N., Mudd, D., Mullins, D., Nugent, J. M., Parrent, J., Phillips, M. M., Pojmanski, G., Rosing, W., Ross, R., Sand, D., Terndrup, D. M., Valenti, S., Walker, Z., & Yoon, Y. 2014, ApJ, 788, 48

Sills, A., Pinsonneault, M. H., & Terndrup, D. M. 2000, ApJ, 534, 335

Silva Aguirre, V., Bojsen-Hansen, M., Slumstrup, D., Casagrande, L., Kawata, D., Ciucă, I., Handberg, R., Lund, M. N., Mosumgaard, J. R., Huber, D., Johnson, J. A., Pinsonneault, M. H., Serenelli, A. M., Stello, D., Tayar, J., Bird, J. C., Cassisi, S., Hon, M., Martig, M., Nissen, P. E., Rix, H. W., Schönrich, R., Sahlholdt, C., Trick, W. H., & Yu, J. 2018, MNRAS, 475, 5487

Simonian, G. V. A., Pinsonneault, M. H., & Terndrup, D. M. 2019, ApJ, 871, 174

Skumanich, A. 1972, ApJ, 171, 565

Smith, J. C., Morris, R. L., Jenkins, J. M., Bryson, S. T., Caldwell, D. A., & Girouard, F. R. 2016, Publications of the Astronomical Society of the Pacific, 128, 124501

Soderblom, D. R. 2010, Annual Review of Astronomy and Astrophysics, 48, 581

Soderblom, D. R., Jones, B. F., & Walker, M. F. 1983, ApJ, 274, L37

Somers, G. & Pinsonneault, M. H. 2016, ApJ, 829, 32

Spada, F. & Lanzafame, A. C. 2020, A&A, 636, A76

Stassun, K. G., Oelkers, R. J., Paegert, M., Torres, G., Pepper, J., De Lee, N., Collins, K., Latham, D. W., Muirhead, P. S., Chittidi, J., Rojas-Ayala, B., Fleming, S. W., Rose, M. E., Tenenbaum, P., Ting, E. B., Kane, S. R., Barclay, T., Bean, J. L., Brassuer, C. E., Charbonneau, D., Ge, J., Lissauer, J. J., Mann, A. W., McLean, B., Mullally, S., Narita, N., Plavchan, P., Ricker, G. R., Sasselov, D., Seager, S., Sharma, S., Shiao, B., Sozzetti, A., Stello, D., Vanderspek, R., Wallace, G., & Winn, J. N. 2019, AJ, 158, 138

Stauffer, J. R., Hartmann, L., Soderblom, D. R., & Burnham, N. 1984, ApJ, 280, 202

Stello, D., Huber, D., Bedding, T. R., Benomar, O., Bildsten, L., Elsworth, Y. P., Gilliland, R. L., Mosser, B., Paxton, B., & White, T. R. 2013, ApJ, 765, L41

Tayar, J., Ceillier, T., García-Hernández, D. A., Troup, N. W., Mathur, S., García, R. A., Zamora, O., Johnson, J. A., Pinsonneault, M. H., Mészáros, S., Allende Prieto, C., Chaplin, W. J., Elsworth, Y., Hekker, S., Nidever, D. L., Salabert, D., Schneider, D. P., Serenelli, A., Shetrone, M., & Stello, D. 2015, ApJ, 807, 82

Tayar, J. & Pinsonneault, M. H. 2018, ApJ, 868, 150

Thomas, A. E. L., Chaplin, W. J., Davies, G. R., Howe, R., Santos, Á. R. G., Elsworth, Y., Miglio, A., Campante, T., & Cunha, M. S. 2019, MNRAS, 485, 3857

Torrence, C. & Compo, G. 1998, A practical guide to wavelet analysis, B. Am. Meteorol. Soc., 79, 61–78

Tucci Maia, M., Ramírez, I., Meléndez, J., Bedell, M., Bean, J. L., & Asplund, M. 2016, A&A, 590, A32

van Ballegooijen, A. A., Cartledge, N. P., & Priest, E. R. 1998, ApJ, 501, 866

van der Walt, S., Schönberger, J. L., Nunez-Iglesias, J., Boulogne, F., Warner, J. D., Yager, N., Gouillart, E., Yu, T., & scikit-image Contributors. 2014, PeerJ, 2, e453

van Saders, J. L., Ceillier, T., Metcalfe, T. S., Silva Aguirre, V., Pinsonneault, M. H., García, R. A., Mathur, S., & Davies, G. R. 2016, Nature, 529, 181

van Saders, J. L. & Pinsonneault, M. H. 2013, ApJ, 776, 67

van Saders, J. L., Pinsonneault, M. H., & Barbieri, M. 2019, ApJ, 872, 128

VanderPlas, J. T. 2018, ApJS, 236, 16

Vanderspek, R., Doty, J. P., Fausnaugh, M., Villaseñor, J. N. S., Jenkins, J. M., Berta-Thompson, Z. K., Burke, C. J., & Ricker, G. R. 2018, TESS Instrument Handbook, `https://archive.stsci.edu/missions/tess/doc/TESS_Instrument_Handbook_v0.1.pdf`

Vilhu, O. & Rucinski, S. M. 1983, A&A, 127, 5

Virtanen, P., Gommers, R., Oliphant, T. E., Haberland, M., Reddy, T., Cournapeau, D., Burovski, E., Peterson, P., Weckesser, W., Bright, J., van der Walt, S. J., Brett, M., Wilson, J., Jarrod Millman, K., Mayorov, N., Nelson, A. R. J., Jones, E., Kern, R., Larson, E., Carey, C., Polat, İ., Feng, Y., Moore, E. W., Vand erPlas, J., Laxalde, D., Perktold, J., Cimrman, R., Henriksen, I., Quintero, E. A., Harris, C. R., Archibald,

A. M., Ribeiro, A. H., Pedregosa, F., van Mulbregt, P., & Contributors, S. . . 2020, Nature Methods, 17, 261

Vitense, E. 1953, ZAp, 32, 135

Wood, B. E., Müller, H. R., Zank, G. P., Linsky, J. L., & Redfield, S. 2005, ApJ, 628, L143

Wright, N. J., Drake, J. J., Mamajek, E. E., & Henry, G. W. 2011, ApJ, 743, 48

Zasowski, G., Johnson, J. A., Frinchaboy, P. M., Majewski, S. R., Nidever, D. L., Rocha Pinto, H. J., Girardi, L., Andrews, B., Chojnowski, S. D., Cudworth, K. M., Jackson, K., Munn, J., Skrutskie, M. F., Beaton, R. L., Blake, C. H., Covey, K., Deshpande, R., Epstein, C., Fabbian, D., Fleming, S. W., Garcia Hernandez, D. A., Herrero, A., Mahadevan, S., Mészáros, S., Schultheis, M., Sellgren, K., Terrien, R., van Saders, J., Allende Prieto, C., Bizyaev, D., Burton, A., Cunha, K., da Costa, L. N., Hasselquist, S., Hearty, F., Holtzman, J., García Pérez, A. E., Maia, M. A. G., O'Connell, R. W., O'Donnell, C., Pinsonneault, M., Santiago, B. X., Schiavon, R. P., Shetrone, M., Smith, V., & Wilson, J. C. 2013, AJ, 146, 81

Zhang, M., Xiang, M., Zhang, H.-W., Ting, Y.-S., Rix, H.-W., Wu, Y.-Q., Huang, Y., Sun, W.-X., Tian, Z.-J., Wang, C., & Liu, X.-W. 2021, ApJ, 922, 145

Zhao, G., Zhao, Y.-H., Chu, Y.-Q., Jing, Y.-P., & Deng, L.-C. 2012, Research in Astronomy and Astrophysics, 12, 723

Zhao, Q. & Zhang, L. 2005, in 2005 International Conference on Neural Networks and Brain, Vol. 2, 1089–1092

Zong, W., Fu, J.-N., De Cat, P., Wang, J., Shi, J., Luo, A., Zhang, H., Frasca, A., Molenda-Żakowicz, J., Gray, R. O., Corbally, C. J., Catanzaro, G., Cang, T., Wang, J., Chen, J., Hou, Y., Liu, J., Niu, H., Pan, Y., Tian, H., Yan, H., Zhang, Y., & Zuo, H. 2020, ApJS, 251, 15